Title
Photonic Actuation, Sensing, and Imaging of Biological and Soft Matters

Author
Ota, Sadao

Publication Date
2013

Peer reviewed|Thesis/dissertation

Photonic Actuation, Sensing, and Imaging of Biological and Soft Matters

By

Sadao Ota

A dissertation in partial satisfaction of the

Requirements for the degree of

Doctor of Philosophy

In Engineering- Mechanical Engineering

In the

Graduate Division

of the

University of California, Berkeley

Committee in charge:

Professor Xiang Zhang, Chair

Professor Seung-Wuk Lee

Professor Samuel S. Mao

Fall 2013

Photonic Actuation, Sensing, and Imaging of Biological and Soft Matters

by Sadao Ota

Abstract

Photonic Actuation, Sensing, and Imaging of Biological and Soft Matters

By

Sadao Ota

Doctor of Philosophy in Mechanical Engineering
University of California, Berkeley
Professor Xiang Zhang, Chair

This dissertation extensively investigates applications of optics in bioresearch and introduces a series of developments in novel optical technology. The developed techniques include optics-based particle manipulation; nanophotonic, device-based gas-sensing; and optical imaging.

Fine control and the inherently remote capability of light technologies allow for enormous potential in every facet of modern advanced technologies. By exploiting these advantages and employing the observable photons as information carriers, the optical techniques developed in the physical sciences are now rapidly finding numerous important applications in the research fields of biology, medicine, and soft matters. Some examples are optical manipulation, sensing, and imaging. I have worked on the technological developments to solve issues faced in this interdisciplinary field.

This thesis consists of four chapters. The first chapter serves as a brief introduction to each research field of optical manipulation, sensing, and imaging, encompassing the research of this PhD work. Chapter 2 describes three novel, optics-based techniques to manipulate nanoscopic objects: lipid integrated optoelectronic tweezers, optoelectrophoresis in nanofluidic scales, and the plasmonic Brownian Ratchet. Chapter 3 reports the development of a novel explosive gas sensor utilizing an actively excited plasmon nanocavity. Chapter 4 introduces two novel microscopy techniques: the nanowire-based backscattering interference contrast microscope and the axial plane optical microscope. The first of these two reveals the Brownian motion of the anisotropic colloids near a wall, and the latter finds its applications in three-dimensional biological tissue imaging and fluidic lithography.

Dedicated to my parents, Yasuto Ota and Michie Ota,
my wife, Aya Ota,
and my brother Eiri Ota,
for their endless love and support.

Table of Contents

List of Figures

Acknowledgement

First of all, I would like to thank my supervisor, Dr. Xiang Zhang, for providing me the full opportunity and support to work in an outstanding group and explore exciting science. Xiang is a solid scientist, and is fully open-minded for crazy ideas. At the same time, he is very sharp with ideas even from different research fields. I am impressed especially by his capability of making decisions on ideas based on vision and confidence. Through many good interactions, he sharpened and deepened my research in all aspects. Moreover, his group is full of experts from quite different backgrounds, keeping me exposed to unfamiliar and exciting science. Considering my background and research style, which is probably extraordinarily interdisciplinary, I could not have asked for a better advisor to learn how to do creative and productive research.

Before joining Xiang's group, I had opportunities to work with Dr. Seung Wuk Lee and Dr. Luke Lee. I do appreciate the experiences in their groups since I could learn many important things and realize what I want to do in research. After joining Xiang's group in Sep. 2009, I started to work with Sheng Wang who is very brilliant and excellently mentored me in general. I learned a lot of experimental skills, including optics, electronics, and biology. Xiaobo Yin and Yuan Wang were good managers and mentors for me. Their detailed criticism and guidance on my research ideas are truly helpful for improving research quality and understanding the science. I also learnt a lot from other kind and smart post-docs including Dr. Atushi Ishikawa, Dr. Thomas Zentgraf, Dr. Rupert Oulton, and Dr. Teruya Ishihara. They taught me how to write a paper and how to make higher impact by deepening ideas. Nga also kindly supported me for a variety of works.

After starting to work independently, I was fortunate that I could work with many best collaborators. Tongcang, my favorite scientists, worked with me to develop a new imaging system and helped me write many papers and build experimental set-ups. He loves science, knows a variety of physics, and is a very solid experimentalist. He showed how to promptly solve problems and taught me that we have no limit in creativity. Renmin worked with me to enable the ultra-sensitive gas sensing. We often worked until mid-night, talked about many things, and he drove me to home. Our friendship will continue. Paloma and I worked for pushing the idea of plasmonic ratchet into reality. Dr. M. Reza Aram helped me really a lot to theoretically investigate the near-wall Brownian motion of anisotropic particles.

I would like to thank other students in the lab who have provided much help and precious friendships to me. Frequent discussions and chatting with Ziliang ye and Zi Jing Wong are my precious memory. It is also true for other too-many-to-mention friends from all over the world. Lastly, I would like to thank our sub-group members, Dr. Tongcang, Jeongmin Kim, Dr. Liang Feng, Dr. Peng Zhang, Dr. Jie Zhu, Dr. Xuefeng Zhu, and Dr. Baolei Li. Without your help and our joyful discussions, I don't think I could enjoy my research this much.

Finally, I would definitely like to thank my wife, Aya Ota. Our adventure was not so easy, but eventually very fruitful. Without her talent of enjoying life, I could not make so many friends here and life here so joyful. I also want to thank my parents who allowed me to leave Japan despite his disease. Also my brother, your work keeps providing me with stimulation and inspiration.

Sadao Ota, December 16, 2013, Berkeley, CA

Chapter 1

Introduction: Photonic Actuation, Sensing, and Imaging of Biological and Soft Matters

Photonics is the term developed as the outgrowth of practical semiconductor light emitters in the range of the visible and near infrared in the early 1960s. These increasingly available good light sources increased understanding of the nature of light as both waves and particles and gave birth to a variety of advanced optical innovations. Optical methods are unique and advantageous because the behaviors of light can be remotely designed and the light-matter interactions can be remotely understood. By exploiting these advantages of light as information vehicle, the optical techniques developed in the physical sciences are now rapidly finding numerous important applications in biology, medicine, and soft matters, including manipulation, imaging, sensing, and synthesis. These research fields are intrinsically interdisciplinary, requiring rich knowledge in sciences, insights in fundamental challenges for finding opportunities, and solid engineering skills for constructing effective solutions and executing ideas. In this dissertation—based on a wide range of knowledge in optics, optoelectronics, image processing, nanoscale photonics, and biology—I developed a series of optical technologies to address important issues of microscopic particle manipulation, optical gas sensing, optical imaging, and 3D optical lithography. This chapter will serve as a brief introduction to these fields and encompasses the research direction of this dissertation work.

1.1 Micro- and Nanoscopic Object Manipulation

1.1.1 Introduction and Summary of Existing Methods

Manipulation of micro- and nanoscopic object such as colloids, nanoparticles, and molecules is of great importance in a wide variety of research fields, from biological science and fundamental physics to nanotechnology. For example, trapping a single micro-sized particle revolutionized the study on the force mechanisms generated by single-chemical or biological molecules and chemical bonds [1-3]. As opposed to conventional ensemble spectroscopies, this single-molecule force spectroscopy enabled determining properties of a particular molecule under study and has revealed the mechanochemical coupling in enzymatic activities [4] and rare events such as conformational changes [5]. On the other hand, parallel manipulation of many small particles is also desired in the field of soft matters and high-throughput biotechnologies. For example, a monolayer of colloids represents analogues to various two-dimensional (2D) physical systems [6, 7], and tracking and/or controlling trajectories of these colloids allows us to study the 2D systems at the microscopic levels. Especially under an imposed potential field, the colloidal dispersion exhibits thermodynamic behaviors characteristic to many-bodied systems, offering a rich opportunity for understanding Brownian dynamics as well as fundamental insights into the phase change behaviors of freezing [8], melting [9], and molecular membrane dynamics [10]. Moreover, the nanoparticles allow us to communicate with biological systems at the sub-cellular resolution, both physically

and chemically, and thus potentially enable novel nanotechnology-based biological studies, with good manipulations systems [11].

Over the last decades, scientists have developed ways to achieve such capability based on several mechanisms, including optical, electrokinetic, magnetic, acoustic [12], and hydrodynamic forces [13], some of which will be briefly introduced in this chapter. Among them, optical tweezers has apparent superiority in terms of its remoteness, high resolution for trapping individual objects, and high optical addressability. However, it typically requires strong light intensity to create a stable trap, limiting the size and kinds of particles to be trapped since such strong light can cause photo-induced damages. Moreover, the requirement of high light intensity limits the number of parallelized laser beams, or throughput, needed for certain applications. The other force mechanisms can alternatively achieve high throughput, but precise control of these forces at single particle levels is challenging due to intrinsic difficulty in remotely addressing them to individual targets while preventing them from interfering with each other. As a result, parallel manipulation technology that can controllably handle individual particles of a very small size, particularly much below the wavelength of light, is still a challenge.

Optical Tweezers

A decade after the invention of the laser, in 1970, Arthur Ashkin demonstrated the use of radiation pressure of the focused laser beam to accelerate and trap transparent microspheres [14]. More than a decade after this first demonstration, Ashkin et al. (1986) showed the stable trapping of dielectric particles with the gradient force of a tightly focused laser beam [15]. Currently, the optical tweezers is widely utilized to trap and manipulate nanomaterials and biological objects [16-18], and they have become a standard tool in the biophysics field [19].

The optical force originates from the transfer of the photon momentum from the incident light beam to the manipulated particle. When the particle size is much larger than the wavelength of the trapping light (typically $R > 10\lambda_0$, where R is the particle radius and λ_0 is the light wavelength in air), ray optics allows for calculation of the optical forces [15, 20]. Fig. 1.1.1 shows the qualitative view of the gradient force of optical tweezers at the laser focus. When the particle moves to the left of the laser focus, it deflects the laser beam to the left and thus increases the momentum of photons to the left. The particle feels the counter force from the deflected photons to the right and is thus pushed back to the laser focus (Fig. 1.1.1a). When the particle moves along the laser's propagation direction (Fig. 1.1.1c), it defocuses the laser and thus decreases the momentum of photons along the propagation direction. The particle feels the counter force from the deflected photons and is thus pushed back to the laser focus. The mechanism of the forces to push back the particle to the laser spot is generally applicable to the particles in any position; thus, the focused laser can create a 3D stable optical trap.

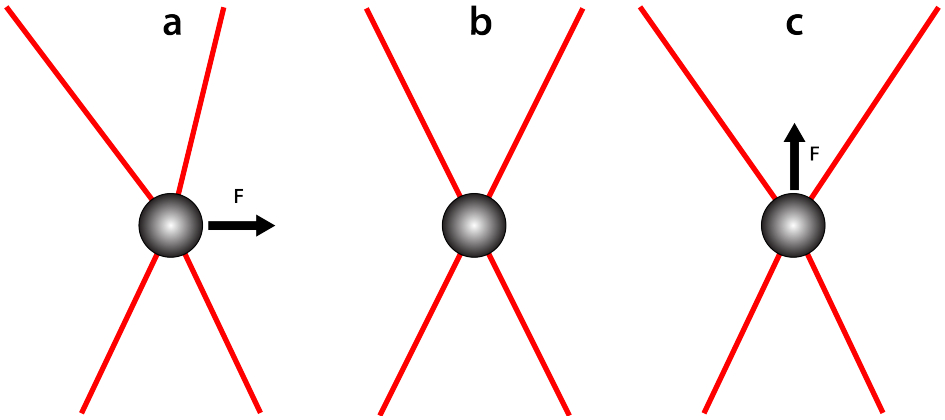

Figure 1.1.1 Qualitative, ray-optical depiction of optical tweezers for trapping a transparent, dielectric, micro-sized sphere. The strongly focused laser beam creates a potential well of optical gradient forces in the 3D space, enabling a stable trapping of the particle. Particles located in positions laterally (**a**) or vertically (**b**) from the focus spot of the laser beam are pushed back to the focus due to the momentum transfer by the deflected photons.

When the particle size becomes smaller than the trapping laser wavelength, the nanosphere can be approximated as a dipole. In this regime, the optical gradient force on the nanosphere under the incident laser intensity $I(\vec{r})$ can be analytically calculated with the Rayleigh scattering theory [21]:

$$\vec{F}_{grad}(\vec{r}) = [\vec{p}(\vec{r},t)\cdot\nabla]\vec{E}(\vec{r},t) = \frac{2\pi n_{md} R^3}{c}\left(\frac{m^2-1}{m^2+2}\right)\nabla I(\vec{r}) \qquad (1.1)$$

where m is the relative refractive index compared to the media index and $\vec{p}(\vec{r},t)$ is the dipole in the nanoparticle induced by the instantaneous electric field $\vec{E}(\vec{r},t)$ of the laser. The $\vec{F}_{grad}(\vec{r})$ creates a trapping potential:

$$V_{grad}(\vec{r}) = \frac{2\pi n_{md} R^3}{c}\left(\frac{m^2-1}{m^2+2}\right) I(\vec{r}) \qquad (1.2)$$

Optical tweezers holds apparent advantages over the other methods, offering optical addressability and high resolution for trapping individual objects [22, 23]. Despite the remarkable advances in the last 40 years, optical manipulation of individual specimens smaller than the wavelength of light, including biological molecules and nanoparticles, remains a considerable challenge. The major reason is that the optical forces decrease linearly with decreasing particle volume (equation (1.1) and (1.2)). The small optical index contrast between biological objects and water (small m in equation (1.2)) is another reason for this challenge. When one tries to trap the very small objects by increasing the light intensity, thermal or photochemical damages to these fragile objects become a critical issue. Although a laser beam with a wavelength at the near-infrared window is typically used for biological cells' manipulation to prevent optical damages due to heat generated from light absorption [24], the issue cannot be resolved for smaller individual molecules. In most cases, indeed, the optically trapped biological specimens have been micrometer sized [1-5]. In these cases, smaller macromolecules and molecular motors (sizes ~10^{-9} m) were studied by attaching the molecular specimens to

larger, micrometer-scale beads (~10^{-6} m) that can be optically trapped and stably manipulated. Unfortunately, because the bead is several hundred times larger than the specimen of interest, the tethering could affect the mechanical or biological properties of the specimen. Thus, the intrinsic issue of the potential damage induced by the strong optical intensity has limited its application in general. On the other hand, parallel optical tweezers have been utilized for many particle manipulations, where shaped optical fields generated with acousto-optic [25], interference [8], or holographic technologies [26, 27] were conventionally utilized to form desired landscapes of the optical potential field. However, because of the intrinsic challenge to maintain the strong light intensity for all parallelized laser beams, the throughput has been limited, especially for nanoparticle manipulations.

Electrokinetic Trap: Electrophoresis and Dielectrophoresis

The electrokinetic trap is commonly used for manipulating micro- and nanoscale particles in microfluidic devices; recent progress in microfabrications has enabled routine patterning of arbitrarily shaped electrodes. Such designed electrodes at micron resolutions can address the electrokinetic forces to control the microparticles' position, finding application in a variety of particle sorting and trapping techniques [28, 29]. Two of the most frequently used electrokinetic force mechanisms are electrophoresis [30] and dielectrophoresis [31].

First, electrophoresis refers to the particle motion induced by an applied direct current (DC) electric field on electrically charged particles (Fig. 1.1.2a). In electrophoresis, nanoscale particles such as DNA or proteins can be sorted out based on their electrophoretic mobility. The charged particles with a higher mobility move faster under the same electric field strength; $v = \mu E$, where v is the velocity, μ is the electrophoretic mobility, and E is the electric field [30]. The electrophoresis-based methods are inherently capable of noncontact, noninvasive parallel manipulation. They can manipulate only charged particles but are not limited by the particle size, which is typically the limit for other force mechanisms. Second, dielectrophoresis (DEP) refers to the particle motion due to the force generated by nonuniform electric fields acting on field-induced dipoles of the particles. The mechanism is the electrical analog of optical tweezers (Fig. 1.1.2b). This phenomenon relies on the gradient force of an electric field rather than on an optical field [31]. The magnitude of this dielectrophoretic force is proportional to the volume of the manipulated particles and the gradient of the squared electric field intensity $\nabla(E_{rms}^2)$ [32]:

$$\langle \vec{F}_{DEP}(t) \rangle = 2\pi r^3 \varepsilon_m \mathrm{Re}[K^*(\omega)] \nabla(E_{rms}^2) \qquad (1.3)$$

$$K^*(\omega) = \frac{\varepsilon_p^* - \varepsilon_m^*}{\varepsilon_p^* - 2\varepsilon_m^*},\ \varepsilon_p^* = \varepsilon_p - j\frac{\sigma_p}{\omega},\ \varepsilon_m^* = \varepsilon_m - j\frac{\sigma_m}{\omega} \qquad (1.4)$$

where r is the radius of spherical particles, ε_p and ε_m are the relative permittivity of the particle and medium, σ_p and σ_m are the conductivity of the particle and medium, and $\mathrm{Re}[K^*(\omega)]$ is the real part of Clausius−Mossotti (CM) factor. $K^*(\omega)$ represents the complex polarizability of the particle in the medium under the applied alternating current (AC) electric field at the angular frequency of ω. DEP, unlike electrophoresis, is able to

apply its forces on both charged and neutral particles and has been used to trap and sort micro- and nanometer particles such as cells, bacteria, and viruses [33].

Electrokinetic mechanisms are convenient tools for cell manipulation in multiparticle or batch scale processes. However, manipulating single cells that are randomly distributed on a surface requires high-resolution, pre-patterned electrode pixels over the large area. As a result, wiring and addressing these electrodes became one of the major challenges of using electrokinetic mechanisms for single cell manipulation. While a complementary metal oxide semiconductor (CMOS) DEP has been proposed to solve this issue, the complicated CMOS DEP chip is not cost-effective enough for biological applications, especially for disposable devices, to prevent cross-contamination[34].

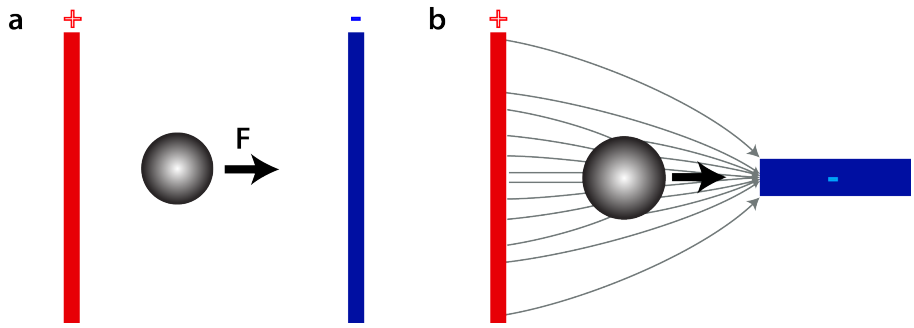

Figure 1.1.2 Electrokinetic Particle Manipulation. **(a)** shows the electrophoresis where the dc electric field is typically applied between electrodes and charged objects to generate the electrostatic force. **(b)** shows dielectrophoresis, where particles feel the force because of nonuniform electric fields acting on field-induced dipoles of the particles.

Magnetic Trap

Magnetic forces are also often used to sort the biological cells in a variety of applications such as flow cytometry [35]. Magnetic beads are typically made of polymers containing a large number of superparamagnetic nanoparticles. The surface of these magnetic particles can be functionalized with antibodies, peptides, or lectins, to be attached to or engulfed by cells in the following steps. The target cells recognized by these biomarkers are tagged by the magnetic beads and can be sorted out by applying a static magnetic field.

The magnetic force is advantageous over the electrokinetic or optical forces since static magnetic fields have fewer effects on the manipulated cells. On the other hand, it is intrinsically challenging to realize the magnetic tweezers with high resolution and high addressability. The microelectromagnetic template has been proposed to manipulate single cells at a high resolution using a magnetic field, which is essentially a matrix of microstructured electrical coils that can create highly localized magnetic field profiles [36]. The force generated in the magnetic field is expressed as $F = m \cdot B$, where B is the magnetic flux and $m = V\chi B/\mu_0$, where V is the magnetic bead's volume, χ is the bead's susceptibility, and μ_0 is the vacuum permeability in the vacuum. Although such microelectromagnetic templates have shown the potential of magnetic tweezers for manipulating single cells, parallel manipulation of multiple cells remains challenging due to the cross-interference of traps at high density of the cells. In addition, attaching the high density of the magnetic beads to cells may alter the nature of the cellular processes.

1.1.2 Challenge and Scope of Dissertation Work

In summary, the existing methods demonstrate that optical tweezers have a clear advantage in terms of high addressability and high resolution in the face of decreasing force with the decrease in particle size. Other force mechanisms do not have such addressability and resolutions but can generate larger forces with the same amount of energy used for optical tweezers. In 2005, Professor Ming Wu's group combined the strength of optical tweezers and DEP to demonstrate so-called optoelectronic tweezers (OET) [37], which could manipulate individual biological cells at high addressability and resolution. Nevertheless, it is still challenging for the OET to controllably handle nanoscopic objects whose size is much below the wavelength of light because the OET force is also proportional to the particle size. In chapter 2 of this dissertation, I will introduce three novel technologies to address optics-based manipulation of nanoscopic objects: OET integration with a biological membrane for enhancing its capability, a novel optoelectrophoresis concept at the nanofluidic scales for manipulating truly small biomolecules, and plasmonic nanotweezers for transporting particles over a long distance.

1.2 Optics-based Gas Sensing

1.2.1 Introduction and Summary of Existing Methods

Sensing converts the physically measured quantities into signals that can be observed (typically electronically). A huge number of optical sensors have been developed and commercialized in the market, including temperature [38], electrical, vibrational [39], gaseous [40], and biomolecular [41] sensors. Particularly, there is critical demand for the gas sensing to maintain high security and high-quality health care for the future sustainable society [42, 43]. Direct detection of gas-phase molecules is advantageous over the liquid-assisted gas sensing because its simple detection procedure is more user friendly and quite often cost-effective. For example, certain kinds of volatile gases in our breath vapors are good indicators of potential diseases such as cancer [42]. Direct detection of these gas-phase molecules can effectively reduce the cost of the cancer diagnoses currently performed through lab procedures. Another example of its use in ensuring better security is early detection of explosives in situations such as airports and battlefields, and the complicated liquid-based lab-procedures cannot be utilized in practice [43]. Despite huge potential, the development of optics-based gas sensors was not as rapid as electric-based gas sensors [44] (so-called electric nose) in general, mainly because of the small size of gas molecules and their minimal interaction with the light.

Mid-IR Absorption Spectroscopy (Optical Nose)

Most typical organic molecules have vibrational modes that can be efficiently excited with radiation energy of resonant frequencies. Because such a resonant frequency is characteristic of the structure of a molecule, every molecule provides its unique absorption peaks in the mid-infrared range of the light spectrum. In this IR spectroscopy, a gas sample of interest is delivered in an optical cavity equipped with two highly reflective mirrors and infrared windows (Fig. 1.2.1) [45]. The probe IR laser beam is directed into this cavity, where the light reflects back and forth, to increase the light

interaction with the delivered gas molecules. If a large enough sample is provided in the cavity and the signal-to-noise ratio is high enough, this spectroscopy produces the most quantitatively accurate results.

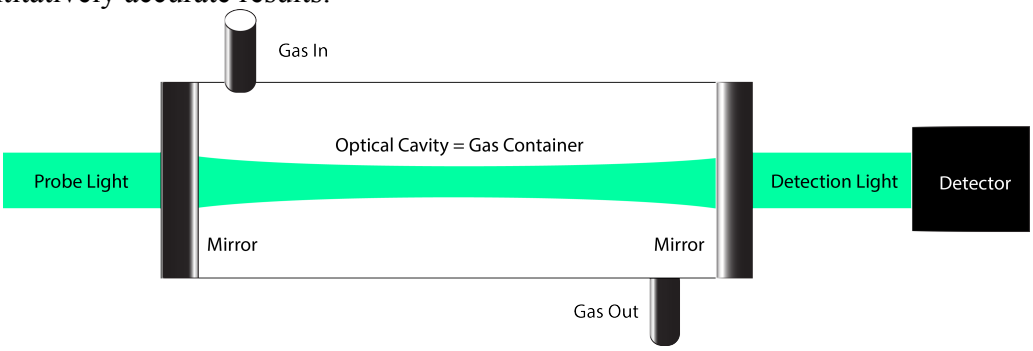

Figure 1.2.1 Typical optical setup used for Mid-IR absorption spectroscopy (Optical Nose).
The setup utilizes a relatively large optical cavity that acts as a gas container while enhancing the light interaction with the diluted gas molecules (small absorption).

Despite its accuracy, the drawback of IR absorption spectroscopy for gas sensing is that it requires the cavity with a long path length to compensate for the diluteness. The more the gas molecules are diluted, the longer the path length of the cavity needs to be. This requirement for large volumes of gaseous samples limits its sensitivity as well as its practical applications, such as detection of explosives in battlefields or medical diagnosis from breath vapors. One solution is to compress the volume sample, but additional cost on sample collection is disadvantageous for the competition with other approaches [46].

Photonic and Plasmonic Resonant Sensors

As mentioned above, the intrinsic challenge for the optical gas sensing is that the interaction between the small gas molecules and photons are too small. One way to solve this issue is to utilize the enhanced interaction of the molecules with near-field light in photonic and/or plasmonic resonant devices. The photonic/plasmonic structures enable strong light confinement in the nanoscale devices, and the evanescent decaying near field light energy bound within sub-diffractive spaces makes the optical resonators very sensitive to the refractive index changes of the surroundings [47]. Two of the best-known plasmonic and photonic devices are surface plasmon resonance (SPR) sensors and microring resonators (MR).

Most typical SPR sensors utilize a thin metallic film that has one side exposed to an analyte solution while the other side faces a glass prism (Fig. 1.2.2a) [48]. The SPs, light-excited collective oscillation of free electrons in metals, are excited by shining a laser or LED into the prism at an angle from behind it. The efficiency of SP excitation relies on the incident angle of the light and the refractive index of the surroundings due to momentum matching. This dependence of the SP's resonance on the incident angle enables determination of the refractive index of the surroundings, finding the single angle that gives the SP resonance peak. When the surface adsorption of target molecules changes the surrounding's index, this angle that provides the SP's resonant peak shifts, allowing for molecular detection. On the other hand, the MR-based sensors are similar to the SPR sensors since it also monitors its resonance wavelength shift due to the molecular absorption. In the MR device, light can be coupled to this ring resonator through evanescent coupling from a straight waveguide nearby (Fig. 1.2.2b) [49]. At a resonant

wavelength of the ring resonator, light can be confined in the ring structures and keep circulating inside it. Because such photons at this wavelength cannot escape the resonator and will be lost there, the transmission spectrum from the straight waveguide shows the complementary resonant dip. When the surface absorption of target molecules changes the surrounding's index, this resonant wavelength shifts, enabling molecular detection.

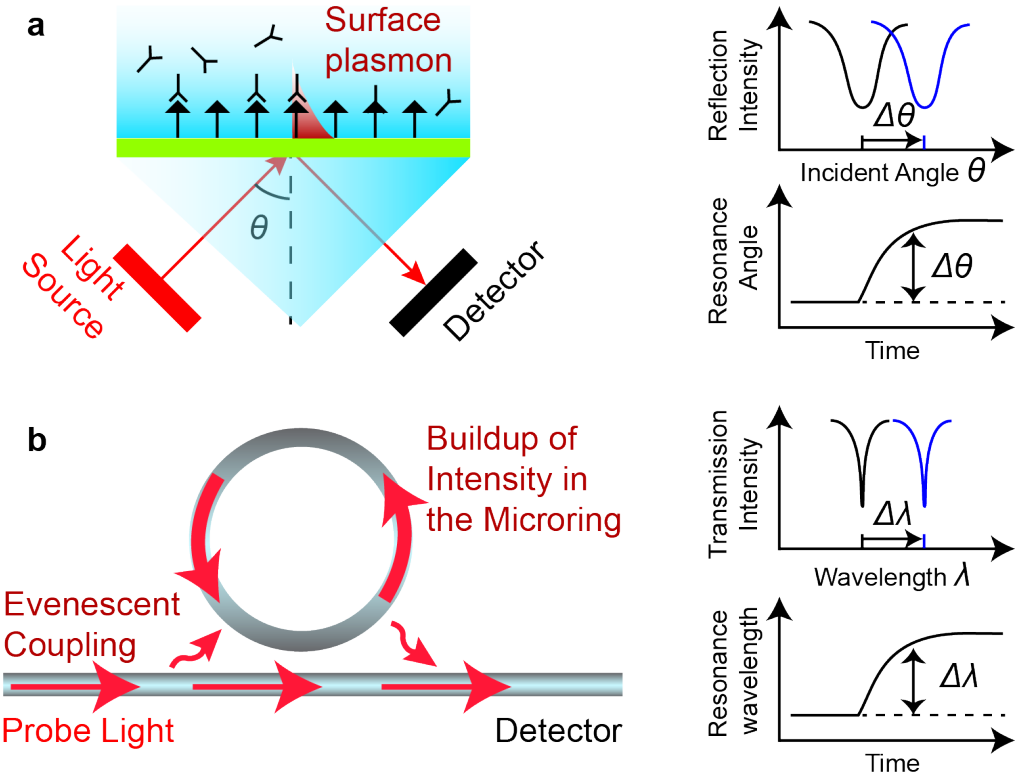

Figure 1.2.2 Refractive index change-based optical sensors. (a) In surface plasmon resonance sensors (SPR), the refractive index of the surroundings due to the molecular absorption can be detected in the shift on incident angles that provides the most efficient SP excitation and consequently the smallest reflection intensity at detection. **(b)** In the ring resonator, its resonant frequency shifts with the change in refractive index due to molecular absorption on surfaces. In both cases, the change of the resonant frequency of the devices is translated as the concentration of molecules detected.

The SPR sensor is simple and cheap. The intrinsically enhanced interaction of the surface waves and the surface events makes it highly sensitive in a real-time and label-free manner [48]. However, its sensitivity is intrinsically limited by the high ohmic loss in the metals, which significantly degrades the quality factor, Q, making it difficult to distinguish the resonance peak wavelength and its shift [50]. On the other hand, the MR sensors can retain significantly high Q and have achieved reliable single biological molecule sensing, though their fabrication is expensive and their complex measurement is not practical for real applications. Moreover, these sensors are relatively large, and their surface-to-volume ratio is limited because the dimensions of such dielectric cavity are intrinsically limited by the diffraction of light [51]. As a result, even with these high Q resonators, it is still a challenge to directly detect the small gas molecules.

Fluorescent Polymer Sensors

A series of fluorescent polymers have been utilized for detecting nitroaromatic explosives via various transduction schemes [43, 52-55]. Many nitroaromatic explosives such as trinitrotoluene (TNT) and dinitrotoluene (DNT) are electron deficient and can efficiently quench luminescent polymers via electron transfer, enabling the continuous detection of such explosives (Fig. 1.2.3).

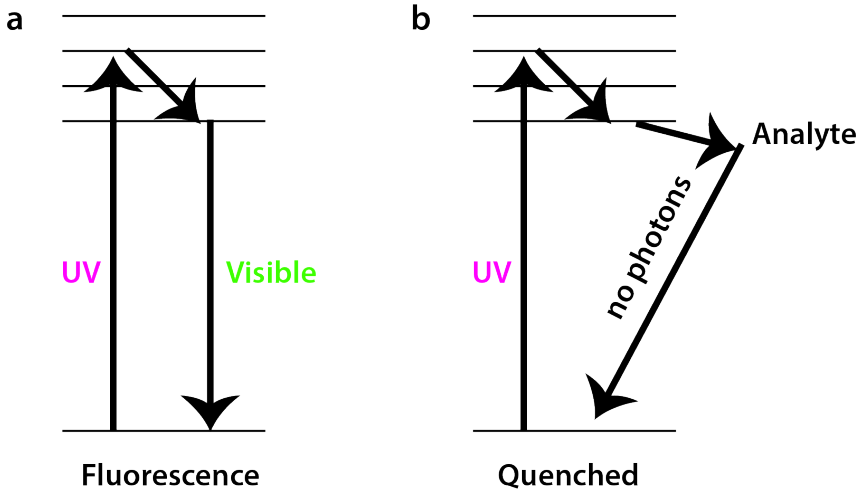

Figure 1.2.3 Conjugated polymer-based nitroaromatic explosive sensing. (**a)** shows the standard fluorescence process, where UV excites the electron in fluorescent polymer molecules; after relaxation, it goes back to the ground state by emitting the fluorescent photon. (**b)** shows the process of quenching due to the binding of nitroaromatic explosive molecules, where the excited photon goes to the quenching process via electron transfer through the quencher molecule, and it eventually returns to the ground state without photon emission.

Among various sensing devices, such fluorescent organic materials have emerged as one of the most promising platforms, first because it is simple and cheap. Due to the high porosity of polymer matrix, these materials can be sensitive. Furthermore, polymer chemistry allows for designing specificity to the target gas molecules and thus can provide ideal. On the other hand, its disadvantage is that all organic polymers are subject to significant photobleaching under strong excitation [42, 52]. This low photo-stability limits the device lifetime and ultimately the stability because it is difficult to obtain large signals (large signal-to-volume ratio) from the device.

Surface Enhanced Raman Scattering (SERS)

Raman scattering spectroscopy is an ideal technology because, in principle, each molecule has its own specific characteristic Raman spectrum. However, Raman is notoriously inefficient and inelastic with a very small cross-section (in the order of 10^{-30} cm^2, while fluorescence usually has a cross-section of 10^{-16} cm^2), resulting in extremely weak signals. Signal enhancement is thus necessary for most practical Raman sensing applications, leading to advancement of important research areas of surface-enhanced Raman scattering (SERS). SERS essentially utilizes metallic nanostructures where excitation of localized surface plasmons causes extraordinary enhancement of electric field, drastically improving the Raman signal detection. One common approach for achieving such high enhancement is to use aggregated colloidal metallic nanoparticles.

So-called hotspots at the narrow gaps between the particles create the highly enhanced local electric field, E, leading to a strong ($\propto E^4$) SERS signal. The enhancement factor of these hot spots can reach up to 10^{14}, enabling detection of single biomolecules in a solution [56, 57]. SERS-based direct detection of gas molecules is also becoming important.

One of the major disadvantages of SERS detection is its low reproducibility and efficiency due to the stochastic nature of nanoparticle aggregation. First, strong hotspots have relatively low probability of occurring by random aggregation. Second, even when using the same aggregate, the target molecule's adsorption is random. As a result, although SERS is very powerful in determining the target's presence or absence, it is not easily able to quantify detection results, such as the concentration of the vapors. Recent efforts demonstrated a variety of more reliable SERS substrates, leading to the 10^{10} Raman enhancement factors [58-61], but achieving 10^{14} is still challenging with current technologies. Another challenge of the SERS gas sensing is that the affinity of gas-phase molecules with metallic surfaces is not as strong as that in water. In most demonstrations, the detection procedure requires preparation of thin liquid layers on the SERS structures to achieve sensitive detection [62, 63]. This laboratory procedure limits the practical gas-sensing applications such as those at houses for health care purposes and at battlefields for security purposes.

1.2.2 Challenge and Scope of Dissertation Work

In summary, due to the intrinsically small interaction of light with small gas molecules, further research was required to enhance the sensitivity for optical gas sensors. The conventional approach required large amounts of (or compressed) gas to increase signals. Recent works utilized the photonic and plasmonic sensors to enhance the interaction of near-field light with the molecules, or adopted the novel electro-optically sensitive organic polymers. Despite rapid advancements of the optical gas sensors, detecting targeted molecules in the gas phase at high sensitivity with high specificity is a remaining goal for the large sensing community. Especially, optical detection of explosive molecules such as trinitrotluen (TNT) and di-nitrotluene (DNT), which have low vapor pressures and are diluted at sub-ppb level in the practical situations, has not yet been achieved. In chapter 3 of this dissertation, I will introduce a novel active plasmon lasing nanosensor that essentially combined the strength of photonics/plasmonic devices and electro-optical change in material properties. The sensor demonstrated sub-ppb detection of DNT in the gas phase with selectivity attributed to the electron deficiency of explosive molecules.

1.3 Optical Bio-imaging

1.3.1 Introduction and Summary of Existing Methods

Optical imaging is the collection of optical sensing over a spatially organized matrix. Optical bio-imaging has played a central role in the progress of modern biological and medical sciences. Absence/presence and spatial and temporal locations of molecules, cellular morphologies, tissue organization and dynamics—and many other important aspects of biological systems—were uncovered through the use of modern microscopies.

Each technique reveals an important aspect of biological phenomena via different interactions with light.

Classical Microscopy

The most fundamental interaction process of light with matter is transmission, absorption, and scattering (reflection) [64]. The most widely used standard microscopes utilize these processes, including bright-field microscopes and dark-field microscopes, which allow the user obvious advantages in terms of simplicity. By engineering the illumination and detection aspects by utilizing ray optical tricks, one can enhance the contrast of the optical information carried from the biological specimen with polarized light, phase contrast, and differential interference contrast microscopy. Each development of these microscopies brought in evolutional progress in the modern biological research. However, as the biological matter of interest becomes smaller, it becomes increasingly challenging to specifically image them because the light interaction with the individual natural biological molecules is too small to allow observation of their shadows or scatterings. Also, the different kinds of molecules typically demonstrate no distinguishable optical differences for observers. Moreover, the huge types of biological molecules are crowded in the micron scale compartments of cells, and the diffraction limits of light become an inevitable problem.

Sensors: Fluorescence and Scattering Labels

One way to achieve molecularly specific optical imaging is to label an optical sensor that converts the information (presence of specific molecules) to the optical signals. Among such sensors, fluorescent organic dyes or genetically encoded fluorescent proteins are essential tools for current molecular biology and medical technologies due to a large number of available fluorophores and the intrinsically high signal-to–background noise ratio [64, 65]. The fluorescence imaging technique evolved into various advanced methods whose images can provide important biological information at higher resolution, higher contrast, high speed, or with an increased number of colors. Particularly, the high-contrast imaging provided by optical sectioning methods such as laser scanning confocal microscopy and selective plane illumination microscopy has become increasingly important for imaging the large volume of samples such as animal tissues and brains [66-71]. The recently initiated brain-mapping project by the U.S. government provided motivation for faster and more convenient optical sectioning methods, which will be explained more in chapter 4 of this dissertation.

On the other hand, fluorescence imaging has several drawbacks: (1) the emission spectrum of fluorescence is typically so broad that the number of detectable colors in the image is limited [74]; (2) all organic fluorophores undergo significant photobleaching [75-77]; (3) attaching fluorophores to biological molecules can disturb their normal functions [78]. These drawbacks have been the motivation for the development of other imaging techniques.

A popular approach to overcoming the limitations of fluorescence imaging is the use of plasmonic nanoparticles such as gold and silver [79-82]. These particles can be resonant under the illumination of visible light and elastically scatter the light back to observer much stronger than biological objects can, providing high signal-to-noise ratio. There is no photobleaching issue for these scattering processes. Furthermore, recent

efforts have enabled many possible ways for target-specific attachment of these nanoparticles to expand the potential in biological research. However, these plasmonic particles are relatively larger (order of tens of nanometers) than those of organic fluorophores and biological molecules (order of several nanometers). Thus, they can have a much higher risk of disturbing the biological process. Another issue is that metallic nanoparticles can easily and randomly aggregate by themselves, and many kinds of biological molecules with cysteine groups may adhere to them too easily.

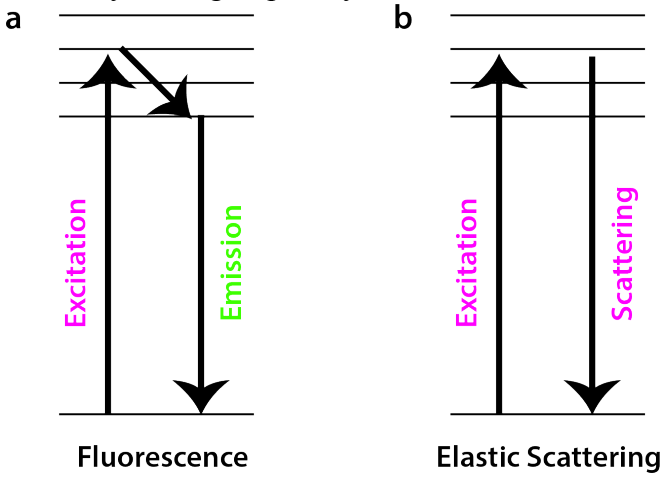

Figure 1.3.1 Fluorescence and Scattering. In the fluorescence process (**a),** an electron in the fluorophore is excited by light and, after relaxation, it goes back to the ground state by emitting a fluorescent visible photon. In the nanoparticles' case (**b),** it is an elastic scattering process such that they scatter back the photons whose color is the same as that of the excitation photons.

Nonlinear Imaging

Each molecule inherently contains molecular fingerprints such as unique vibrational, rotational, and other low-frequency modes [83]. With the rapid, rich understanding in the nonlinear optical phenomena for the last decades, it has become possible to read out these fingerprints in a direct optical manner without any labeling sensors. Although the currently best-known non-linear imaging method is maybe the two-photon excitation microscope—still a fluorescence imaging method enabling imaging of living tissue up to a very high depth of close to one millimeter [84-86]—I foresee that emerging label-free nonlinear microscopies able to observe the low frequency modes will make a large impact on the wide range of biological and biomedical communities. Good examples are founded in Raman spectroscopy, including microscopies based on Coherent anti-Stokes Raman spectroscopy [87-89] and Stimulated Raman Spectroscopy [90] (example processes shown in Fig. 1.3.2). These innovations employ multiple photons to address the molecular vibrations and can efficiently produce nonlinear signals without any labels.

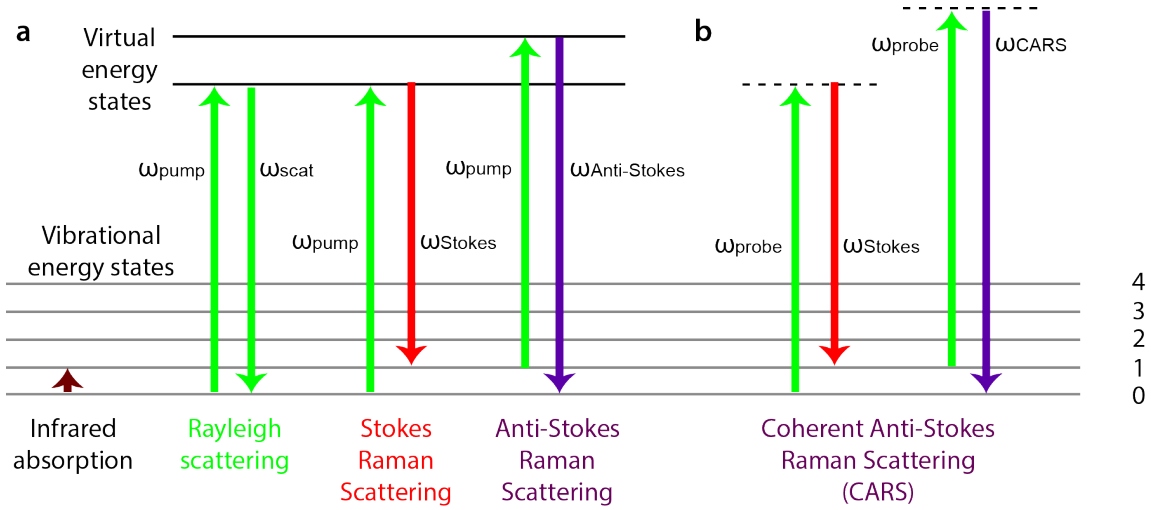

Figure 1.3.2 Energy-level diagram depicting the electronic states involved in the Raman process and coherent anti-stoked Raman scattering (CARS) (b). In the Raman process **(a)**, excitation laser light interacts with molecular vibrations and other modes at lower frequency modes, causing the energy of scattered laser photons to shift up or down. This shift corresponds to the vibrational modes in the system whereas the IR absorption spectroscopy (see chapter 1) yields complementary information. Because this Raman scattering occurs rarely, detection signals close to the laser wavelength due to elastic scattering are strictly filtered out. In the CARS process **(b)**, multiple photons are employed to address the molecular vibrations and to produce a coherent signal. Consequently, CARS can generate signals that are several orders of magnitude stronger than those of spontaneous Raman emission. The CARS process requires three laser photons: a pump beam of frequency ω_{pump}, a Stokes beam of frequency ω_{Stokes}, and a probe beam at frequency ω_{probe}. These beams interact with the sample and produce a coherent optical signal at the anti-Stokes frequency ($\omega_{probe} + \omega_{pump} - \omega_{Stokes}$). When the frequency difference between the pump and the Stokes beams ($\omega_{pump} - \omega_{Stokes}$) matches the frequency of a Raman resonance, the anti-Stokes signal is resonantly enhanced.

There is no doubt that these emerging nonlinear, label-free imaging technologies hold great potential. However, the intrinsic limit is its highly inefficient process. Indeed, the small spontaneous Raman scattering cross-section results in signals that are several orders of magnitude weaker than fluorescence-based methods. As a result, a very expensive, high-power pulsed laser is needed to efficiently observe the nonlinear signals. Although the use of metallic nanoparticles to enhance these small Raman signals, surface-enhanced Raman spectroscopy, is promising for the detection of molecules, their adverse interference with biological processes is not preferable for bio-imaging. Although this process is advancing, researchers need to find a way to reduce cost and to further improve signal generation.

1.3.2 Challenge and Scope of Dissertation Work

In summary, although classical microscopies are the basis for modern microscopies and nonlinear imaging extracts most molecular fingerprints, fluorescence imaging techniques play the most influential role in the recent discoveries of biology and medicine. The apparent advantage of fluorescence imaging is that it enables efficient extraction of structural and molecular information at higher temporal and spatial resolutions. To enhance this capability, an essential requirement is to efficiently collect the needed signals while rejecting un-needed signals as noise. Optical sectioning microscopes are the best examples. In chapter 4 of this dissertation, I will introduce a novel axial plane microscope and further its application as an optical sectioning

microscope. Essentially, my work realized the selective plane illumination microscopy with a single objective lens near the sample, and demonstrated the three-dimensional fluorescence imaging of auto-fluorescent pollens and stained mouse brain sections.

References

1. Jri, K. K. Unhinding force of a single motor molecule of muscle measured using optical tweezers. *Nature* **377,** 21 (1995).
2. Abbondanzieri, E. A., Greenleaf, W. J., Shaevitz, J. W., Landick, R. & Block, S. M. Direct observation of base-pair stepping by RNA polymerase. *Nature Cell Biology* **438,** 460–465 (2005).
3. Fazal, F. M. & Block, S. M. Optical tweezers study life under tension. *Nature Photonics* **5,** 318–321 (2011).
4. Mehta, A. D. Single-Molecule Biomechanics with Optical Methods. *Science* **283,** 1689–1695 (1999).
5. Uemura, S., Higuchi, H., Olivares, A. O., La Cruz, De, E. M. & Ishiwata, S. Mechanochemical coupling of two substeps in a single myosin V motor. *Nat Struct Mol Biol* **11,** 877–883 (2004).
6. Brunner, M. & Bechinger, C. Phase Behavior of Colloidal Molecular Crystals on Triangular Light Lattices. *Phys. Rev. Lett.* **88,** 248302 (2002).
7. Mikhael, J., Roth, J., Helden, L. & Bechinger, C. Archimedean-like tiling on decagonal quasicrystalline surfaces. *Nature* **454,** 501–504 (2008).
8. Chowdhury, A., Ackerson, B. J. & Clark, N. A. Laser-induced freezing. *Phys. Rev. Lett.* **55,** 833–836 (2011).
9. Korda, P. T. & Grier, D. G. Annealing thin colloidal crystals with optical gradient forces. *J. Chem. Phys.* **114,** 7570 (2001).
10. Barry, E. & Dogic, Z. Entropy driven self-assembly of nonamphiphilic colloidal membranes. *Proc. Natl. Acad. Sci. U.S.A.* **107,** 10348–10353 (2010).
11. Fan, D. *et al.* Subcellular-resolution delivery of a cytokine through precisely manipulated nanowires. *Nature Nanotechnology* **5,** 545–551 (2010).
12. Evander, M. *et al.* Noninvasive Acoustic Cell Trapping in a Microfluidic Perfusion System for Online Bioassays. *Anal. Chem.* **79,** 2984–2991 (2007).
13. Jönsson, P. *et al.* Hydrodynamic trapping of molecules in lipid bilayers. *Proc. Natl. Acad. Sci. U.S.A.* **109,** 10328–10333 (2012).
14. Ashkin, A. Acceleration and trapping of particles by radiation pressure. *Phys. Rev. Lett.* **24,** 156–159 (1970).
15. Ashkin, A., Dziedzic, J. M., Bjorkholm, J. E. & Chu, S. Observation of a single-beam gradient force optical trap for dielectric particles. *Optics letters* **11,** 288–290 (1986).
16. Pauzauskie, P. J. *et al.* Optical trapping and integration of semiconductor nanowire assemblies in water. *Nature Materials* **5,** 97–101 (2006).
17. Block, S. M., Blair, D. F. & Berg, H. C. Compliance of bacterial flagella measured with optical tweezers. *Nature* **338,** 514–518 (1989).
18. Xie, C., Dinno, M. A. & Li, Y.-Q. Near-infrared Raman spectroscopy of single optically trapped biological cells. *Optics letters* **27,** 249–251 (2002).

19. Neuman, K. C. & Nagy, A. Single-molecule force spectroscopy: optical tweezers, magnetic tweezers and atomic force microscopy. *Nature Methods* **5,** 491–505 (2008).
20. Ashkin, A. Forces of a single-beam gradient laser trap on a dielectric sphere in the ray optics regime. *Biophysj* **61,** 569–582 (1992).
21. Harada, Y. & Asakura, T. Radiation forces on a dielectric sphere in the Rayleigh scattering regime. *OPTICS* **124,** 529–541 (1996).
22. Moffitt, J. R., Chemla, Y. R., Smith, S. B. & Bustamante, C. Recent Advances in Optical Tweezers. *Annu. Rev. Biochem.* **77,** 205–228 (2008).
23. Dholakia, K. & Čižmár, T. Shaping the future of manipulation. *Nature Photonics* **5,** 335–342 (2011).
24. Hale, G. M. & Querry, M. R. Optical constants of water in the 200-nm to 200-µm wavelength region. *APPLIED OPTICS* **12,** 555–563 (1973).
25. Visscher, K., Gross, S. P. & Block, S. M. Construction of multiple-beam optical traps with nanometer-resolution position sensing. *Selected Topics in Quantum Electronics, IEEE Journal of* **2,** 1066–1076 (1996).
26. Reicherter, M., Haist, T., Wagemann, E. U. & Tiziani, H. J. Optical particle trapping with computer-generated holograms written on a liquid-crystal display. *Optics letters* **24,** 608–610 (1999).
27. Martín-Badosa, E. *et al.* Design strategies for optimizing holographic optical tweezers set-ups. *J. Opt. A: Pure Appl. Opt.* **9,** S267–S277 (2007).
28. Fields, A. P. & Cohen, A. E. Electrokinetic trapping at the one nanometer limit. *Proc. Natl. Acad. Sci. U.S.A.* **108,** 8937–8942 (2011).
29. Fu, A. Y., Chou, H.-P., Spence, C., Arnold, F. H. & Quake, S. R. An Integrated Microfabricated Cell Sorter. *Anal. Chem.* **74,** 2451–2457 (2002).
30. Hunter, R.J. *Foundations of Colloid Science*. Oxford University Press. (1989).
31. Pohl, H. A., *Dielectrophoresis the behavior of neutral matter in nonuniform electric fields*. Cambridge University Press. Cambridge, (1978).
32. Irimajiri, A., Hanai, T. & Inouye, A. A dielectric theory of 'multi-stratified shell' model with its application to a lymphoma cell. *Journal of Theoretical Biology* **78,** 251–269 (1979).
33. Cheng, I.-F., Froude, V. E., Zhu, Y., Chang, H.-C. & Chang, H.-C. A continuous high-throughput bioparticle sorter based on 3D traveling-wave dielectrophoresis. *Lab Chip* **9,** 3193 (2009).
34. Manaresi, N., Romani, A. & Medoro, G. A CMOS chip for individual cell manipulation and detection. *Solid-State Circuits* (2003).
35. Miltenyi, S., Müller, W., Weichel, W. & Radbruch, A. High gradient magnetic cell separation with MACS. *Cytometry* **11,** 231–238 (1990).
36. Lee, H., Liu, Y., Ham, D. & Westervelt, R. M. Integrated cell manipulation system—CMOS/microfluidic hybrid. *Lab Chip* **7,** 331–337 (2007).
37. Wu, M. C. Optoelectronic tweezers. *Nature Photonics* **5,** 322–324 (2011).
38. Bhatia, V. & Vengsarkar, A. M. Optical fiber long-period grating sensors. *Optics letters* **21,** 692–694 (1996).
39. Kimura, M. & Toshima, K. Vibration sensor using optical-fiber cantilever with bulb-lens. *Sensors and Actuators A: Physical* **66,** 178–183 (1998).

40. Hodgkinson, J. & Tatam, R. P. Optical gas sensing: a review. *Meas. Sci. Technol.* **24,** 012004 (2012).
41. Yalcin, A. *et al.* Optical sensing of biomolecules using microring resonators. *IEEE J. Select. Topics Quantum Electron.* **12,** 148–155.
42. Peng, G. *et al.* Diagnosing lung cancer in exhaled breath using gold nanoparticles. *Nature Nanotechnology* **4,** 669–673 (2009).
43. Rose, A., Zhu, Z., Madigan, C. F., Swager, T. M. & Bulovi cacute, V. Sensitivity gains in chemosensing by lasing action in organic polymers. *Nature* **434,** 876–879 (2005).
44. James, D., Scott, S. M., Ali, Z. & O'Hare, W. T. Chemical Sensors for Electronic Nose Systems. *Microchim Acta* **149,** 1–17 (2004).
45. Kreuzer, L. B. Ultralow Gas Concentration Infrared Absorption Spectroscopy. *J. Appl. Phys.* **42,** 2934–2943 (1971).
46. Bratož, S. & Martin, M. L. Infrared Spectra of Highly Compressed Gas Mixtures of the Type HCl+X. A Theoretical Study. *J. Chem. Phys.* **42,** 1051 (1965).
47. Erickson, D., Serey, X., Chen, Y. F. & Mandal, S. Nanomanipulation using near field photonics. *Lab Chip* (2011).
48. Homola, J., Yee, S. S. & Gauglitz, G. Surface plasmon resonance sensors: review. *Sensors and Actuators B: Chemical* **54,** 3–15 (1999).
49. Robinson, J. T., Chen, L. & Lipson, M. On-chip gas detection in silicon optical microcavities. *Opt. Express* **16,** 4296–4301 (2008).
50. Yeatman, E. M. Resolution and sensitivity in surface plasmon microscopy and sensing. *Biosensors and Bioelectronics* (1996).
51. Born, Max; Emil Wolf, *Principles of Optics*. Cambridge University Press, (1997).
52. Toal, S. J. & Trogler, W. C. Polymer sensors for nitroaromatic explosives detection. *J. Mater. Chem.* **16,** 2871–2883 (2006).
53. Sohn, H., Sailor, M. J., Magde, D. & Trogler, W. C. Detection of nitroaromatic explosives based on photoluminescent polymers containing metalloles. *J. Am. Chem. Soc.* **125,** 3821–3830 (2003).
54. Thomas, S. W., Joly, G. D. & Swager, T. M. Chemical sensors based on amplifying fluorescent conjugated polymers. *Chem. Rev.* (2007).
55. Liu, Y., Mills, R. C., Boncella, J. M. & Schanze, K. S. Fluorescent polyacetylene thin film sensor for nitroaromatics. *Langmuir* (2001).
56. Kneipp, K. *et al.* Single molecule detection using surface-enhanced Raman scattering (SERS). *Phys. Rev. Lett.* **78,** 1667–1670 (1997).
57. Nie, S. & Emory, S. R. Probing Single Molecules and Single Nanoparticles by Surface-Enhanced Raman Scattering. *Science* **275,** 1102–1106 (1997).
58. Sun, C. *et al.* Time-Resolved Single-Step Protease Activity Quantification Using Nanoplasmonic Resonator Sensors. *ACS Nano* **4,** 978–984 (2010).
59. Su, K.-H. *et al.* Raman Enhancement Factor of a Single Tunable Nanoplasmonic Resonator. *J. Phys. Chem. B* **110,** 3964–3968 (2006).
60. Nanophotonic crescent moon structures with sharp edge for ultrasensitive biomolecular detection by local electromagnetic field enhancement effect. **5,** 119–124 (2005).

61. Xu, H., Aizpurua, J., Kall, M. & Apell, P. Electromagnetic contributions to single-molecule sensitivity in surface-enhanced raman scattering. *Phys Rev E Stat Phys Plasmas Fluids Relat Interdiscip Topics* **62,** 4318–4324 (2000).
62. Sylvia, J. M., Janni, J. A., Klein, J. D. & Spencer, K. M. Surface-Enhanced Raman Detection of 2,4-Dinitrotoluene Impurity Vapor as a Marker To Locate Landmines. *Anal. Chem.* **72,** 5834–5840 (2000).
63. Spencer, K. M., Sylvia, J. M., Janni, J. A. & Klein, J. D. Advances in land mine detection using surface-enhanced Raman spectroscopy. in *AeroSense '99* (**3710,** 373–379 (SPIE, 1999).
64. Nikon Microcopy U: http://www.microscopyu.com/.
65. Perfetto, S. P., Chattopadhyay, P. K. & Roederer, M. Seventeen-colour flow cytometry: unravelling the immune system. *Nat. Rev. Immunol.* **4,** 648–655 (2004).
66. Agard, D. A. Optical sectioning microscopy: cellular architecture in three dimensions. *Annu. Rev. Biophys. Bioeng.* **13,** 191–219 (1984).
67. Conchello, J. A. & Lichtman, J. W. Optical sectioning microscopy. *Nat. Meth.* (2005).
68. Wilson, T. Optical sectioning in confocal fluorescent microscopes. *Journal of microscopy* (1989).
69. Webb, S. E. D. *et al.* A wide-field time-domain fluorescence lifetime imaging microscope with optical sectioning. *Rev. Sci. Instrum.* **73,** 1898–1907 (2002).
70. Coyle, I. P. Confocal imaging of fluorescently labeled proteins in the Drosophila larval neuromuscular junction. *Methods Mol. Biol.* **1075,** 201–212 (2014).
71. Keller, P. J., Schmidt, A. D., Wittbrodt, J. & Stelzer, E. Reconstruction of zebrafish early embryonic development by scanned light sheet microscopy. *Science* (2008).
72. Alivisatos, A. P. *et al.* Nanotools for neuroscience and brain activity mapping. *ACS Nano* **7,** 1850–1866 (2013).
73. Osten, P. & Margrie, T. W. Mapping brain circuitry with a light microscope. *Nat Meth* **10,** 515–523 (2013).
74. Chattopadhyay, P. K. *et al.* Quantum dot semiconductor nanocrystals for immunophenotyping by polychromatic flow cytometry. *Nat. Med.* **12,** 972–977 (2006).
75. Alivisatos, A. P., Gu, W. & Larabell, C. Quantum dots as cellular probes. *Annu Rev Biomed Eng* **7**, 55-76 (2005).
76. Ippen, E., Shank, C. & Dienes, A. Rapid Photobleaching of Organic Laser Dyes in Continuously Operated Devices. *IEEE Journal of Quantum Electronics* **7**, 178-179 (1971).
77. Dubois, A., Canva, M., Brun, A., Chaput, F. & Boilot, J. P. Photostability of dye molecules trapped in solid matrices. *Applied Optics* **35**, 3193-3199 (1996).
78. Okada, M. *et al.* Label-free Raman observation of cytochrome c dynamics during apoptosis. *Proc. Natl. Acad. Sci. U.S.A.* **109,** 28–32 (2012).
79. Lu, Y., Liu, G. L., Kim, J., Mejia, Y. X. & Lee, L. P. Nanophotonic crescent moon structures with sharp edge for ultrasensitive biomolecular detection by local electromagnetic field enhancement effect. *Nano Lett.* **5,** 119–124 (2005).
80. Daniel, M.-C. & Astruc, D. Gold nanoparticles: assembly, supramolecular

chemistry, quantum-size-related properties, and applications toward biology, catalysis, and nanotechnology. *Chem. Rev.* **104,** 293–346 (2004).
81. Sönnichsen, C., Reinhard, B. M., Liphardt, J. & Alivisatos, A. P. A molecular ruler based on plasmon coupling of single gold and silver nanoparticles. *Nature Biotechnology* **23,** 741–745 (2005).
82. Liu, G. L. *et al.* A nanoplasmonic molecular ruler for measuring nuclease activity and DNA footprinting. *Nature Nanotechnology* **1,** 47–52 (2006).
83. Boyd, R. W. Nonlinear optics. *Elsevier Science.* (2003).
84. Helmchen, F. & Denk, W. Deep tissue two-photon microscopy. *Nat Meth* (2005).
85. Kobat, D., Durst, M. E., Nishimura, N. & Wong, A. W. Deep tissue multiphoton microscopy using longer wavelength excitation. *Optics express* (2009).
86. Denk, W., Strickler, J. H. & Webb, W. W. Two-photon laser scanning fluorescence microscopy. *Science* (1990).
87. Evans, C. L. *et al.* Chemical imaging of tissue in vivo with video-rate coherent anti-Stokes Raman scattering microscopy. *Proc. Natl. Acad. Sci. U.S.A.* **102,** 16807–16812 (2005).
88. Duncan, M. D., Reintjes, J. & Manuccia, T. J. Scanning coherent anti-Stokes Raman microscope. *Optics letters* **7,** 350–352 (1982).
89. Cheng, J. X. & Xie, X. S. Coherent anti-Stokes Raman scattering microscopy: instrumentation, theory, and applications. *J. Phys. Chem. B* (2004).
90. Kukura, P. & McCamant, D. W. Femtosecond stimulated Raman spectroscopy. *Annu. Rev. Phys. Chem.* (2007).

Chapter 2

Nanoscopic Object Manipulations

2.1 Lipid Bilayer-Integrated Optoelectronic Tweezers for Nanoparticle Manipulations

2.1.1 Introduction to Optoelectronic Tweezers (OET)

As mentioned in section 1.1, there is still no technology capable of generating sufficient force over individual microscale objects in large fields with high resolution. While the conventional optical tweezers revolutionized the biophysics research [1-2], the high optical intensity required for trapping small particles has been problematic. To address this issue, the recently developed optoelectronic tweezers (OET) elegantly combined the advantage of OT with electrode-based dielectrophoresis (DEP) [3-9]. OET provides optically controlled manipulation at the single-particle level. It is a dynamic, reconfigurable, minimally invasive tool capable of massive parallel manipulation. This section will explain the operating principle and challenges of OET.

In OET, light patterns are projected onto a photosensitive semiconductor substrate to form "virtual electrodes" that concentrate the electric field when an external a.c. bias is applied, similar in function to a lightning rod. The resultant nonuniform electric fields interact with the induced dipole moments in the particles. This interaction results in the DEP forces, $\vec{F}_{OET}$, expressed as follows:

$$\langle \vec{F}_{OET}(t) \rangle = 2\pi r^3 \varepsilon_m \mathrm{Re}[K^*(\omega)] \nabla (E_{rms}^2) \qquad (2.1.1)$$

which is the same as the earlier equation (1.3) [6]. In essence, in the alternating nonuniform electric field, the particles are either attracted or repelled by the DEP force, depending on the CM factor's sign. The CM factor is defined in the same way as in Section 1.1.1. The use of virtual electrodes with OET simultaneously enables both dynamic optical addressability and large forces at low-light intensities (~1 W/cm^2) to achieve massive manipulation of microspheres and biological cells [3].

Despite OET's versatility, manipulating nanoscale objects remains a challenge because smaller particles experience a weaker DEP force; the force is proportional to the particle volume (equation 2.1.1). Furthermore, nanoparticles subject to larger Brownian fluctuations can easily escape from the potential trap because the DEP force decreases rapidly in distance from the photoconductive channel with the decreasing gradient of the squared electric field. Efforts have been made to address this issue by operating the OET device at a lower a.c. frequency (<10 kHz), where the light-induced a.c. electro-osmosis and/or electro-thermal flow [7] is utilized to concentrate and immobilize the nanoscale objects [13]. Yet, due to the intrinsic difficulty of controlling the 3D fluidic flows and the particles' irreversible immobilization onto surfaces, the reversible manipulation of nanoscale objects remains challenging.

2.1.2 Introduction of Lipid Bilayer and Its Integration with OET

My plan is to integrate a supported lipid bilayer (SLB), an ultrathin (~5 nm) 2D fluid, and the OET for parallel manipulation of nanoparticles. The SLB continuously covers the whole photoconductive substrate and confines the motion of nanoparticles tethered to the membrane in extreme vicinity of the substrate (Fig. 2.1.1a). Because the electric field strength most significantly changes near the substrate surface, the SLB integration ensures that large DEP forces can be applied to the particles (Fig. 2.1.1b). Using this approach, I have demonstrated the dynamic, reversible, and parallel manipulation of hundreds of gold nanoparticles (< 60 nm) in 2D space [14].

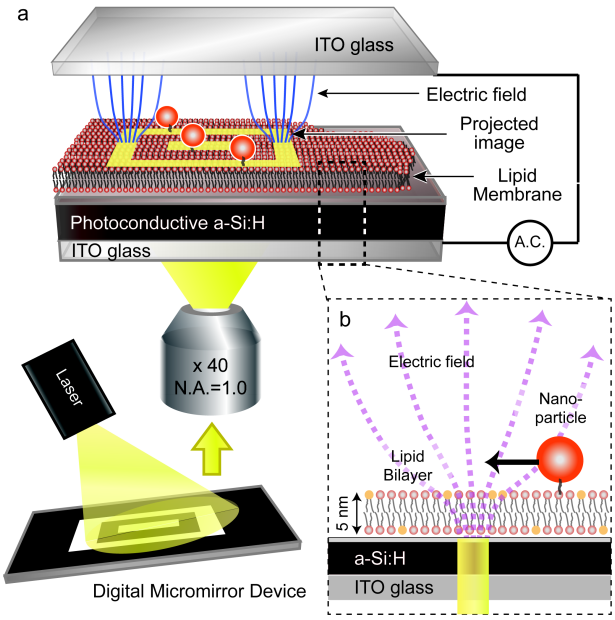

Figure 2.1.1 Optoelectronic tweezers integrated with a supported lipid bilayer (SLB). (**a**) shows the schematics of an experimental setup. A transparent ITO electrode and a photoconductive (hydrogenated amorphous silicon) electrode sandwiched an aqueous solution. By projecting light patterns from the DMD onto the photo-conducting layer and applying an a.c. electrical bias at the same time, the photo-induced "virtual electrodes" create dielectrophoretic traps in the illuminated areas. An SLB with 5 nm thickness is formed on the silicon surface, retaining lateral fluidity. (**b**) Due to the two-dimensional confinement defined by the SLB, tethered particles diffuse only in lateral directions in the extreme vicinity of the photoconductive substrate surface. This configuration enables the efficient application of the light-induced DEP force onto the particles because the field strength changes most significantly at the photo-activated surface, and the dielectrophoretic force is thus the strongest there.

Supported Lipid Bilayer (SLB)

SLB is a planar lipid bilayer structure sitting on a planar substrate, unlike a vesicle or a cell membrane in which the lipid bilayer is rolled into an enclosed shell [15]. In water, due to the intrinsic amphiphilic property of individual lipid molecules, lipids form its bilayer structure by facing the hydrophilic heads toward water. In the SLB, the upper face of the bilayer is exposed to a free solution while its lower faces the supporting substrate with a thin (~ 1nm) separation of a water hydration layer. In the two-dimensional space defined by the SLB, the individual lipid molecules can maintain their natural diffusivity in lateral directions. An important advantage of the SLB is its stability; it remains largely intact even when subject to fluid flows above it or to vibration, and the presence of holes will not destroy the entire bilayer. Like other lipid bilayer structures,

the SLB is inherently biocompatible and provides environments retaining the function of the membrane proteins that play crucial roles in cellular functions and have thus been main targets of drug discoveries [16-18].

2.1.3a OET Fabrication

In the fabrication of OET used for the SLB integration, glass cover slips (Fisher Scientific, Pittsburgh, PA) were first cleaned with piranha solution (3:1), concentrated sulfuric acid/30% hydrogen peroxide, for 10 min, thoroughly rinsed with deionized (DI) water, and then dried by a stream of nitrogen. A 50 nm of ITO layer was then sputtered on the cleaned glass cover slip (Edwards), and a 200 nm of hydrogenated amorphous silicon layer (a-Si: H) was deposited on the cover slips using plasma-enhanced chemical vapor deposition (PECVD, Oxford2). The hydrogenation during the plasma-enhanced chemical vapor deposition of the a-Si effectively reduced the probability of potential defects and consequently prevented creation of pinholes, enabling OET operation even with 50 nm of the photoconductive a-Si layer (data not shown). Also, after the deposition by PECVD, the a-Si: H layer was slowly cooled down in the nitrogen-filled PECVD chamber to prevent pinhole creation. Just before the SLB formation experiment, the a-Si/ITO substrate was cleaned with a 1:1:5 RCA solution of NH_4OH (ammonium hydroxide) + H_2O_2 (hydrogen peroxide) + H_2O (water) at 80 °C for 15 minutes to oxidize the substrate surface, allowing it to become highly hydrophilic (SiO_2), followed by a thorough rinse with deionized water and a drying with nitrogen.

2.1.3b Formation of SLB in OET and Its Characterization

The first step toward SLB integration with OET was to confirm the SLB formation in the OET. When properly formed, the supported phospholipid-membrane retains the lateral fluidity necessary for the dynamic particle manipulation. The integrated OET device in this work consists of an aqueous solution sandwiched between two flat electrodes: one side is 200 nm in thickness and consists of a hydrogenated amorphous photoconductive silicon (a-Si) layer deposited on top of 100 nm of an indium tin oxide (ITO) layer. The other side consists only of the 100 nm of ITO layer. Again, before experiments, the surfaces of the device substrates were rigorously cleaned with the strongly oxidizing solution.

The SLB was then formed on this hydrophilic, oxidized a-Si surface using a vesicle fusion and rupture method [19, 20]. Briefly, first, a suspension of small unilamellar vesicles (SUV) was made by drying the lipid solution in chloroform in a round-bottom glass flask and then dispersing the dried film in a PBS buffer by sonication. Finally, the solution was passed through 60 nm polycarbonate membrane filters (Avanti, Alabaster, AL) 10 times using a mini-extruder (Avanti, Alabaster, AL). The lipids used in this experiment consisted of DOPC (1,2-dioleoyl-*sn*-glycero-3-phosphocholine, Avanti Polar Lipids, Alabaster, AL) doped with 1 mol % Oregon Green 488 DHPE (1,2-Dihexadecanoyl-*sn*-Glycero-3-Phosphoethanolamine, Invitrogen, Carlsbad, CA). The SUV suspension was mixed at 3:1 (v/v) concentration with phosphate-buffered saline (PBS, pH 7.4; 3.2 mM Na_2HPO_4, 0.5 mM KH_2PO_4, 1.3 mM KCl, 135 mM NaCl), and 50 μL of the resulting solution (1 mg/mL) was placed onto the a-Si device. After 15 min incubation, the photoconductive substrate was immersed in excess DI water to remove

excess SUVs. All procedures were performed without exposing the device surface to air to prevent damage to the formed SLB [21].

The SLB formation SLB and its maintained lateral fluidity were confirmed by fluorescence recovery after bleaching (FRAP) using a home-built confocal microscope [22, 23]. In this membrane characterization experiment, another glass cover slip was placed on the solution on top of the SLB/a-Si. In the FRAP experiment, after photobleaching a 10 μm spot with concentrated laser exposure, I took time-sequential fluorescence images of the membrane. The average fluorescence intensity of the bleached spots exhibited rapid recovery due to the lateral diffusion of fluorescent lipids in the fluid membrane (Fig. 2.1.2a). The recovery data was analyzed using easyFRAP, an open-source software written by MATLAB [24]. Fitting this intensity curve to five samples with a theoretical curve provided their diffusion coefficient, estimated as 8.9 $\mu m^2/s$ (Fig. 2.1.2b). The measured diffusivity was very similar to that of phospholipids on a clean glass cover slip [25, 26], confirming the maintained membrane fluidity on the fabricated a-Si surface.

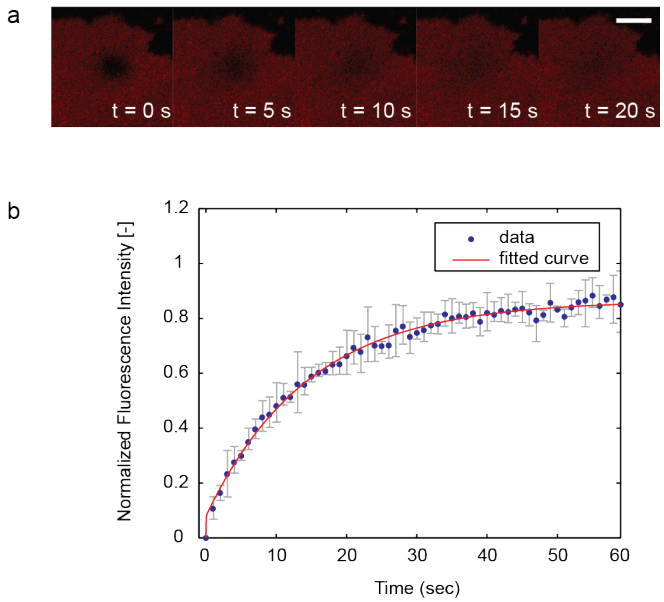

Figure 2.1.2 Fluorescence recovery after photobleaching (FRAP) experiment. (**a**) time-sequential fluorescence images of the SLB formed on the amorphous silicon surface, taken by confocal microscope. The center spot was photobleached with a focused strong laser, and the recovery in its average fluorescence intensity was continuously monitored. The resultant rapid recovery confirmed the maintained fluidity of the lipid membrane on the OET device. Scale bar is 20 μm. (**b)** Plots are the normalized average fluorescence intensity of the bleached spot versus time.

2.1.3c Imaging Setup and Analysis Method

In the following experiments, gold nanoparticles (Au-NPs) tethered on the SLB were optically imaged. In the optical setup shown in Fig. 2.1.3, light from a 100 W halogen lamp passed through a narrow band path filter (546 nm ± 5 nm) was used for illumination and reflectively applied to sample through an objective (40x, NA = 1.0, water immersion, Carl Zeiss, Germany) in an upright microscope (Carl Zeiss). A normal CCD camera (Andor Technology, UK) was employed for imaging membrane-tethered

Au-NPs. The motion of the Au-SPs was mapped with interferometric scattering detection. In essence, the light fields scattered by the object (E_{sca}) and the light reflected by the a-Si substrate (E_{ref}) cause interference, producing signals proportional to $|E_{sca}||E_{ref}|\cos\phi$, where ϕ denotes the phase difference between the two light fields [27, 28]. This interferometric method provides a high-contrast image of the particles. Furthermore, this interferometric effect is sensitive to the distance between the particles and the reflective surface of a-SI, effectively removing the background noise from unbound objects. This setup enables taking time-lapsed images of the laterally diffusing particles at every 50 ms for more than 3,000 frames. The particles' trajectories were collected from the recorded images using the ImageJ program, and MATLAB analyzed their statistics.

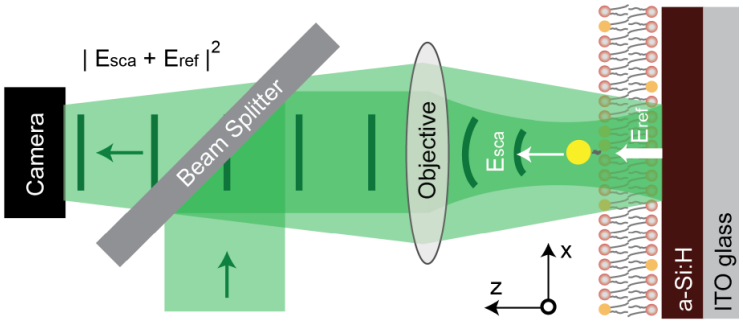

Figure 2.1.3 Imaging setup for interferometric scattering detection of the nanoparticle with an inverted optical microscope (not to scale). With monochromatic illumination applied to the sample, both backscattered light from nanoparticles and reflected light from the silicon surface were collected, generating a high-contrast image of the nanoparticle.

2.1.3d Characterization of Membrane-Tethered Nanoparticles

To characterize particles' diffusive behavior, I chemically tethered the gold nanoparticles to the SLB-containing thiol-ended lipids and confirmed their confinement to (2D) Brownian motion. The SLB used in the following experiments was a mixture of 96 mol % of DOPC and 4 mol % of thiol-ended lipids, PTE-SH (1,2-dipalmitoyl-sn-glycero-3-hosphothioethanol, Avanti, Alabaster, AL). This PTE-SH yields thiol-anchoring groups for selectively tethering the gold nanoparticles to the SLB [29, 30].

The 2D Brownian motion of the SLB-tethered nanoparticles was optically mapped and confirmed by interferometric scattering detection, which provides sufficiently high-contrast images for tracking particles' trajectories (Fig. 2.1.3 makes Fig.2.1.4). Fig. 2.1.4a shows an example trajectory of a single particle, taken by 20 Hz for 350 frames. Continuously constant intensity of the particle in the time-lapsed images confirmed the constant distance from the reflective a-Si surface and the 2D confinement of the particle's motions on the lipid membrane. The mean square displacement (MSD), obtained from 3,000 frames of the trajectories of each 30 particle showed a linear increase with slope = 1 (Fig. 2.1.4b), confirming the diffusive motions of the tethered particles. With the general law of random diffusion, $\langle \Delta r^2 \rangle = 2D\Delta t$, the lateral diffusivity of the particles from the MSD was estimated as 0.280 $\mu m^2/s$. On the other hand, the diffusivity of the same-sized particle (60 nm) in bulk water can be estimated as $D = k_B T/6\pi\eta r =$ 7.31 $\mu m^2/s$, wherein η is the fluid viscosity, k_B is the Boltzmann

constant, and T is the room temperature at 298 K. The measured particles' diffusivity was an order of magnitude smaller than that of particles in bulk water due to the viscous environment and the 2D confinement imposed by the fluidic SLB [31].

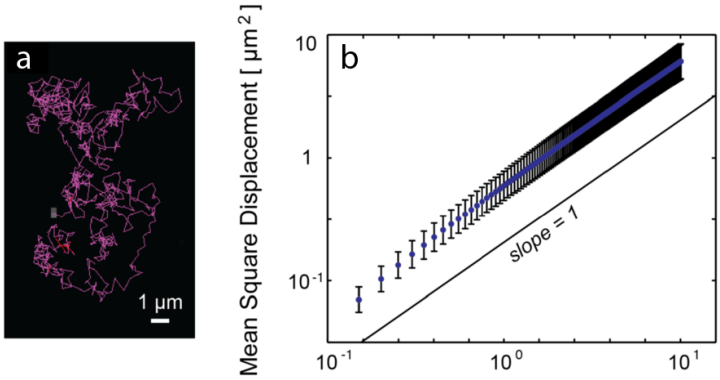

Figure 2.1.4. Two-dimensional Brownian motion of 60 nm gold nanoparticles tethered onto the SLB/a-Si. (**a)** The Brownian motion of the tethered nanoparticles tracked with its constant light intensity confirmed that the distance between the particles and amorphous Si-surface was maintained. (**b**) The mean square displacement (MSD), averaged from the trajectories of the 30 tracked particles, linearly increased with time at slope = 1, confirming their diffusive behavior. The measured diffusivity estimated from the MSD was 0.28 μm^2/s. Here the formed SLB was mixture of 96 mol % of DOPC and 4 mol % of a thiol-ended lipid, PTE-SH.

2.1.4 Results: Demonstration of Particle Manipulations

Finally, the manipulation of SLB-tethered nanoparticles in the OET is demonstrated. In the OET operations, a.c. bias of 10 V p.p. at 100 kHz was applied between the top and bottom ITO layers with a functional generator (GFG-8219A, GW Instek, Taiwan). Simultaneously, the photoconductive electrodes were activated using an orange C.W. laser at a wavelength of 594 nm and at intensities of ~5 W/cm^2. This excitation light was reflectively patterned to the sample using a digital micromirror device (DMD, Texas instruments, TX, USA) and through a 40x water immersion lens in an upright optical microscope. In parallel, silver glue was used to make electrical connections from the device to cables, where the a-Si layer was partially scratched to allow direct contact between the underlying ITO and the cable. Finally, the counter electrode of ITO was placed with a spacer tape (3M) and OET was operated.

For this experiment, the gold nanoparticles were tethered by placing the Au-NP solution on the SLB/a-Si surface and incubating them for 1 hour. After rinsing off the unbound particles with DI water, the resultant sample was submerged in a 1 % PBS buffer in DI water.

Fig 2.1.5a shows the overlapped image of a projected light pattern and randomly distributed tethered gold nanoparticles of 60 nm in diameter. As seen in Fig. 2.1.5a to Fig 2.1.5c, the OET effectively applied the light-induced DEP forces onto the particle and moved them into the light pattern. The histogram shown in Fig 2.1.5d displays time evolution of the particle distribution under the OET operation, confirming the successful collection of particles toward the projected light pattern. After turning off either the applied a.c. bias or the light projection, the DEP forces disappeared and the particles recovered their free (tethered) 2D Brownian motion. In contrast to the low frequency operation, which can induce electrokinetic flows and/or particle aggregation onto the a-Si

surfaces, the SLB-assisted process was reversible and dynamically controllable due to the fluidic property and the 2D confinement provided in the SLB.

To my knowledge, the well-controlled, reversible manipulation of nanoscale particles has been difficult for the conventional OT and OET techniques. Our approach realized it with following advantages: (1) 2D confinement of particles' diffusion imposed by the SLB enables efficiently applying the strong light-induced DEP force near the photoconductive surface; (2) the SLB prevents nonspecific and irreversible binding of the particles onto the device substrate; and (3) the high viscosity of the SLB makes particles resistive to the ionic fluid flow above the electrode surface.

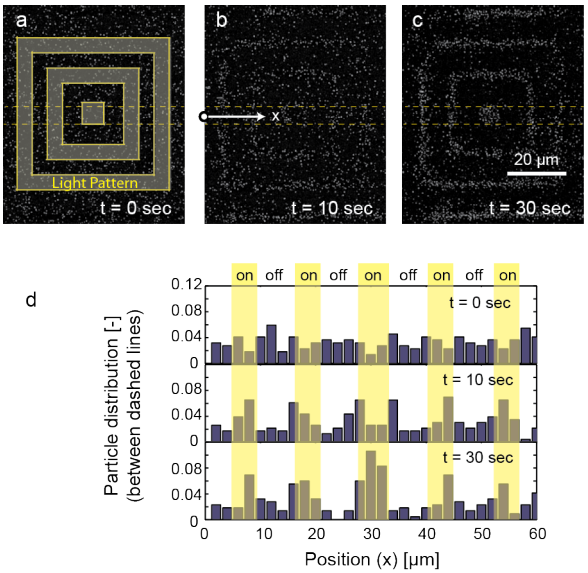

Figure 2.1.5 Manipulation of the nanoparticles tethered to the fluid SLB using the OET. (**a-c)** are the time-sequential images (B/W inverted for visualization) of the gold nanoparticles, showing that they were successfully trapped into the projected light pattern shown in (**a**). After turning off either the a.c. bias or light pattern projection, the particles were released from the DEP forces and recovered their free (tethered) 2D Brownian motion. (**d)** Particle distribution under the OET operation, which was normalized by the total number of particles in a section in each image (defined with dashed lines). The time-dependent distribution confirmed the collection of the nanoparticles into the projected light pattern.

Simply by decreasing the frequency from 100 kHz, our configuration enables manipulation of even smaller particles using the electro-osmosis effect. However, we found that operating the device at a frequency lower than 20 kHz can induce instability of the supported bilayers. Also at the low frequency, interestingly, continuous monitoring of the fluorescently labeled membrane showed the production of many uniform lipid vesicles from the area illuminated (data not shown). This is similar to a commonly known vesicle production process, electroformation [32]. This finding may lead to the development of a new method that can generate vesicles production from a targeted area in the SLB on demand.

In addition, interestingly, I noticed that not all the tethered nanoparticles kept showing the infinitely continuous diffusion. Some of them temporally trapped on the membrane but, after seconds, they restarted the normal 2D diffusion. This kind of behavior, seemingly different diffusive process co-exists in the single trajectory, has recently attracted scientific interest, categorized as non-Brownian motion [33-35]. While

our configuration can be interesting platform for studying this, in this work, we intentionally omitted those temporally trapped particles from the MSD analysis (Fig. 2.1.4b) for characterizing the kinetic property of the tethered particles.

2.1.5 Summary and Future Directions

In summary, the integration of the supported lipid bilayer with optoelectronic tweezers was proposed and experimentally demonstrated, enabling 2D manipulation of many nanoparticles in desired patterns. The capability of manipulating nanoparticles as small as 60 nm diameters holds great potential for controlling many particles simultaneously for the study of various 2D physical systems and underlying Brownian mechanics. The DEP force maximized at the 2D membrane surface can be used to controllably fractionate and/or sort the small objects with high selectivity [36-38] and to transport a number of nanoparticles to *in vitro* cells as drug vehicles [39-40]. Moreover, because the lipid bilayer is an essential component of biological cell membranes, the SLB has been extensively used with living cells to mimic cell-to-cell interfaces for the study of intercellular interactions [41-42]. Through the nanoparticles tethered on the SLB, our technique will facilitate the research of mechanotransductions and molecular sensing at the cellular interface in the near future.

References

1. Moffitt, J. R., Chemla, Y. R., Smith, S. B. & Bustamante, C. Recent Advances in Optical Tweezers. *Annu. Rev. Biochem.* **77,** 205–228 (2008).
2. Visscher, K., Gross, S. P. & Block, S. M. Construction of multiple-beam optical traps with nanometer-resolution position sensing. *IEEE J. Select. Topics Quantum Electron.* **2,** 1066–1076 (1996).
3. Chiou, P.-Y., Ohta, A. T. & Wu, M. C. Massively parallel manipulation of single cells and microparticles using optical images. *Nature* **436,** 370–372 (2005).
4. Hsu, H.-Y. *et al.* Phototransistor-based optoelectronic tweezers for dynamic cell manipulation in cell culture media. *Lab Chip* **10,** 165 (2009).
5. Hwang, H. *et al.* Interactive manipulation of blood cells using a lens-integrated liquid crystal display based optoelectronic tweezers system. *Electrophoresis* **29,** 1203–1212 (2008).
6. Shah, G. J., Ohta, A. T., Chiou, E. P. Y., Wu, M. C. & Kim, C.-J. C. EWOD-driven droplet microfluidic device integrated with optoelectronic tweezers as an automated platform for cellular isolation and analysis. *Lab Chip* **9,** 1732 (2009).
7. Ohta, A. T. *et al.* Dynamic Cell and Microparticle Control via Optoelectronic Tweezers. *J. Microelectromech. Syst.* **16,** 491–499 (2007).
8. Valley, J. K., Jamshidi, A., Ohta, A. T., Hsu, H.-Y. & Wu, M. C. Operational Regimes and Physics Present in Optoelectronic Tweezers. *J. Microelectromech. Syst.* **17,** 342–350.
9. Jamshidi, A. *et al.* Dynamic manipulation and separation of individual semiconducting and metallic nanowires. *Nature Photonics* **2,** 86–89 (2008).
10. Zarowna-Dabrowska, A. *et al.* Miniaturized optoelectronic tweezers controlled by GaN micro-pixel light emitting diode arrays. *Opt. Express* **19,** 2720–2728 (2011).

11. Yang, S.-M. *et al.* Dynamic manipulation and patterning of microparticles and cells by using TiOPc-based optoelectronic dielectrophoresis. *Optics Letters* **35,** 1959–1961 (2010).
12. Tsutsui, H. *et al.* Efficient Dielectrophoretic Patterning of Embryonic Stem Cells in Energy Landscapes Defined by Hydrogel Geometries. *Ann Biomed Eng* **38,** 3777–3788 (2010).
13. Jamshidi, A. *et al.* NanoPen: Dynamic, Low-Power, and Light-Actuated Patterning of Nanoparticles. *Nano Lett.* **9,** 2921–2925 (2009).
14. Ota, S., Wang, S., Wang, Y., Yin, X. & Zhang, X. Lipid Bilayer-Integrated Optoelectronic Tweezers for Nanoparticle Manipulations. *Nano Lett.* **13,** 2766–2770 (2013).
15. Richter, R. P., Bérat, R. & Brisson, A. R. Formation of Solid-Supported Lipid Bilayers: An Integrated View. *Langmuir* **22,** 3497–3505 (2006).
16. Kung, L. A., Kam, L., Hovis, J. S. & Boxer, S. G. Patterning Hybrid Surfaces of Proteins and Supported Lipid Bilayers. *Langmuir* **16,** 6773–6776 (2000).
17. Tanaka, M. & Sackmann, E. Polymer-supported membranes as models of the cell surface. *Nature Cell Biology* **437,** 656–663 (2005).
18. Castellana, E. T. & Cremer, P. S. Solid supported lipid bilayers: From biophysical studies to sensor design. *Surface Science Reports* (2006).
19. Cremer, P. S. & Boxer, S. G. Formation and Spreading of Lipid Bilayers on Planar Glass Supports. *J. Phys. Chem. B* **103,** 2554–2559 (1999).
20. Groves, J. T., Ulman, N. & Boxer, S. G. Micropatterning fluid lipid bilayers on solid supports. *Science* **275,** 651–653 (1997).
21. Deng, Y. *et al.* Fluidic and Air-Stable Supported Lipid Bilayer and Cell-Mimicking Microarrays. *J. Am. Chem. Soc.* **130,** 6267–6271 (2008).
22. Sprague, B. L., Pego, R. L., Stavreva, D. A. & McNally, J. G. Analysis of Binding Reactions by Fluorescence Recovery after Photobleaching. *Biophysical Journal* **86,** 3473–3495 (2004).
23. Sprague, B. L., Pego, R. L., Stavreva, D. A. & McNally, J. G. Analysis of Binding Reactions by Fluorescence Recovery after Photobleaching. *Biophysical Journal* **86,** 3473–3495 (2004).
24. Rapsomaniki, M. A. *et al.* easyFRAP: an interactive, easy-to-use tool for qualitative and quantitative analysis of FRAP data. *Bioinformatics* **28,** 1800–1801 (2012).
25. Seu, K. J. *et al.* Effect of Surface Treatment on Diffusion and Domain Formation in Supported Lipid Bilayers. *Biophysical Journal* **92,** 2445–2450 (2007).
26. Tabarin, T., Martin, A., Forster, R. J. & Keyes, T. E. Poly-ethylene glycol induced super-diffusivity in lipid bilayer membranes. *Soft Matter* **8,** 8743 (2012).
27. Krishnan, M., Mojarad, N., Kukura, P. & Sandoghdar, V. Geometry-induced electrostatic trapping of nanometric objects in a fluid. *Nature* **467,** 692–695 (2010).
28. Mojarad, N. & Krishnan, M. Measuring the size and charge of single nanoscale objects in solution using an electrostatic fluidic trap. *Nature Nanotechnology* **7,** 448–452 (2012).
29. Ba, H., Rodríguez-Fernández, J., Stefani, F. D. & Feldmann, J. Immobilization of

Gold Nanoparticles on Living Cell Membranes upon Controlled Lipid Binding. *Nano Lett.* **10,** 3006–3012 (2010).
30. Yang, Y.-H. & Nam, J.-M. Single Nanoparticle Tracking-Based Detection of Membrane Receptor−Ligand Interactions. *Anal. Chem.* **81,** 2564–2568 (2009).
31. Yoshina-Ishii, C. *et al.* Diffusive Dynamics of Vesicles Tethered to a Fluid Supported Bilayer by Single-Particle Tracking. *Langmuir* **22,** 5682–5689 (2006).
32. Angelova, M. I. & Dimitrov, D. S. Liposome electroformation. *Faraday Discuss. Chem. Soc.* **81,** 303 (1986).
33. Wang, B., Kuo, J., Bae, S. C. & Granick, S. When Brownian diffusion is not Gaussian. *Nature Materials* **11,** 481–485 (2012).
34. Sharma, N. N., Ganesh, M. & Mittal, R. K. Non-Brownian Motion of Nanoparticles: An Impact Process Model. *IEEE Trans. Nanotechnology* **3,** 180–186 (2004).
35. Wang, B., Anthony, S. M., Bae, S. C. & Granick, S. Anomalous yet Brownian. *Proc. Natl. Acad. Sci. U.S.A.* **106,** 15160–15164 (2009).
36. Xiao, K. & Grier, D. G. Multidimensional optical fractionation of colloidal particles with holographic verification. *Phys. Rev. Lett.* **104,** 028302 (2010).
37. Milne, G., Rhodes, D., MacDonald, M. & Dholakia, K. Fractionation of polydisperse colloid with acousto-optically generated potential energy landscapes. *Optics letters* **32,** 1144–1146 (2007).
38. Shi, J., Huang, H., Stratton, Z., Huang, Y. & Huang, T. J. Continuous particle separation in a microfluidic channel via standing surface acoustic waves (SSAW). *Lab Chip* **9,** 3354 (2009).
39. Fan, D. *et al.* Subcellular-resolution delivery of a cytokine through precisely manipulated nanowires. *nature nanotechnology* **5,** 545–551 (2010).
40. Groves, J. T. & Kuriyan, J. Molecular mechanisms in signal transduction at the membrane. *Nature structural & molecular biology* (2010).
41. Shen, K., Tsai, J., Shi, P. & Kam, L. C. Self-Aligned Supported Lipid Bilayers for Patterning the Cell−Substrate Interface. *J. Am. Chem. Soc.* **131,** 13204–13205 (2009).
42. Manz, B. N. & Groves, J. T. Spatial organization and signal transduction at intercellular junctions. *Nat Rev Mol Cell Biol* **11,** 342–352 (2010).

2.2 Optoelectrophoresis in Nanofluidics

2.2.1 Motivation

The purpose of this work is to realize optic manipulation of truly small biological molecules. Technologies that enable optically trapping, accumulating, and sorting of biological molecules with high spatial control are invaluable for a wide field of biophysics research and biomedical sensing applications. In the previous sections (Sections 1.2 and 2.2), I have investigated and experimentally demonstrated the optics-based particle manipulation techniques. Both optical tweezers and optoelectronic tweezers are very powerful, but it is still practically impossible to manipulate biological molecules with much smaller dimensions than the typical inorganic nanoparticles and a smaller index contrast with water [1]. While fluidic [2] and electrostatic [3, 4] methods can move a large number of small molecules such as proteins and a small fraction of DNAs at bulk scales, no technology exists to manipulate the molecules at good addressability. In this exploratory work, I utilize the SLB/OET system previously used in Section 2.1 to show the potential of the novel concept optoelectrophoresis in the nanofluidic scales. The SLB is used in this demonstration because the SLB is essentially a two-dimensional fluid that can remain below the electric double-layer thickness formed on the optoelectronic device surface. In this section, I will show the proof-of-concept manipulation of charged lipid molecules that have physical dimensions below 3 nm in all directions, which will lead to a more general breakthrough for creating the new field of optoelectronics in the nanofluidic scales.

2.2.2 Introduction to Nanofluidics

The nanofluidics research field studied and applied phenomena that involve fluid's or particles' motion through or past structures with features less than 100 nm in one or more directions [5, 6]. In this scale, unlike microfluidics that utilize pressure difference to drive the fluid flows, the fluids at the nanoscales are significantly affected by the property of the wall. Unlike the system at bulk scales, where ions in a solution are attracted to the wall surface to screen out the electrostatic potential after a so-called electric double layer (EDL with thickness of Debye length), the electric field can remain in the nanofluidic systems. This is because there is not enough space for the ions to screen the surface potential within dimensions smaller than the Debye length. Also, the imposed physical constraints induce the fluid to have very high fluidic resistance in a channel, high frictional interaction with the wall, and consequently increased viscosity. Thus, nanofluidics is essentially a surface fluidics [6].

The enhanced electrostatic interaction is particularly important for a wide range of applications because the surface charge of the nanofluidic walls can be well controlled. One example is the nanocapillary array membrane (NCAM) [7-9]. The surface of NCAM contains surface charges and induces reorganization of ion distribution near the surface. This EDL may completely span the width of a nanopore, causing changes in the fluid composition and its property inside the structure. Inside the pore, the population of ions counteracting the surface charge significantly exceeds that of attracted ions. Such phenomena can be used for selectively manipulating charged molecules along the pore length to enable molecular sorting, which is not possible in larger structures. For

example, replacing the agarose gels used for DNA separations with nanostructured solid-state materials is a goal of nanofluidic technologies [10-12].

Electric Double Layers and Free Energy between a Plane and Particles

Surface charges at a solid interface are typically fixed such that an oppositely charged region of counter ions develops in the liquid to maintain the neutrality of the solid-liquid interface [6]. This screening region is called EDL. As mentioned in the previous section, the nanofluidic channel's dimensions smaller than the EDL often play key roles in enabling unique functions of nanofluidic technologies. If the channel dimension is much larger than the EDL thickness, Debye length, there is no observable unique behavior of ions and charged molecules in the channel (Fig. 2.2.1a). If the channel opening becomes comparable to the Debye length, the surface charge of channel walls causes significant modification of ionic or charge molecules' population inside the channel (Fig. 2.2.1b). In most cases, ions or molecules containing charges countering the channel wall's charge can remain there.

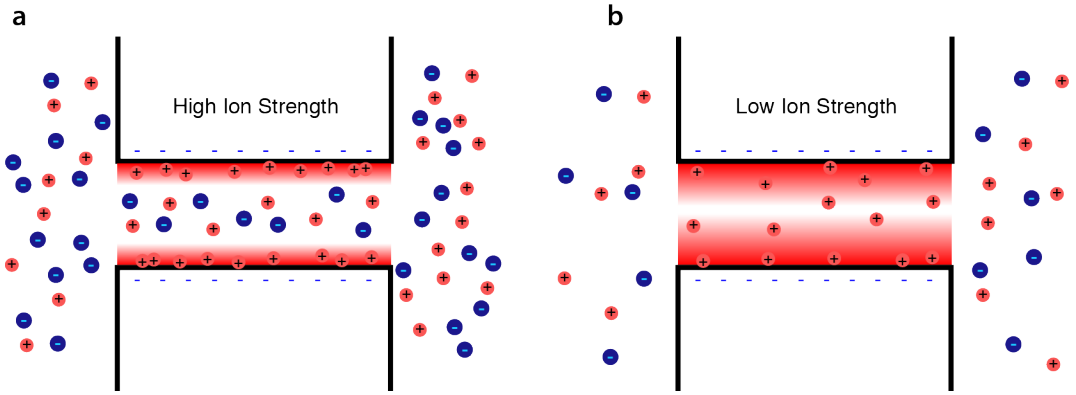

Figure 2.2.1 Schematic of electrical double layer (EDL), depicted as gradient red area. **(a)** At high ionic strength, it is very thin, such that all ions can almost freely pass through the nanochannel. **(b)** At low ionic strength, the EDL thickness expands over the nanochannel dimensions such that the channel becomes counterion-selective.

The Poission-Boltzmann equation for the electrostatic potential induced by the modified distribution of charged ions or molecules near the fixed charge on the solid surface is given with second-order partial differential equation for distance z as follows [6, 13, 14]:

$$\nabla^2\psi = \frac{d^2\psi}{dz^2} = -\frac{e}{\varepsilon_0\varepsilon_r}\sum_i n_0 z_i e^{-z_i e\psi(z)/k_B T} \qquad (2.2.1)$$

where ψ is the potential, e is the charge of single electron, ε_0 and ε_r are the vacuum and relative permittivity, and n_0 is the bulk volume density given with $n_0 = 1000 N_A c_i$, where c_i is the molar concentration of ions or molecules. Assuming the potential is small enough everywhere and expanding the exponential term in equation (2.2.1) leads to the Debye-Huckel approximation [6]:

$$\nabla^2\psi = \frac{d^2\psi}{dz^2} = \kappa^2\psi \qquad (2.2.2)$$

$$\kappa = \left(\frac{e^2 \sum_i n_0 z_i^2}{\varepsilon_0 \varepsilon_r k_B T}\right)^{1/2} \qquad (2.2.3)$$

where κ is the Debye-Huckel parameter and is mainly dependent on n_0 and the Debye length is given as $\lambda_D = \kappa^{-1}$, simplifying the estimation of EDL thickness with varied solute concentrations. For example, λ_D is below 1 nm at high ion concentration of KCL solution at 1 M, while λ_D is around 100 nm at low ion concentration of KCL solution at 10^{-5} M. Thus, the EDL at such low concentrations expands to fill the nanofluidic device's opening to cause its unique phenomena.

2.2.3 Nanofluidics-based Manipulation of Molecules and Particles

Recent nanofluidic technology engineered the EDL thickness to achieve molecular sorting and nanoparticle trapping. For example, controlling the protein transport in the nanofluidic channel by a gate voltage V_g between the microchannels was demonstrated as shown in Figs. 2.2.2a and b. With the negative V_g, the positively charged protein can diffuse through the nanochannel, whereas the same protein is repelled with positive V_g [15]. A charged nanoscopic object's trapping is demonstrated without any applied electrostatic energy. As shown in Fig. 2.2.2c, nanofluidic space is structured in channels made of glass that is intrinsically negatively charged. As a result, negatively charged nanoparticles or lipid vesicles experience repelling forces from the channel wall and are trapped in the space [16, 17].

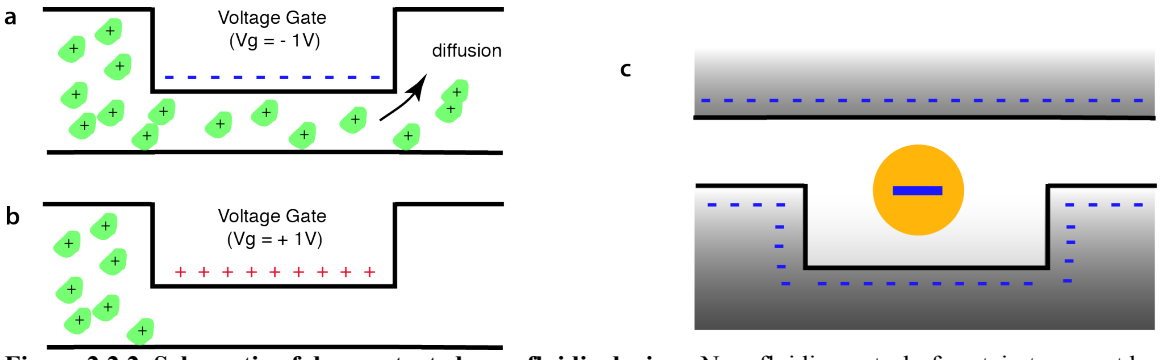

Figure 2.2.2 Schematic of demonstrated nanofluidic devices. Nanofluidic control of protein transport by a gate voltage between the microchannels **(a)** and electrostatic fluidic trap with glass nanofluidic structures that have negatively charged walls **(b).**

These demonstrated techniques are based on fabricated electronic structures or on the electrostatically fixed structures, and no one has ever tried to integrate them with optically controlled functions.

2.2.4 Optoelectrophoresis in Nanofluidics

The general concept of optoelectrophoresis in nanofluidic, shown in Fig. 2.2.3 can be understood in three steps: (1) light patterns locally excite the carriers inside photo-conductive semiconductors; (2) the optoelectronic modification of semiconductor changes its surface charge distribution and consequently the electrostatic potential shape within the nanofluidic solution; (3) the created electrostatic potential generates electrostatic forces on the charge molecules or particles. In this work, the SLB is utilized

since the assembly of lipid molecules remains diffusive inside the electric double layer. When the SLB is composed of charge lipids and uncharged lipids, only charged lipid molecules will be inevitably affected by the surface charge redistribution induced by light illumination. This device actively enables the first optical control of biological molecules and potentially enables application of large electrostatic forces with applied bias.

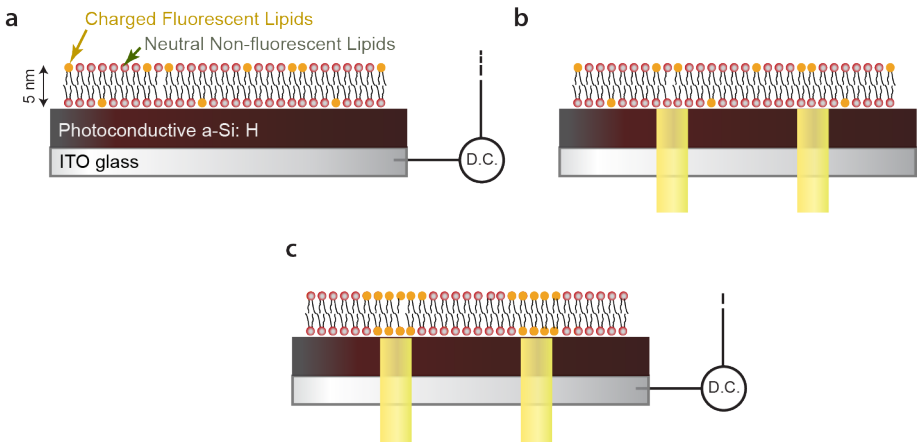

Figure 2.2.3 Schematic of optoelectophoresis in nanofluidics with an example system of a supported lipid bilayer membrane containing both fluorescent charged lipids and nonfluorescent neutral lipids. When light patterns locally modified the optoelectronic circuits in the OET device under dc bias voltage, they modified the surface charge distribution on the device surface and thus created electrostatic potentials within the EDL thickness. In the case of SLB, with either bias voltage or light patterns, there is no change in the electrostatic potential landscape **(a)** and **(b)**. However, when both are applied at the same time (c), only the charged one will feel the optophoretic forces. The lipid membrane is an ideal environment because it can retain the fluidic environment in the 2D space near the substrate surface.

In this experiment, in addition to the OET device demonstrated in Section 2.1, microfabricated gold electrodes were placed on the a-Si surface near the SLB area. Different from conventional OET devices, dc voltage is applied between the pre-fabricated electrode on the a-Si layer and the ITO layer below the photoconductive a-Si layer. This configuration is favored because the presence of electrodes on the surface where the SLB sits allows them to share the same electric double layer. Within this same double layer, ions cannot screen the electrostatic potential created by the surface in all three dimensions. If the counter ITO electrode is used in the conventional manner, because the aqueous solution above the SLB is at bulk, ions can form a complete double layer such that the concept does not work.

The combination of charged fluorescent lipids and uncharged nonfluorescent lipids was used to form a single SLB on the a-Si surface of the OET device using the standard vesicle rupture method used in Section 2.1. The lipid membrane used in this experiment consisted of DOPC (1,2-dioleoyl-*sn*-glycero-3-phosphocholine, Avanti Polar Lipids, Alabaster, AL) doped with 4 mol % Oregon Green 488 DHPE (1,2-Dihexadecanoyl-*sn*-Glycero-3-Phosphoethanolamine, Invitrogen, Carlsbad, CA). While DOPC is neutral, the Oregon Green is negatively charged. The same FRAP experiment was performed as in Section 2.1 and confirmed retained diffusivity of 9.0 $\mu m^2/s$.

The optical setup is similar to what was used in the previous section, 2.1, but is coupled with the normal fluorescence imaging system, consisting of excitation (ET470/40x) and emission (ET525/50m) filter and dichroic mirror (T495lpxr) for the

green emitting dyes (Fig. 2.2.2). This emission filter blocks the laser excitation at 594 nm, enabling the fluorescence imaging during laser light patterning. The excitation light intensity used in the experiment was reduced because it should not affect the optoelectronic modulation of the surface charges. Before the manipulation experiment, I confirmed that the orange laser light illumination did not cause any detectable photobleaching.

2.2.5 Result: Demonstration of Charged Lipid Manipulations

In the manipulation experiment, 1V of dc bias voltage was applied between the electrode and the ITO layer and a laser spot was patterned on the a-Si layer using the DMD projector.

When a circular laser spot was projected in the SLB on the a-Si layer, containing both fluorescent charged lipids and nonfluorescent neutral lipids with applied bias in the device, the continuous increase in the fluorescence intensity in the laser-illuminated area was observed (Figs. 2.2.4a–e), confirming the dynamic rearrangement of charged lipid molecules. The original fluorescence imaging before applying the bias voltage was used as a reference. When the fluorescence intensity profile was plotted according to the x-axis shown in the Fig. 2.2.4a, the time evolution in the intensity profile was visualized as shown in Fig. 2.2.4f. When plotting the averaging fluorescence intensity of the center part of the laser spot with time in Fig. 2.2.4g, rapid intensity increase of close to 5 min was observed. The increase confirmed, again, the accumulation of the charged fluorescent lipids in the optoelectrically generated electrostatic potential well. After 5 minutes, the plateau indicated that the total charge of the accumulated charged lipids reached the electrostatic charge induced by the optoelectronic device. The total concentration of fluorescent lipids was increased up to 20 times, which is one order of magnitude larger than the previous report, to our knowledge [19].

Furthermore, to demonstrate the flexibility and potential of the concept of optoelectrophoretic manipulation of molecules, an arbitrarily formed light pattern was projected into the SLB/OET device. When the concentric light squares are projected (Fig. 2.2.5a) onto the SLB that has uniform distribution of fluorescent charged lipids (Fig. 2.2.5b), the induced electrostatic charge on the device surface drives the rearrangement of fluorescent lipids continuously (Fig. b-d). In this case, the bias voltage was applied oppositely such that the negatively charged lipids were driven away from the light patterns. The slightly inhomogeneous movement from the light pattern was most likely because of imperfect uniformity in the intensity over the whole light pattern and the original shape of the SLB itself. The applied bias was then released, resulting in the disappearing of the optoelectrically induced electrostatic charge from the device surface and recovery of free diffusion of charged molecules in the SLB, indicating the minimal photo-induced damage in the SLB. This recovery was observed in Figs. 2.2.5 e–f. The fluorescence image was taken every 1 min. This experiment thus successfully demonstrated the light-pattern–induced electrostatic generation in the optoelectronic device and optoelectrophoresis of charged molecules in the nanofluidic scales.

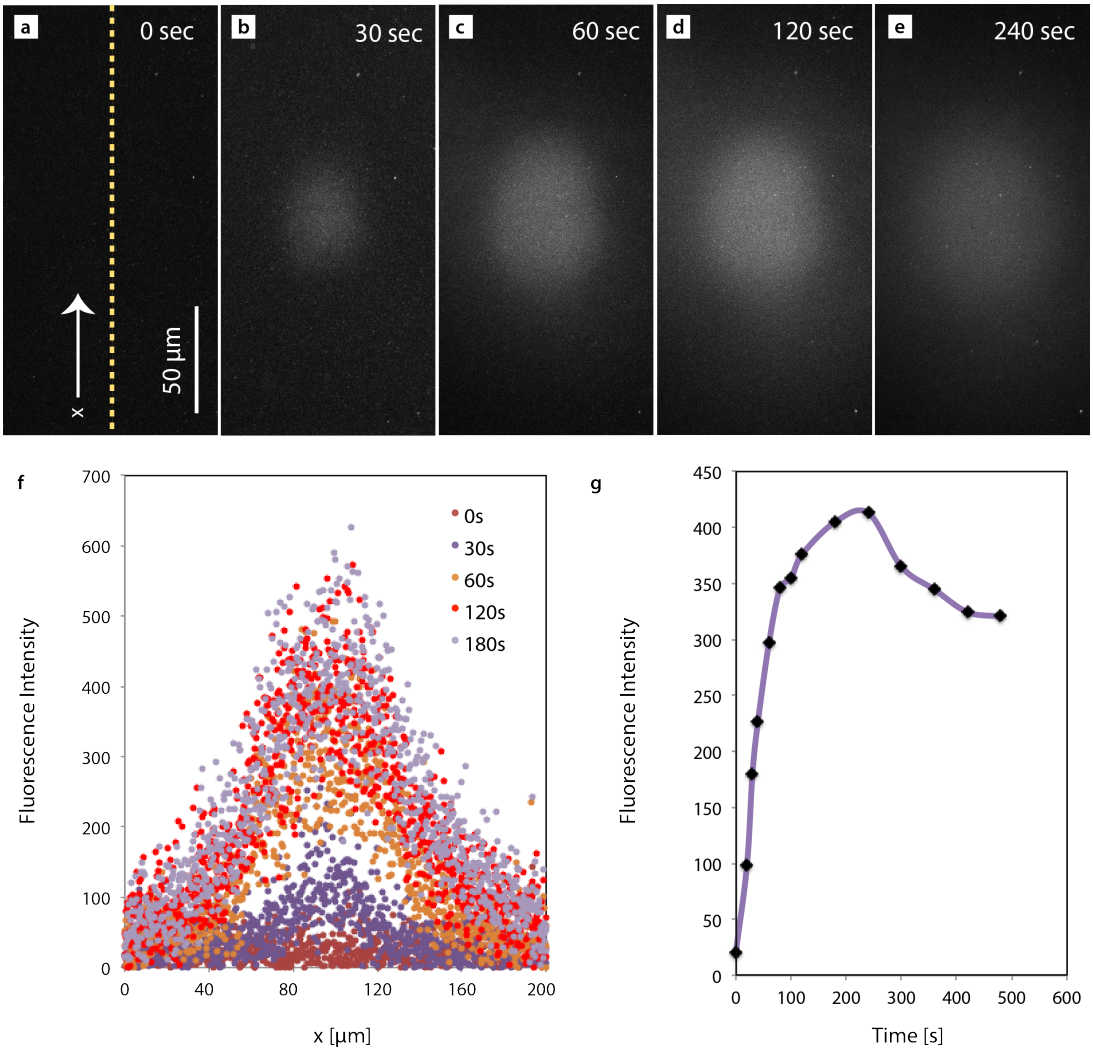

Figure 2.2.4 Concentration of fluorescent charged lipid molecules with patterned laser light spot in the optoelectronic device. **(a)–(e)** shows the time-sequential fluorescence image of the supported lipid bilayer containing both fluorescent charged lipids and nonfluorescent neutral lipids, demonstrating the increase in fluorescence intensity around the laser spot. **(f)** is the intensity profile along the x-axis shown in **(a),** and **(g)** is the average fluorescence intensity evolution versus time in the laser spot.

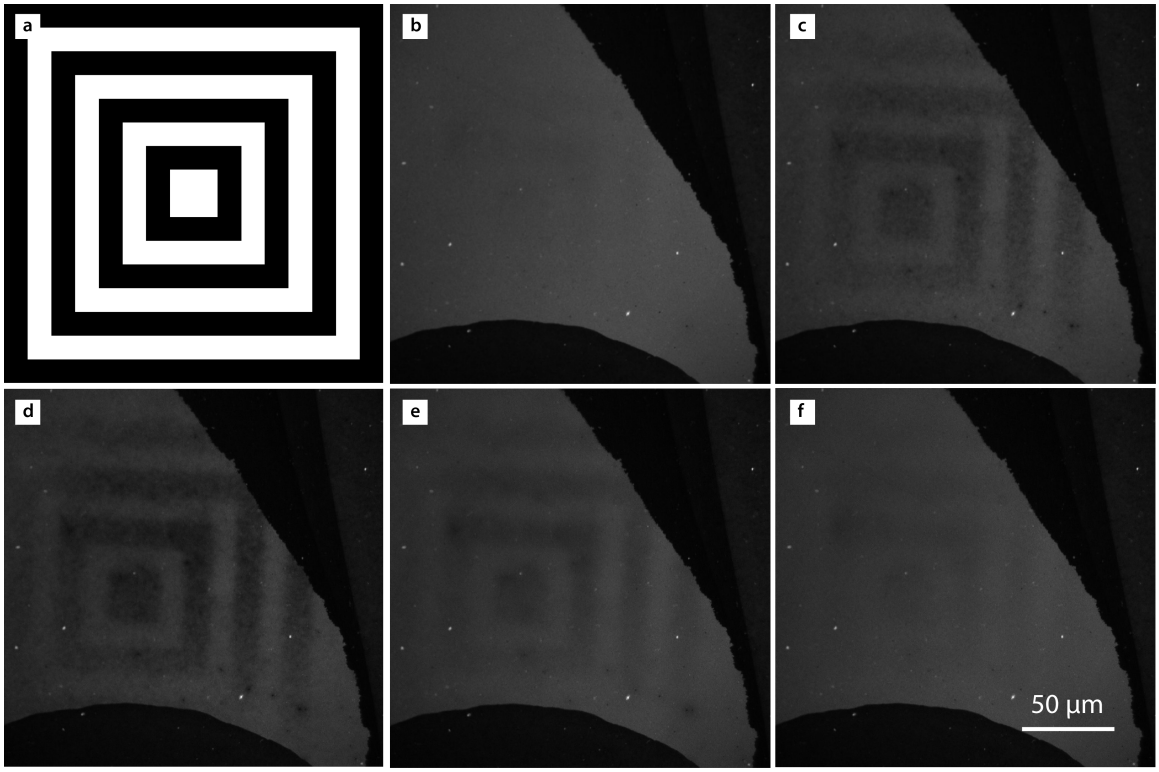

Figure 2.2.5 Dynamic manipulation of the fluorescent lipids in the SLB by simultaneously applying patterned light illumination and the dc voltage bias in the OET. **(a)** is the example light pattern used in the experiment. **(b)–(d)** is the lipid driving process with both light and voltage. After **(d)**, the voltage bias was turned off, returning the lipids to free diffusion and resulting in the recovery of uniform fluorescence intensity distribution **(d)-(f)**.

2.2.6 Summary and Future Directions

In summary, I provided a proof-of-concept demonstration of optoelectrophoresis at the nanofluidic scales by manipulating the fluorescent charged lipids within the supported lipid bilayer. Considering the significant potential applications in the SLB and membrane proteins that can be studied in the SLB, this technology has immediate applications in biological sensing and in the study of membrane proteins' collective behavior in the natural environment. Moreover, the concept of optoelectrophoresis in the nanofluidic physical environment should be applicable in general. I foresee its significant importance in the general optics-based manipulation of truly small molecules and particles. As the electrophoresis is intrinsically free from the particles' size limit, the method can generate larger forces on extremely small charged particles than the conventional optical tweezers and optoelectronic tweezers are capable of. This will enable optical study of single fluorescent molecules in a free solution in a flexible manner [20-25] and optical construction of nanomaterial-based structures such as dynamically reconfigurable optical metamaterials [26-28]. Moreover, the flexibility of light-patterned modification of electrostatic charges in the nanofluidic environment will open the opportunity for the optically reconfigurable nanofluidic circuits. One of the general hurdles for the nanofluidic device community is its small flexibility in designing electronic functions in the nanofluidic devices due to the intrinsic difficulty of its

fabrication and possible integration of electronic functions [29, 30]. Because the light pattern can be remotely and dynamically reconfigurable with high resolution at the diffraction limit (< 1μm), complex and dynamic imposition of electronic functions in the nanofluidic device will be possible, finding significance in the micro-total-analytical-systems and beyond.

References

1. Weiss, S. Fluorescence Spectroscopy of Single Biomolecules. *Science* **283,** 1676–1683 (1999).
2. Armani, M., Chaudhary, S., Probst, R. & Shapiro, B. Using feedback control and micro-fluidics to steer individual particles. in *18th IEEE International Conference on Micro Electro Mechanical Systems, 2005. MEMS 2005.* 855–858 (2005).
3. Meyers, J. A., Sanchez, D., Elwell, L. P. & Falkow, S. Simple agarose gel electrophoretic method for the identification and characterization of plasmid deoxyribonucleic acid. *J. Bacteriol.* **127,** 1529–1537 (1976).
4. Garner, M. M. & Revzin, A. A gel electrophoresis method for quantifying the binding of proteins to specific DNA regions: application to components of the Escherichia coli lactose operon regulatory system. *Nucl Acids Res* **9,** 3047–3060 (1981).
5. Sparreboom, W., van den Berg, A. & Eijkel, J. C. T. Principles and applications of nanofluidic transport. *nature nanotechnology* **4,** 713–720 (2009).
6. Schoch, R., Han, J. & Renaud, P. Transport phenomena in nanofluidics. *Rev. Mod. Phys.* **80,** 839–883 (2008).
7. Temperature-controlled flow switching in nanocapillary array membranes mediated by poly(N-isopropylacrylamide) polymer brushes grafted by atom transfer radical polymerization. **23,** 305–311 (2007).
8. Fa, K., Tulock, J. J., Sweedler, J. V. & Bohn, P. W. Profiling pH gradients across nanocapillary array membranes connecting microfluidic channels. *J. Am. Chem. Soc.* **127,** 13928–13933 (2005).
9. Kuo, T.-C. *et al.* Nanocapillary arrays effect mixing and reaction in multilayer fluidic structures. *Angew. Chem. Int. Ed. Engl.* **43,** 1862–1865 (2004).
10. Turner, S., Cabodi, M. & Craighead, H. Confinement-Induced Entropic Recoil of Single DNA Molecules in a Nanofluidic Structure. *Phys. Rev. Lett.* **88,** 128103 (2002).
11. Tegenfeldt, J. O. *et al.* Micro- and nanofluidics for DNA analysis. *Anal Bioanal Chem* **378,** 1678–1692 (2004).
12. Liang, X. & Chou, S. Y. Nanogap Detector Inside Nanofluidic Channel for Fast Real-Time Label-Free DNA Analysis. *Nano Lett.* **8,** 1472–1476 (2008).
13. Hunter, R. J., *Zeta Potential in Colloid Science,* Academic, London,)1981).
14. Overbeek, J. T. G., in *Colloid Science*, edited by H. R. Kruyt, *Elsevier*, Amsterdam, **1**, (1952).
15. Karnik, R., Castelino, K. & Majumdar, A. Field-effect control of protein transport in a nanofluidic transistor circuit. *Appl. Phys. Lett.* **88,** 123114 (2006).
16. Krishnan, M., Mojarad, N., Kukura, P. & Sandoghdar, V. Geometry-induced

electrostatic trapping of nanometric objects in a fluid. *Nature* **467,** 692–695 (2010).
17. Mojarad, N. & Krishnan, M. Measuring the size and charge of single nanoscale objects in solution using an electrostatic fluidic trap. *nature nanotechnology* **7,** 448–452 (2012).
18. Richter, R. P., Bérat, R. & Brisson, A. R. Formation of Solid-Supported Lipid Bilayers: An Integrated View. *Langmuir* **22,** 3497–3505 (2006).
19. Bao, P. *et al.* On-chip alternating current electrophoresis in supported lipid bilayer membranes. *Anal. Chem.* **84,** 10702–10707 (2012).
20. Wang, Q., Goldsmith, R. H., Jiang, Y., Bockenhauer, S. D. & Moerner, W. E. Probing single biomolecules in solution using the anti-Brownian electrokinetic (ABEL) trap. *Acc. Chem. Res.* **45,** 1955–1964 (2012).
21. Schlau-Cohen, G. S., Wang, Q., Southall, J., Cogdell, R. J. & Moerner, W. E. Single-molecule spectroscopy reveals photosynthetic LH2 complexes switch between emissive states. *Proc. Natl. Acad. Sci. U.S.A.* **110,** 10899–10903 (2013).
22. Wang, Q. & Moerner, W. E. Lifetime and spectrally resolved characterization of the photodynamics of single fluorophores in solution using the anti-Brownian electrokinetic trap. *J. Phys. Chem. B* **117,** 4641–4648 (2013).
23. Jiang, Y. *et al.* Sensing cooperativity in ATP hydrolysis for single multisubunit enzymes in solution. *Proc. Natl. Acad. Sci. U.S.A.* **108,** 16962–16967 (2011).
24. Goldsmith, R. H. & Moerner, W. E. Watching conformational- and photodynamics of single fluorescent proteins in solution. *Nature Chem* **2,** 179–186 (2010).
25. Cohen, A. E. & Moerner, W. E. Principal-components analysis of shape fluctuations of single DNA molecules. *Proc. Natl. Acad. Sci. U.S.A.* **104,** 12622–12627 (2007).
26. Lee, J. H., Wu, Q. & Park, W. Metal nanocluster metamaterial fabricated by the colloidal self-assembly. *Optics letters* **34,** 443–445 (2009).
27. Gardner, D. F., Evans, J. S. & Smalyukh, I. I. Towards Reconfigurable Optical Metamaterials: Colloidal Nanoparticle Self-Assembly and Self-Alignment in Liquid Crystals. *Molecular Crystals and Liquid Crystals* **545,** 3/[1227]–21/[1245] (2011).
28. Rogach, A. L. Binary superlattices of nanoparticles: self-assembly leads to "metamaterials". *Angew. Chem. Int. Ed. Engl.* **43,** 148–149 (2004).
29. Guan, W., Fan, R. & Reed, M. A. Field-effect reconfigurable nanofluidic ionic diodes. *Nature Communications* **2,** 506–8 (1AD).
30. Gijs, M. Device physics: Will fluidic electronics take off? *Nature Nanotechnology* **2**, 268 – 270, (2007).

2.3 Plasmonic Brownian Ratchet

2.3.1 Introduction to Nanomanipulation Using Near-Field Optics

Photonics-based Particle Manipulation

Trapping and transport of nanoscopic objects using photonics technology has become increasingly important for microfluidic and lab-on-a-chip applications [1]. Conventional optical tweezers have played important roles in biophysics [2-4] and soft-condensed matter physics [5-7], while the trapping size is intrinsically limited by diffraction. As a result, it is still practically challenging to manipulate dielectric particles smaller than 100 nm because the optical tweezers' trapping force is proportional to the third power of the particle's radius. Because important particles such as biological molecules, viruses, and nanoparticles have sizes ranging far below 50 nm, there has been an unmet need for a more powerful photonic technology. To address this issue, near-field optical manipulation methods have advanced significantly over the last few years [8-9]. The fundamental difference of the near-field optical tweezers over the conventional method is that the former utilizes the evanescently decaying light wave that is a part of optical modes excited in fabricated photonic structures (Fig 2.3.1). Compared to the light propagating in air whose optical index is 1, the light can be much more tightly confined in the photonic devices whose optical index is typically very high [10-12]. This tight confinement generates rapid decay of the intensity of the evanescent waves, which in turn generates large optical gradient forces to trap small particles. Among the many demonstrations of these near-field devices, one promising approach is to utilize well-established silicon waveguides because silicon waveguides have minimal absorption loss to the near-IR light, called an optical biological window due to small absorption in water, allowing us to confine and guide a huge amount of light energy. In 2009, Yang et al. utilized silicon waveguide structure to very tightly confine the powerful light energy and demonstrated manipulation of nanoparticles and relatively large DNA molecules that had diameters of > 100 nm [8]. Although it was a significant step, it is still challenging to achieve trapping of even smaller molecular because the index contrast of silicon with water is not large enough (i.e., tightness of the generated near-field energy was not enough). Alternatively, the field of plasmonic nano-tweezers has made rapid advances.

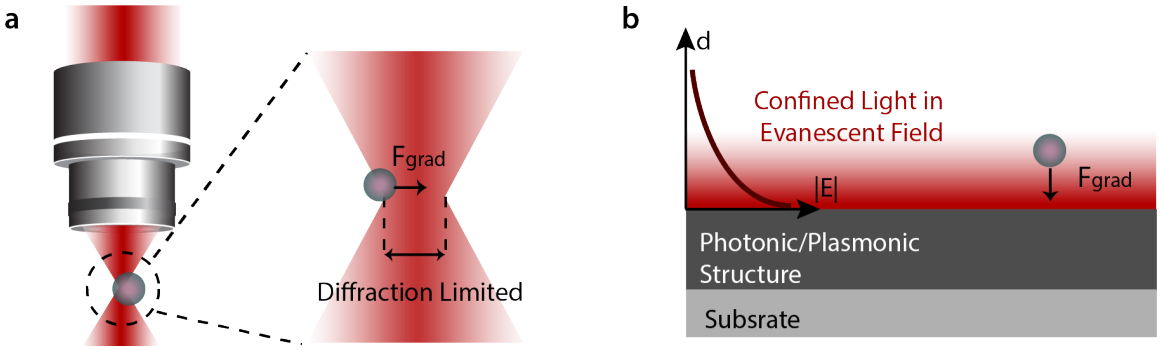

Figure 2.3.1 Examples of traditional and near-field optical tweezing/trapping techniques, showing relevant forces. (a) Traditional single-trap free-space optical tweezers. (b) Dielectric waveguide based on the near-field optical trap.

Plasmonic Nanotweezers

Plasmonic nanotweezers are nanofabricated metallic antenna structures that can store the light energy as localized surface plasmons (LSP), collective excitation of free electrons in metals excited by light [9, 13, 14]. The high index contrast of metals with the surrounding water results in the extreme energy confinement right down to deep sub-wavelength scales (Fig 2.3.2) [15, 16]. This enhanced EM energy in plasmonic antennas has enabled demonstration of trapping of Rayleigh dielectric particles and biological objects within the sub-wavelength volumes.

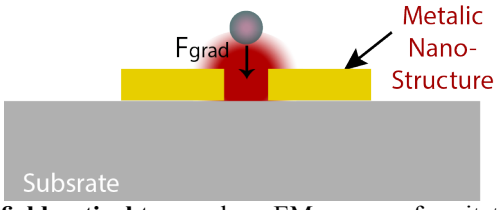

Figure 2.3.2 Plasmonic near-field optical trap, where EM energy of excitation light is enhanced to increase the trapping force, enabling Rayleigh dielectric particles and biological objects within the sub-wavelength volumes.

To date, these plasmonic antennas have been designed to produce the localized gradient forces for trapping the target particle at a single point fixed by the fabricated nanostructure [17-19]. On the other hand, transporting these targets over a long distance has never been shown. Although important especially for on-chip sorting, it is intrinsically difficult because the localized force is defined with pre-fabricated structures. While large scattering forces were alternatively utilized to show the control of metallic particles on a flat substrate [20, 21], the more powerful antenna-based tweezers have not been exploited for this purpose.

2.3.2 Brownian Ratchet

Particles in a liquid are subject to random collision of liquid molecules, displaying random behavior, so-called Brownian motion [22]. This thermal noise has usually been a critical problem in controlling particle flows at nanoscopic scales and has been suppressed for any method of particle manipulations. Contrary to general belief, the concept of Brownian ratchet is to take advantage of these Brownian fluctuations instead suppressing them. Indeed, the second law of thermodynamics states that the thermal energy originates no net motion of particles in the large scale. However, when driving anisotropic energetic systems out of thermodynamic equilibrium, it is possible to produce work out of the thermal noise. This is the working principle of the so-called Brownian ratchets [23, 24], first proposed by the Richard P. Feynman. After 40 year, this Brownian ratchet is still of fundamental interest in biology because such mechanisms play a role in biological protein motors [25], which utilizes the thermal fluctuation in its functional work. Devices utilizing this ratchet concept have also attracted significant interest as the basic working principle of future devices [26-31]. Moreover, mesoscopic Brownian motors, including organic electronic and spin ratchets, were experimentally demonstrated and showed its great potential as future powerful nanodevices and electronic circuits [32-36].

2.3.3 Plasmonic Brownian Ratchet

Here the idea of the plasmonic Brownian ratchet is to utilize the thermal ratchet mechanism to address the issue of unrevealed transporting of dielectric particles over long distances using the plasmonic antennas. This work presents a proof-of-principle demonstration of the optically excited nanoscale thermal ratchet based on LSP interactions. Essentially, it uses plasmonic-based near-field powerful optical forces, which first trap the sub-wavelength dielectric beads in the sub-wavelength fluid volume and then drive its long-distance displacement within a single device. The device consists of an array of plasmonic antennas with spatially broken symmetry, with which a set of anisotropic optical potential for trapping the beads is generated. By repeatedly the exciting and releasing process of the trapping potential, with a laser field turned on and off, the system is taken out of equilibrium, yielding a directed drift of particles in one direction. In addition, molecular dynamics (MD) simulations was utilized to demonstrate this mechanism, showing the rectified Brownian motion of the bead in the absence of any external far-field energy bias.

2.3.4. Plasmonic Antenna Design and Force Simulation

Plasmonic Antenna Design

The system uses an arrayed plasmonic nanostructure to rectify the Brownian motion of nanoscale dielectric beads of 50 nm diameter. The ratchet system design essentially requires two functions: (1) anisotropic trapping, generated by the antenna array's geometrical asymmetry and (2) temporally periodic modulation of the particle-plasmonic system interactions, achieved by turning the illumination on and off in periodic cycles (Fig 2.3.3a). To fulfill both required functions, the periodic array of the antenna structures is proposed as shown in Fig. 2.3.3b and Fig. 2.3.3c. The unit cell consists of four metallic dipole antennas (dielectric permittivity ε_m) with gradually changing lengths and with sub-wavelength spacing [37], where the dipole antenna is designed to have a deep sub-wavelength gap d and is separated from its nearest neighbor antenna by g. The dipole antennas are a pair of nanoscale rods with width w, height h, and varying lengths: L in one side of the group and $\mathrm{L_0} = \mathrm{L} - 3(\mathrm{w} + \mathrm{g})\tan\theta$ in another, where the angle θ represents the structure asymmetry. The array of nanostructures, with period Λ, is on top of a glass substrate and in water containing dielectric beads at room temperature. A normal incident plane wave (intensity $\mathrm{I_0}$) with the electric field polarized along the dipole antennas axis ($\mathrm{E_x}$) was chosen as illumination, efficiently exciting the near field within the gap and enabling trapping of the dielectric beads in the EM hotspots. In this way, a one-dimensional (1D) array of anisotropic plasmonic-based nano-optical traps was designed.

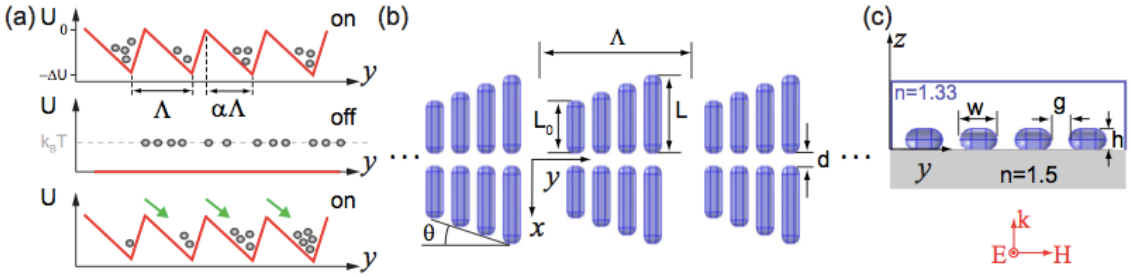

Fig 2.3.3 Schematic of plasmonic Brownian ratchet. (a) By periodically turning on and off continuous, periodic asymmetric potentials, the Brownian diffusion of a dielectric particle is biased in one direction. **(b)** The plasmonic system from a top view: a periodic array of plasmonic structures formed by four optical dipole antennas. The geometrical asymmetry is characterized by angle θ. **(c)** The periodic array unit cell from the side view: the plasmonic structure is placed on top of a glass substrate and embedded in water.

Force Simulation

The plasmonic nano-tweezers was characterized by considering a single array element, where the set of four dipole antennas composes one unit cell. In the presence of the plasmonic structure, the bead experiences optical forces determined by the system EM fields. Such fields are contained in the Maxwell stress tensor, $\overleftrightarrow{T}(r)$ [38], and are simulated based on the finite element method [39]. The integration of this tensor on an arbitrary surface enclosing the particle provides the force exerted on it:

$$F = \int \langle \overleftrightarrow{T}(r) \rangle \cdot n(r) da \qquad (2.3.1)$$

where n(r) is the normal unit vector to the integration surface. To obtain the force field [40], the tensor $\overleftrightarrow{T}(r)$ is calculated for variant positions of the particle's center. A line integration of the force from infinity to a position r provides the potential energy of the particle:

$$U(r) = \int_{-\infty}^{r} F(r') \cdot d(r') \qquad (2.3.2)$$

The calculated potential U(y) obtained for a PS bead (refractive index n = 1.59, radius = 50 nm) in the plasmonic structure of gold antennas for the different angle θ is shown in Fig. 2.3.4a. The particle-antenna separation was assumed to be 10 nm. The potential for driving the particle's motions along the group's symmetry axis (y direction, x = 0) was calculated and normalized to the thermal energy (k_BT) and the illumination intensity (I_0). The asymmetric geometry produces the anisotropy in the trap, and the simulated EM field for θ = 18 is shown in the inset panel of Fig. 2.3.4.b. The field pattern showed the significantly enhanced EM field in a hotspot located at the gap of the longest antenna. In the presence of the neighbor antennas, with slightly different resonance wavelengths due to their slightly different lengths, a continuous and asymmetric field profile along the y direction was produced. The asymmetry of the potential is characterized with its given parameter α, and its depth, U, which were depicted in Fig. 2.3.3. The upper (α) and lower (U) inset panels of 1.4.4a show the evolution of these two parameters with θ. The case θ = 0° is equivalent to a symmetric structure and consequently to a symmetric potential (α = 0.5). Increasing θ is equivalent to the more anisotropic potential (α decreases) by

moving the hottest spot to the longest antenna's gap and to increasing the depth of the potential well. For θ~18° [U(y) plotted as a yellow dashed line in panel (a)], α saturates at ~0.36: for larger θ, the dipole antennas are too different in length and are decoupled to distinct resonance frequencies. Fig. 2.3.4b shows the force field, yielding the potential for the coupled case in Fig. 2.3.4a. As the figure shows, F_y drives the particle to the hottest spot depicted in the inset. In the direction vertical to the substrate, F_z attracts the particle down to the antennas, while in the x direction $F_x \ll F_y$, F_z . The plasmonic structure with θ = 18 is convenient for designing the plasmonic ratchet due to the maximum anisotropy and potential depth, $\Delta U \sim k_B T I_0$ [mW^{-1} μm^2], given at the order of the thermal energy for illumination intensities $I_0 \sim 1$ mW/ μm^2.

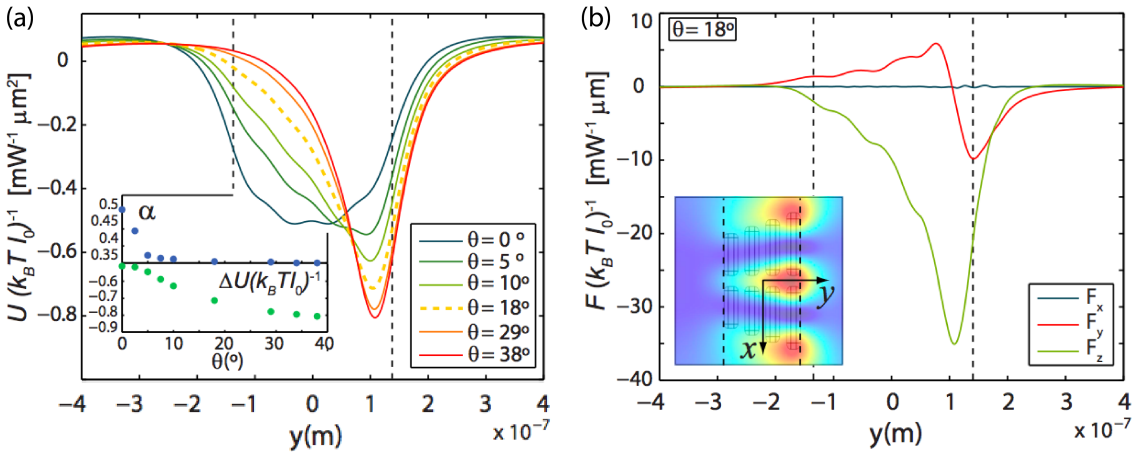

Fig. 2.3.4 (a) Trapping potential experienced by a dielectric bead near the plasmonic nanostructure (four dipole antennas). Several values of geometrical asymmetry are considered. Inset panels: the potential asymmetry parameter, α (upper) and the depth of the potential well, ΔU (lower) changes as a function of θ. The dashed vertical lines' point at the antenna's boundaries is shown for reference. **(b)** Forces experienced by the bead in the presence of a structure at θ = 18°. Inset panel: the normalized strength of the electric fields upon illumination at = 1.5μm is plotted at z = 90nm. The dipole antennas are designed to maximize the field enhancement at a near-IR excitation wavelength: geometrical parameters L = 225 nm, d = 40 nm, w = 50 nm, g = 25 nm, and h = 30 nm.

Now consider a periodic set of asymmetric plasmonic traps by arranging the plasmonic structures in a periodic manner (see Fig. 2.3.3). Fig. 2.3.5 is the optical potential calculated for the periodic array for different period Λ. This simulation assumed the plasmonic nanostructure subjected to periodic boundary conditions into the y direction. Assuming the plasmonic structures in such an array results in a coupling between them, generating a slightly oscillating potential depth with periods of Λ as shown in the figure inset. The maximum potential depth is at Λ ~ 1 μm, and its minimum at Λ ~ 1.4 μm. When the period becomes large enough, the depth approaches the value that corresponds to the single structure. The oscillation appears because of an interference effect in the far-fields between the plasmonic antennas.

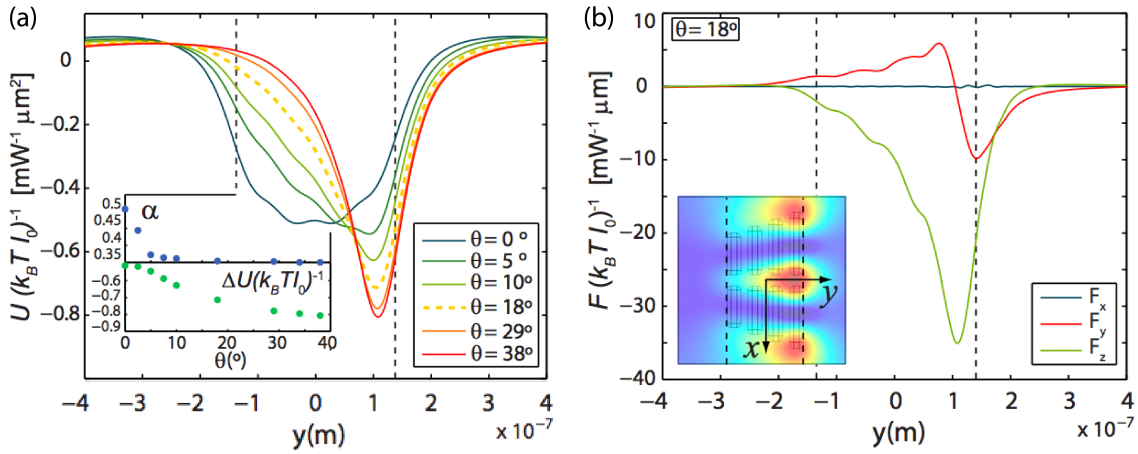

Fig. 2.3.5 Trapping a potential profile within a unit cell, generated by a periodic array of plasmonic structures θ = 18°. The anisotropic trapping potential is shown for different periods, Λ. Inset panel: evolution of the potential depth with a different array period.

2.3.5 Device Characterization

The Brownian ratchet operation is characterized using MD simulations. The following Langevin equation of motion (2.3.3) governs the Brownian dynamics of a dielectric particle with mass m and radius σ in water at a constant temperature T, which is subjected to the external plasmonic force F_y:

$$m\ddot{r} = F_y - \gamma m\dot{r} + \sqrt{2\gamma m k_B T}R(t) \qquad (2.3.3)$$

Here, the term $\gamma m\dot{r}$ represents the drag force exerted on the particles in water, where $\gamma = 6\pi\sigma\eta/m$. The last term is the Langevin expression explaining the Brownian motion due to a stochastic force, where R(t) is a delta-correlated Gaussian function with zero mean [41]. Ultimately, the particle dynamics is dominated by both the diffusivity, $D = k_B T/m$, and the external plasmonic forces.

Solution of Eq. (2.3.3) for *N* realizations of the system at T = 300 K simulates the statistics of the system. Here, a proof of concept ratchet design has the array period Λ = 800 nm, whose U(y) is plotted as a yellow line in Fig. 2.3.5 because it generates a potential without any local maxima. The dynamics are simulated in 1D and an irradiance $I_0 = 75$ mW/μm^2 is used to ensure stable trapping; the device also works for lower laser powers. The sample bead is initially placed within a unit cell ($0 \leq y \leq \Lambda$) of the anisotropic and periodic potential. An external laser excites the set of plasmonic traps during time t_{on}. There is no large-scale gradient force in the system and therefore no statistical net motion of the particle. With a long enough t_{on}, the bead is trapped at the potential minimum as $\Delta U \gg k_B T$. Fig. 2.3.6 shows a histogram of N realizations of the particle's position at $t = t_{on}$, displaying their distribution around the minimum. In the ratchet operation, the repeated modulation of the potential in time takes the system out of equilibrium. By turning off the potential, the particles freely diffuse out from the potential minimum. The spatial anisotropy makes the characteristic time, τ_F, needed for the particle to travel the distance $\alpha\Lambda$ to the neighbor unit cell in the forward direction, shorter than the characteristic time, τ_B, to travel backwards $(1-\alpha)\Lambda$. If $\tau_B \gg t_{off} \gg \tau_F$. The probability of the particle moving forward increases while that of moving backward

decreases. Thus, after one cycle, trapping the particle in the potential minimum in the forward direction is more likely than that in the backward direction. Repeating this cycle results in a rectified drift of the particles as an ensemble. Fig. 2.3.6b displays the particle's positions after 16 cycles, corresponding to t = 0.26 s, and shows the statistically directed motion in the forward direction. In the inset, the time evolution of the probabilities of moving forward and backward are shown as $P_F = N_F/N$ and $P_B = N_B/N$, where N_F and N_B are the number of realizations when the particle is at $y \gg \Lambda$ and $y \ll 0$. Together with P_F and P_B, P_0 is the probability of particles remaining in the initial cell. Circles are the probabilities after 4, 8, 12, and 16 on/off cycles, showing that P_F increases with the number of cycles, up to 40%, while P_B saturates around 10% with 4 cycles. The large number of repetitions results in clear observation of the increase in P_F and thus in the directed motion.

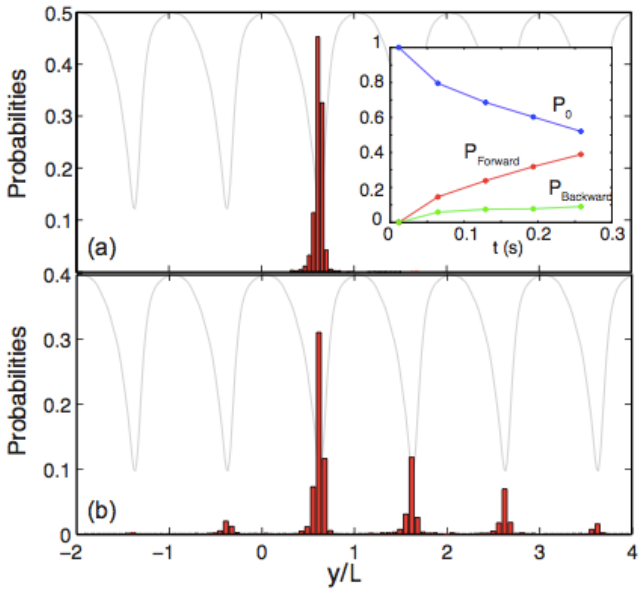

Figure 2.3.6 Plasmonic Brownian ratchet dynamics simulation for N = 4000 realizations of the system. One PS bead (radius = 50 nm, density ρ = 1050 kg/m^3) is embedded in water (viscous coefficient η = 1×10^{-3} kg/(m·s)) at room temperature and was exposed to the time-modulated plasmonic force potential. The dynamics is diffusive ($\gamma\tau_\sigma \sim 10^6$, where $\tau_\sigma = \sigma^2/D$ is time required for the bead to diffuse its own radius). **(a)** Initial situation: the particle probability distribution is centered at the trapping position of the nanotweezer ($0 \le y \le \Lambda$) after a time $t_{on} = 2\times10^4\tau_\sigma$, with $\tau_\sigma = \frac{\sqrt{m\sigma^2}}{k_BT} = 5.7\times10^{-7}$ s. Inset panel: time evolution of the probabilities for the particles to move forward (P_F), move backward (P_B), or to remain in the same cell (P_0). (b) Final situation: after 16 on-off cycles ($t_{off} = 8\times10^3\tau_\sigma$), the probability for the particle showing a directed motion in the forward direction is 40%. The gray line represents the plasmonic force potential in arbitrary units (U = 75kBT).

Finally, the practical implementation of the plasmonic ratchet must consider the thermal heat generation from the plasmonic antennas as the performance of the device can be affected by thermal-induced dynamics. Notoriously, light coupling to LSPs in metallic resonators causes heat dissipation into the surroundings [42]. It is feasible to minimize this heat effect in an experiment simply by reducing illumination intensities, or more carefully designing the plasmonic structure. For instance, a substrate with a high

thermal conductivity was utilized as a heat sink [43, 44]. Moreover, considering thin fluidic cells is also helpful to suppress the convection flow in the sample [45]. This last point also prevents beads from leaving the plasmonic structures in the vertical direction when the illumination is turned off.

2.3.6 Summary and Future Directions

The concept of a plasmonic Brownian ratchet device is proposed to enable transport of sub-wavelength dielectric particles in a plasmonic nano-tweezers system by taking advantage of thermal noise. This device requires only the temporally periodic modulation of the large EM field enhancement produced by the asymmetric plasmonic array structures under simple light illumination. The MD simulation demonstrated the statistical rectification of the Brownian motion of the nanoscale bead. The powerfulness of the plasmonic nanotweezers can overcome the limitations of conventional optical tweezers for manipulating particles, achieving control of the sub-wavelength particles' flow. This device can be applied to the wide range of micro- and nanofluidics applications where colloidal and biological objects' manipulation is desired.

One of the critical limitations of the current idea is the lack of spatial confinement of the Brownian particles along the gaps of the dipole antennas. Future experimental demonstration can circumvent this issue by combining the antenna arrays with a nanofluidic channel. Although the alignment of the nanoscale structures is challenging, a possible design that does not require the alignment between the prefabricated nanochannel and the patterned antenna is displayed here (Fig. 2.3.7). PR representing the photoresist can be patterned using e-beam lithography, achieving good alignment with the metallic antennas relatively easily. Then, while heating up the sample to melt and reflowing the PR, another substrate is placed on it to seal it and create a nanofluidic channel over the antenna space. Alumina is recommended for this because it has higher thermal conductivity than glass, which can act as a heat sink to minimize the heat issue.

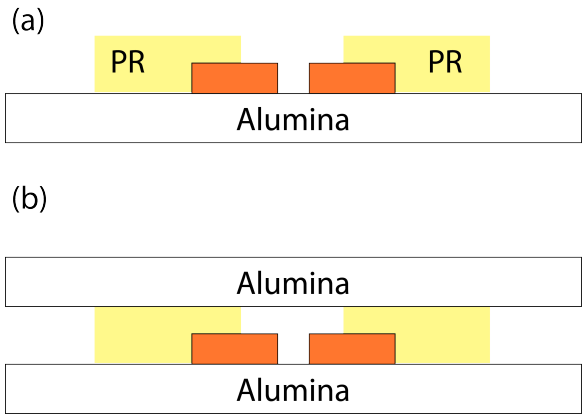

Fig. 2.3.7 Possible fabrication design for experimental realization of plasmonic Brownian Ratchet. The device has a nanofluidic channel that encloses the antenna array. **(a)** To make the alignment between the channel and antennas feasible, photoresist that simultaneously acts as a nanoscale spacer and the adhesive glue is patterned by e-beam lithography with nanometer-order computer-controlled alignment with the bottom nanoantenna structures. **(b)** The top sealing substrate is placed on the photoresist and, by heating the device to remelt the photoresist, the channel structure is irreversibly enclosed. Alumina substrate is suggested because it has higher heat conductivity than glass, thus acting as a heat sink to prevent the unfavorable heat effects inside the nanochannel.

References

1. Erickson, D., Serey, X., Chen, Y.-F. & Mandal, S. Nanomanipulation using near field photonics. *Lab Chip* **11,** 995 (2011).
2. Weiss, S. Fluorescence Spectroscopy of Single Biomolecules. *Science* **283,** 1676–1683 (1999).
3. Moffitt, J. R., Chemla, Y. R., Smith, S. B. & Bustamante, C. Recent Advances in Optical Tweezers. *Annu. Rev. Biochem.* **77,** 205–228 (2008).
4. Fazal, F. M. & Block, S. M. Optical tweezers study life under tension. *Nature Photonics* **5,** 318–321 (2011).
5. Brunner, M. & Bechinger, C. Phase Behavior of Colloidal Molecular Crystals on Triangular Light Lattices. *Phys. Rev. Lett.* **88,** 248302 (2002).
6. Mikhael, J., Roth, J., Helden, L. & Bechinger, C. Archimedean-like tiling on decagonal quasicrystalline surfaces. *Nature* **454,** 501–504 (2008).
7. Chowdhury, A., Ackerson, B. J. & Clark, N. A. Laser-induced freezing. *Phys. Rev. Lett.* **55,** 833–836 (2011).
8. Yang, A. H. J. *et al.* Optical manipulation of nanoparticles and biomolecules in sub-wavelength slot waveguides. *Nature* **457,** 71–75 (2008).
9. Juan, M. L., Righini, M. & Quidant, R. Plasmon nano-optical tweezers. *Nature Photonics* **5,** 349–356 (2011).
10. Ashkin, A. Acceleration and trapping of particles by radiation pressure. *Phys. Rev. Lett.* **24,** 156–159 (1970).
11. Ashkin, A., Dziedzic, J. M., Bjorkholm, J. E. & Chu, S. Observation of a single-beam gradient force optical trap for dielectric particles. *Optics letters* **11,** 288–290 (1986).
12. Ashkin, A. Forces of a single-beam gradient laser trap on a dielectric sphere in the ray optics regime. *Biophysj* **61,** 569–582 (1992).
13. Novotny, L., Bian, R. & Xie, X. Theory of Nanometric Optical Tweezers. *Phys. Rev. Lett.* **79,** 645–648 (1997).
14. Arias-González, J., Nieto-Vesperinas, M. & Lester, M. Modeling photonic force microscopy with metallic particles under plasmon eigenmode excitation. *Phys. Rev. B* **65,** 115402 (2002).
15. Barnes, W. L., Dereux, A. & Ebbesen, T. W. Surface plasmon subwavelength optics. *Nature* **424,** 824–830 (2003).
16. S. A. Maier, Plasmonics: Fundamentals and Applications, *Springer*, New York, (2007).
17. Righini, M., Volpe, G., Girard, C., Petrov, D. & Quidant, R. Surface Plasmon Optical Tweezers: Tunable Optical Manipulation in the Femtonewton Range. *Phys. Rev. Lett.* **100,** 186804 (2008).
18. Grigorenko, A. N., Roberts, N. W., Dickinson, M. R. & Zhang, Y. Nanometric optical tweezers based on nanostructured substrates. *Nature Photonics* **2,** 365–370 (2008).
19. Righini, M. *et al.* Nano-optical trapping of Rayleigh particles and Escherichia coli bacteria with resonant optical antennas. *Nano Lett.* **9,** 3387–3391 (2009).
20. Wang, K., Schonbrun, E. & Crozier, K. B. Propulsion of Gold Nanoparticles with Surface Plasmon Polaritons: Evidence of Enhanced Optical Force from Near-

Field Coupling between Gold Particle and Gold Film. *Nano Lett.* **9,** 2623–2629 (2009).
21. Cuche, A. *et al.* Brownian motion in a designer force field: dynamical effects of negative refraction on nanoparticles. *Nano Lett.* **12,** 4329–4332 (2012).
22. Einstein, A. On the movement of small particles suspended in stationary liquids required by the molecular-kinetic theory of heat. *Ann Physic* (1905).
23. R. P. Feynmann, R. B. Leighton, and M. Sands, Feyn- mann Lectures in Physics (Addison-wesley, Reading, 1966).
24. Hänggi, P. Artificial Brownian motors: Controlling transport on the nanoscale. *Rev. Mod. Phys.* **81,** 387–442 (2009).
25. Terada, T. P., Kimura, T. & Sasai, M. Entropic Mechanism of Allosteric Communication in Conformational Transitions of Dihydrofolate Reductase. *J. Phys. Chem. B* **117,** 12864–12877 (2013).
26. Faucheux, L., Bourdieu, L., Kaplan, P. & Libchaber, A. Optical thermal ratchet. *Phys. Rev. Lett.* **74,** 1504–1507 (1995).
27. Astumian, R. D. Thermodynamics and kinetics of a Brownian motor. *Science* **276,** 917–922 (1997).
28. Bader, J. S. *et al.* DNA transport by a micromachined Brownian ratchet device. *Proc. Natl. Acad. Sci. U.S.A.* **96,** 13165–13169 (1999).
29. van Oudenaarden, A. & Boxer, S. G. Brownian ratchets: molecular separations in lipid bilayers supported on patterned arrays. *Science* **285,** 1046–1048 (1999).
30. Zapata, I., Albaladejo, S., Parrondo, J. M. R., Sáenz, J. J. & Sols, F. Deterministic ratchet from stationary light fields. *Phys. Rev. Lett.* **103,** 130601 (2009).
31. Di Leonardo, R. *et al.* Bacterial Ratchet Motors. *PNAS* 9541–9545 (2009).
32. Song, A. *et al.* Nonlinear Electron Transport in an Asymmetric Microjunction: A Ballistic Rectifier. *Phys. Rev. Lett.* **80,** 3831–3834 (1998).
33. Linke, H. Experimental Tunneling Ratchets. *Science* **286,** 2314–2317 (1999).
34. Villegas, J. E. *et al.* A superconducting reversible rectifier that controls the motion of magnetic flux quanta. *Science* **302,** 1188–1191 (2003).
35. Hüttel, A., Ludwig, S., Lorenz, H., Eberl, K. & Kotthaus, J. Direct control of the tunnel splitting in a one-electron double quantum dot. *Phys. Rev. B* **72,** 081310 (2005).
36. Costache, M. V. & Valenzuela, S. O. Experimental Spin Ratchet. *Science* **330,** 1645–1648 (2010).
37. Zhang, S. *et al.* Anti-Hermitian plasmon coupling of an array of gold thin-film antennas for controlling light at the nanoscale. *Phys. Rev. Lett.* **109,** 193902 (2012).
38. H. Novotny, Lukas, Principles of Nanooptics*, Cambridge University Press*, (2006).
39. COMSOL, Multiphysics 4.2a.
40. McCauley, A. P. *et al.* Microstructure effects for Casimir forces in chiral metamaterials. *Phys. Rev. B* **82,** 165108 (2010).
41. P. Langevin, On the Theory of Brownian Motion", *C. R. Acad. Sci. (Paris)* **146**, 530-533 (**1908**)
42. Baffou, G. & Quidant, R. Thermo-plasmonics: using metallic nanostructures as nano-sources of heat. *Laser & Photon. Rev.* **7,** 171–187 (2012).

43. Wang, K., Schonbrun, E., Steinvurzel, P. & Crozier, K. B. Trapping and rotating nanoparticles using a plasmonic nano-tweezer with an integrated heat sink. *Nature Communications* **2,** 469–474 (2011).
44. Wong, H. M. K. *et al.* On-a-chip surface plasmon tweezers. *Appl. Phys. Lett.* **99,** 061107–061107–3 (2011).

Chapter 3

Plasmon Nanolaser-based Ultra-Sensitive Gas Sensor

3.1 Hurdles to Overcome for Enhancing Gas-Phase Sensitivity

There is a critical demand for the ultra-sensitive detection of vapor-phase chemicals or biological molecules in improving national security, health care, and environmental protection for the future sustainable society [1-5]. Despite the great advancements and sophistications in the recent optical technologies, discussed in the introduction chapter (Section 1.2), the direct detection of explosive molecules such as TNT and DNT at the sub-ppb level is still challenging. Among the series of approaches toward optical gas sensing in Section 1.2, the photonic/plasmonic devices and fluorescent organic materials have potential in terms of practicality and ease of quantification of detections. So, here I briefly restate the basics and issues of these sensors to clarify my goal: plasmon laser-based gas sensing.

Both of the introduced dielectric and plasmonic devices are essentially resonant structures that localize electric fields of light and enhance the light-matter interactions [6-8]. Their resonant behavior is utilized because the absorption of molecules changes the refractive index of the surroundings as well as the peak/dip wavelength of the resonators. In general, the sensitivity of these resonant sensors increases by increasing two essential factors: (1) quality factor of the cavity, Q, and (2) surface-to-volume, S/V, ratio of the optical structure. Currently, surface plasmon (SP) sensors are passively excited (designed only with pure metals) and can achieve limited Q due to the intrinsic Ohmic loss in metals [4, 8-20]. On the other hand, the dielectric-based photonic structures such as ring resonators have limited surface-to-volume ratio due to the diffraction of light [21, 22]. Thus, it is difficult to achieve both factors at the same time. Consequently, the existing sensors are not sensitive enough to reliably respond to the minute refractive index change due to the surface adsorption of small gas molecules.

Fluorescent semiconductor materials are currently some of the most promising platforms, where surface-binding events can induce changes in their optical properties [23-28]. These materials are ready for use simply after being coated on plain substrates or dielectric photonic structures such as Bragg-grating resonators. The non-limit in size, the intrinsic high porosity of organic polymers, and their cheapness makes this approach attractive to practical applications. Its weakness is that organic dye-based devices suffer from photobleaching [24-27]. This issue is especially severe in its sensor applications wherein the sensing media is typically exposed to oxidative environments, such as ambient air that contains oxygen, water, explosives, and other gases [1, 24-31]. The weaker photo-stability of organic materials over the inorganic ones is always the case for other examples such as the dye lasers over inorganic ones, as well as organic dyes over quantum dots. In fact, the significant enhancement in the gas-phase explosive detection was experimentally observed when the fluorescent polymer was excited strongly up to lasing. The quick photobleaching, however, made it unpractical for real applications. In addition, its sensitivity enhancement was limited because the polymer was coated on a diffraction-limited dielectric photonic device [1].

3.2 Plasmon Laser-based Sensing

It is difficult to achieve the high Q and S/V ratio simultaneously in optical gas sensor photonic/plasmonic devices. It is, however, possible via a union of semiconductors with plasmonic resonant structures (cavities). SP modes provide deep sub-wavelength confinement, and the semiconductor provides optical gain for compensating the ohmic losses in metal. Recently demonstrated plasmon lasers exhibited well-confined strong local electric fields, increased radiating power, and dramatically narrowed line width, compared to the passive plasmon resonators [32-39]. Such a highly emissive cavity has been theoretically predicted for significantly improving sensitivity to changes in the local environment [40-42].

Here, my idea is to utilize actively excited plasmon cavities for gas sensing. The active plasmon nanocavity sensor (APS) device is based on a lasing plasmon nano-cavity wherein a single crystalline cadmium sulfide (CdS) nano-slab simultaneously acts as optical gain and as sensing material (Fig. 3.1). Loss of compensation by gain allows the sub-diffractive cavity to achieve an intense and sharp lasing emission. The surface-adsorption of the molecules on the gain semiconductor significantly modulates the lasing intensity. Benefitting from both the good photo-stability of the crystalline inorganic gain and enhanced light-matter interaction associated with plasmon lasing, the APS achieved sub-ppb level detection of multiple explosive molecules with selectivity attributed to their electron deficiency. Furthermore, there was 300-fold sensitivity enhancement under the lasing condition over the spontaneous emission condition.

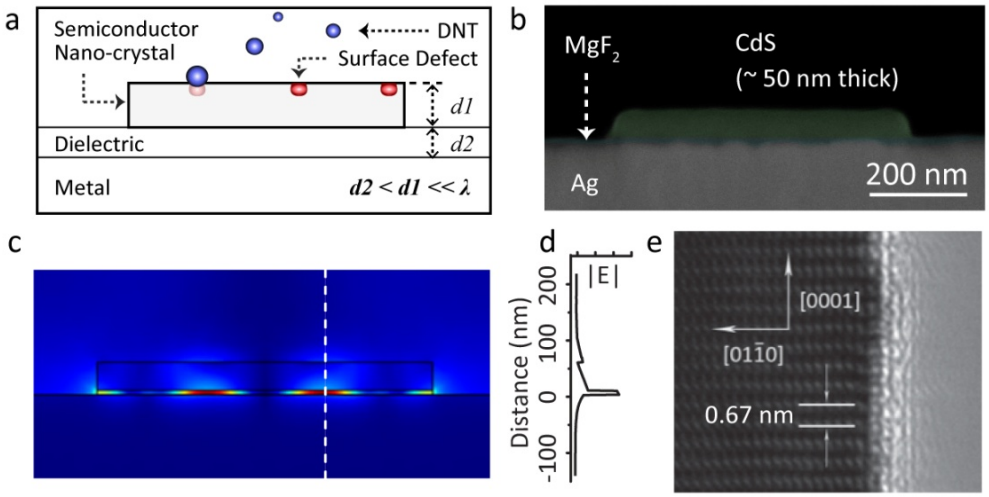

Figure 3.1 Schematic, SEM image, simulation of electric field distribution, and TEM image of an active plasmon nanocavity gas sensor. (**a)** The sensing scheme is based on the intensity modulation of stimulated emission from a lasing plasmon nano-cavity with sub-wavelength electromagnetic field confinement. In the cavity, the semiconductor slab acts as optical gain and as sensing material simultaneously. The large surface-to–physical volume ratio (S/V_{phy}) of the nano-cavity enhances the intensity modulation effect associated with surface events. This is because the number of carriers that can be influenced by surface events is highly limited due to the small V_{phy}, while there is a large surface area for analyte absorption. (**b)** SEM image of the device shows a CdS nano-slab with thickness of 50 nm and length of 600 nm atop silver film, with separation of 8 nm and low permittivity in the MgF_2 layer. (**c)** Electric field distribution in a cross-section of the nano-cavity EM mode that was simulated in 3D space. (**d)** Distribution of electric field amplitude |E| along the dashed line in (**c**). (**e)** high resolution TEM image of a top view of CdS slab shows the single crystal structure and atomically smooth surface, crucial for the optical performance of the device.

3.3 Plasmon Laser Design

Fig. 3.1a and Fig. 3.1b show a schematic and a SEM image of the active plasmon sensor, respectively. The device consists of a single crystalline semiconductor CdS nano-slab (50 nm in thickness, 600 nm in length) on top of a silver surface separated by an 8-nm-thick magnesium fluoride (MgF_2) gap layer. The CdS nano-slabs were synthesized with a chemical vapor deposition (CVD) method. CdS (99.995%) powders were used as the source, and pieces of Si wafers covered with 10 nm of thermally evaporated gold catalysts were used as the substrates. The grown CdS nano-slabs show a single crystalline lattice structure with a lattice spacing of a_{CdS} = 0.67 nm along the [0001] axis corresponding to a wurzite crystal lattice (Fig. 3.1b). The silver/magnesium fluoride substrates were deposited by electron beam evaporation on a silicon wafer. The film roughness (RMS) measured by AFM was below 1 nm. CdS nano-slabs were deposited from the solution by spin coating onto silver/magnesium fluoride substrates.

The SP mode localizes the electromagnetic field at the interface between the metal and semiconductor, allowing both the device's physical size and mode confinement to shrink down to the nanometer scale in a dimension perpendicular to the metal surface (Fig 3.1c–3.1d). The optical modes were calculated using a finite-element method 3D eigen-mode solver with Comsol Multiphysics. In this model, the CdS nano-slab ($n_{CdS} = 2.5$) was laid in contact with an 8-nm MgF_2 ($n_{MgF2} = 1.38$) gap layer above a single Ag strip ($\varepsilon_{Ag} = \varepsilon_b - E_p^2[E(E - i\gamma)]^{-1}$, $\varepsilon_b = 5$ eV, $\gamma = 0.04$ eV). The effective mode volume of the lasing plasmon cavity was calculated as $V_{eff} = \int w_{em}(\vec{r})d^3\vec{r}/\varepsilon_0\varepsilon(|\vec{E}|^2{}_{max})$, where w_{em} was the electromagnetic energy density of the optical mode. $\vec{E}$ in the denominator was the evaluated maximal electric field. Taking into account the strongly dispersive property of silver, $w_{em}(\vec{r})$ equals half of $[\mathrm{Re}\left[\frac{d(\omega\varepsilon)}{d\omega}\right]|\vec{E}(\vec{r})|^2 + \mu|\vec{H}(\vec{r})|^2]$. As a result, the calculated optical mode volume is only about 0.03 λ^3. The Q factors of the cavity modes were calculated with the formula $Q = f_r/\Delta f$, where the f_r is the resonance frequency and Δf is the full width at half maximum of the resonance spectrum. For the Q factors of the cavity modes with gain, a complex refractive index of $n_{CdS} = n - i\kappa$ was fixed, where the gain coefficient κ can vary depending on the pump intensity. The Q factor is significantly enhanced by orders of magnitude with the increase of gain coefficient κ and reaches maximum at a κ value of 0.19, corresponding to a material gain ($g = 4\pi\kappa/\lambda$) of ~9500 cm^{-1}.

The semiconductor slab with an atomically smooth surface displayed in Fig. 3.1e simultaneously serves as the optical gain and nanoscale sensing medium in the lasing plasmon nano-cavity. The large surface-to–physical volume ratio (S/V_{phy}) of the nano-cavity, which is inversely proportional to the nano-slab thickness, strengthens the surface modulation effect to the emission. While the large surface area S allows more analytes' adsorption, the small physical volume V_{phy} limits the number of carriers to be influenced inside. In our cavity, S/V_{phy} can also be expressed as $\frac{S \cdot n_e}{N}$, where $V_{phy} = \frac{N}{n_e}$, n_e is the carrier concentration and N is the carrier number in the cavity. The carrier density just above the lasing threshold of the plasmon nano-slab cavity is on the order of 10^{18} cm^{-3}. Given that the V_{phy} of the CdS nano-slab is about 0.018 μm^3 (~0.14 λ^3), the number of carriers for the lasing operation *N* in the device is ~1.8×10^4, making the emission intensity intrinsically sensitive to the few number of surface events.

3.4 Experimental Setup

The characterization of the device sensitivity was performed in a sealed chamber with two ports for gas exchange and an optical window for both the pumping and signal collection, respectively (Fig. 3.2a). The device was exposed to a flow of diluted target gas molecules at a controlled concentration. Inert N_2 gas was used to dilute explosive vapors while also serving as the background reference. The saturated explosive vapor in N_2 can be further diluted by another N_2 channel, and thus its final concentration can be determined by the ratio of the flow rates in these two channels. The sensing devices were optically pumped by a frequency-doubled, mode-locked Ti-sapphire laser (Spectra Physics) with λ_{pump}=405 nm, a 10 KHz repetition rate and approximately 100 fs pulse length. A 20x objective lens (NA=0.4) was used to focus the pump beam to around the 2-μm diameter spot onto the sample and collect its luminescence efficiently. The device was optically pumped above the lasing threshold at room temperature.

Fig. 3.2b shows the dependence between the pump intensity and emission intensity and line width of the device emission. The lasing emission above the threshold has a much narrower line width, stronger intensity, and higher slope efficiency than those of spontaneous emission. These features provide the device with high performance in terms of high signal intensity (I) and relative intensity change (ΔI/I) at peak wavelength.

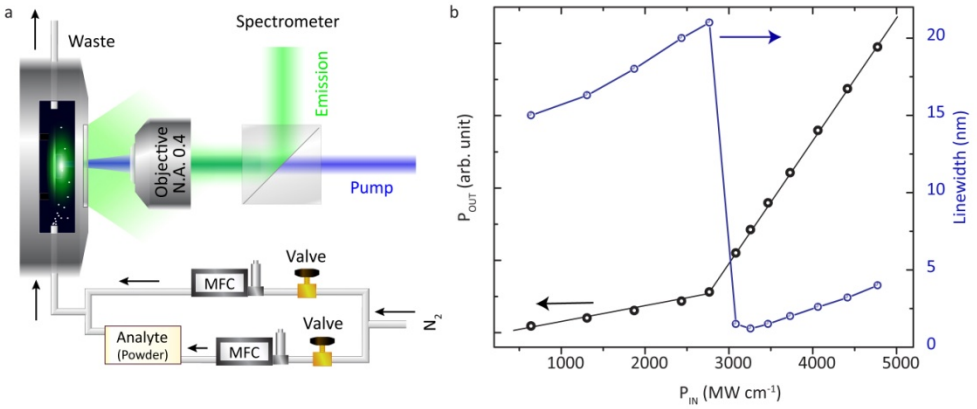

Figure 3.2 Characterization of the active plasmon nanocavity laser. (**a)** Experimental setup. The device was placed in a sealed chamber with two ports for gas exchange and an optical window for both optical pumping and signal collection. A spectrometer continuously tracked the laser emissions from the device at a controlled concentration of gas vapors. (**b)** Pump intensity dependence of the total emission intensity and line width of the device. The stimulated emission above the lasing threshold provides stronger intensity, higher slope efficiency and much narrower line width than these of spontaneous emission. These features enable the device's higher performance in terms of high signal-to-noise ratio and relative intensity change (ΔI/I) at peak wavelength.

3.5a Time-Lapsed Spectroscopy for APS-based DNT Detection and Its Stability Test in Air

DNT with a saturation concentration of about 100 ppb at room temperature was chosen as the target chemical [1]. In our sensing scheme, the peak intensity change of the lasing emission reflects the detection of molecules adsorbing onto the lasing cavity. In Fig. 3.3**a**, the lasing emission spectrum under a flow of 8 p.p.b, is shown. The emission in the DNT is compared with that in pure N_2. The surface adsorption of DNT induces an apparent increase in the peak intensity at about 505 nm, while no appreciable change in

the peak wavelength is observed. Fig. 3.2d displays the evolution of the peak intensity at 505 nm as the flow alternates between pure N_2 and diluted DNT at various concentrations. An increase in the peak intensity and further saturation within several minutes after switching on a flow of the diluted DNT was observed. Fig. 3.2d show that, even at the level of 1 ppb, 6 % of $\Delta I/I$ could be detected. The peak intensity decreased to the original value after switching back to a pure-N_2 flow, showing the reversible response. The response time of sensing reflects a slow change of the local DNT concentration on the device surface. This transient time of several minutes is not limited by the device itself but is mainly determined by the flow rate and the volume of the chamber. Moreover, when tracking the lasing peak wavelength via Gaussian fitting of the spectra, there is no appreciable change in the peak wavelength at various DNT concentrations (Fig. 3.3b blue dots). This observation indicates that, in the case of active plasmon sensors, direct monitoring of the lasing intensity has superior performance compared to that of the index change–induced peak wavelength shift.

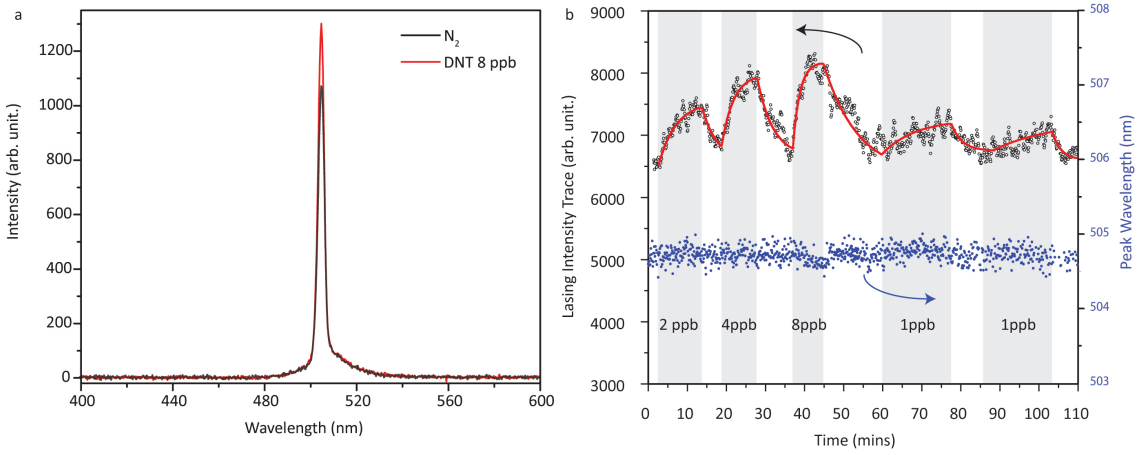

Figure 3.3 APS-based gas sensing. **(a)** Measured emission spectra of the lasing plasmon cavity in pure N_2 (black curve) and 8 ppb DNT (red curve). An obvious increase of lasing intensity in a flow of 8 ppb DNT is observed. **(b)** Black circles: Continuous trace of emission intensities of the APS when delivering DNT vapors at varied concentrations of 1, 2, 4, and 8 ppb. The lasing intensities showed apparent increase after each DNT delivery, even at the level of 1 ppb, with a change of 6 %. When the input gas was switched to pure N_2, the lasing intensities decreased to the initial value. Blue dots: The lasing peak wavelength tracked via Gaussian fitting of the spectra. There is no appreciable change in the peak wavelength at a variety of DNT concentrations, which indicates that directly monitoring the lasing intensity has superior performance over monitoring the index change–induced peak wavelength shift in active plasmon sensors.

Although the detection of DNT in N_2 demonstrated the principle of our sensor devices, the path toward a practical sensor requires measuring the target molecules in air and in the presence of common interferences. To achieve this, standard air and N_2 were alternatively delivered into the chamber. The lasing intensities showed increase of only about 1% after each air delivery, with a decrease to the original value after switching back to pure N_2 (Fig. 3.4). When it was kept lasing in air, the emission showed *no* appreciable photobleaching over 1800 seconds, as shown in Fig. 3.5. This high stability is because of the use of the inorganic crystalline semiconductor slab in our device. In contrast, the organic polymer-based devices generally suffer from significant photobleaching in a short time [1, 24-31]. In practical application, the use of stable

inorganic materials is beneficial for a reliable signal readout and for a long lifetime. These experiments confirmed that the device can be operated in air with very high stability, and explosives can be detected if they cause significant change in the lasing emission.

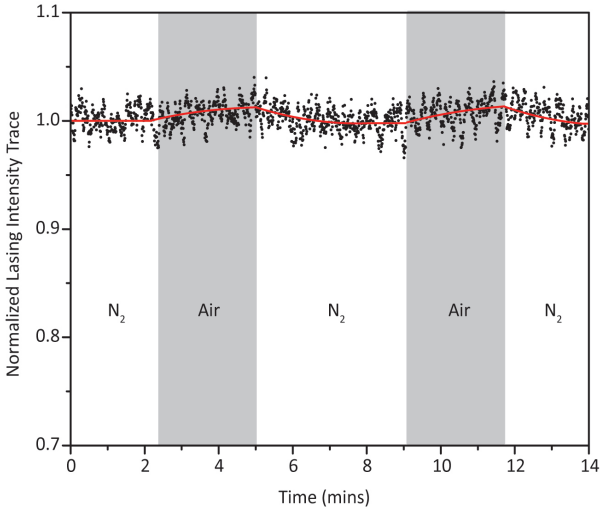

Fig. 3.4 Continuous trace of emission intensities of the active plasmon nano-sensor when air and N2 were alternately delivered into the chamber. The lasing intensities showed an increase of ~1% after each air delivery. When the input gas is switched to N_2, the lasing intensities decreased to the initial value.

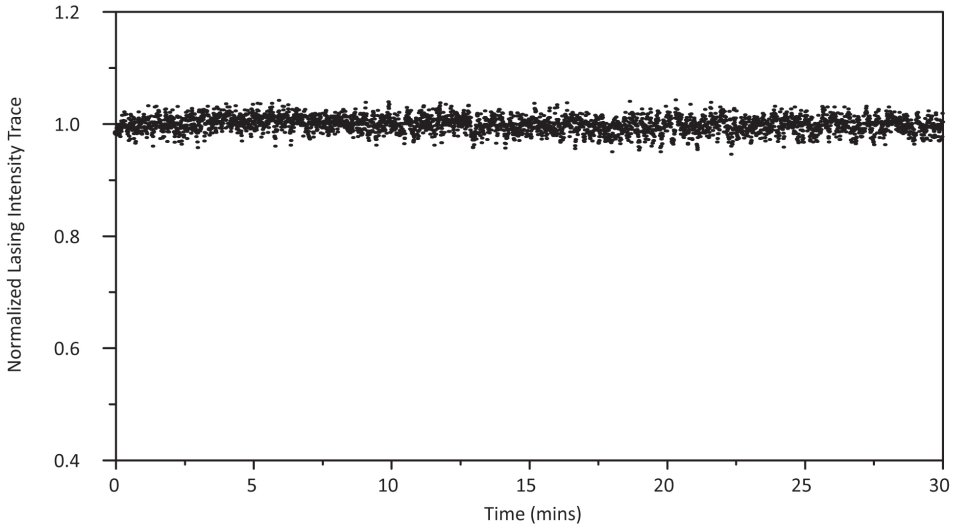

Fig. 3.5. Continuous tracing of lasing emission intensities of the active plasmon sensor in air. There is no appreciable photobleaching in over 1800 seconds; conversely, the organic polymer laser sensor demonstrated by others suffered more than 3% of photobleaching in just over 20 seconds [5, 15–17].

3.5b Selective and Sensitive Gas Sensing

The path toward a real explosives detector also requires that the detectors for selectivity be at high sensitivity. To show this capability, I detected four different explosive molecules: DNT, ammonium nitrate (AN), nitrobenzene (NB), and nitrotoluene (NT). The detection was quantified to characterize our device's sensitivity as well as

selectivity. In the experiment, air was used to dilute the explosive vapors and as the background reference. Figs. 3.6a–d show the continuous trace of emission intensities of the lasing plasmon nano cavity when AN (**a**), DNT (**b**), NB (**c**), and NT (**d**) vapors are delivered at varied concentrations by diluting them in air. The lasing intensities apparently increased after each analyte delivery and decreased to the initial value after switching the input gas to only air. As shown in all figures, despite the detection in air, the sensor showed highly robust and reversible responses. From the sensor response acquired in Figs. 3.6a-d, the calibration curves for these four analytes are obtained as shown in Fig. 3.6e, where the lasing intensity changes percentages ($\Delta I/I$) are plotted as a function of the analytes' vapor concentration. The sensitivities defined as the slope of the calibration curves for DNT, AN, NB, and NT are 1.2%/ppb, 6.1%/ppb, 0.4%/ppm, and 0.3%/ppm, respectively [43]. The limits of detection of these analytes in air can also be obtained from the calibration curves. The minimum distinguishable analytical signal, S_{lod}, is taken as a+3S, where a and S are y-intercept and standard deviation of the regression of the calibration curves, respectively. The limits of detection obtained for DNT, AN, NB, and NT are 0.67 ppb, 0.4 ppb, 7.2 ppm and 2.7 ppm, respectively. Thus, I have demonstrated that our sensor responds to the different analytes in air with good robustness, reversibility, and stability over the long-lasting experiments (> 5 hours).

Furthermore, the selectivity of our device was quantitatively characterized, where the selectivity coefficient for A with respect to B is defined as $k_{B,A} = m_B/m_A$ [10], and where m_B and m_A are the calibration sensitivity of the analytes A and B. From the measurement and analysis we made above, the $k_{B,A}$ of DNT with respect to AN, NB, and NT are 5.1, 3.3×10^{-4}, and 2.5×10^{-4}, respectively. The selectivity of our sensor is attributed to the different electron deficiencies of the four gases [44-46]. The materials tested in the experiments have specific electron deficiencies, which originate from their oxidative nitro groups. The AN decomposes to nitric acid, a stronger oxidizer than the DNT, which is a nitro derivative of toluene. The DNT with two nitro groups is more electron-deficient than the NB and NT with a single nitro group. When the explosives are ordered according to electron deficiency, AN > DNT > NB, NT, the results correspond with the magnitude of induced responses to our sensor.

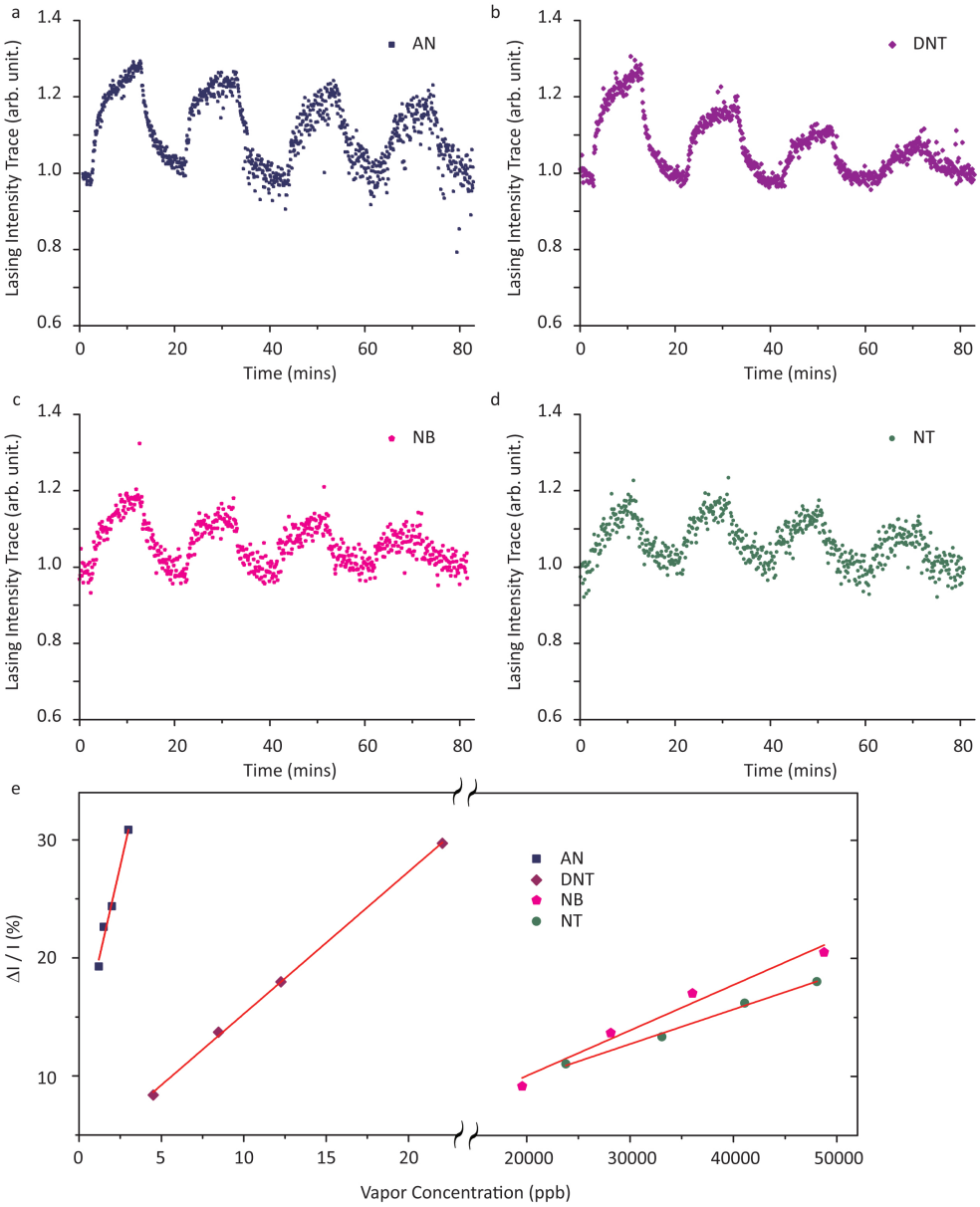

Figure 3.6 Detection of 2, 4-dinitrotoluene (DNT), ammonium nitrate (AN), nitrobenzene (NB), and nitrotoluene (NT) in air. (a-d) Continuous traces of lasing intensities at varied AN (**a**), DNT (**b**), NB (**c**), and NT (**d**) vapor concentrations diluted by air. **(e)** Calibration curves for these four analytes. The sensitivities defined as the slope of the calibration curves for DNT, AN, NB, and NT are 1.2%/ppb, 6.1%/ppb, 0.4%/ppm, and 0.3%/ppm, respectively. The detection limits obtained for DNT, AN, NB and NT are 0.67 ppb, 0.4 ppb, 7.2 ppm and 2.7 ppm, respectively. The selectivity coefficients of DNT with respect to AN, NB, and NT are 5.1, 3.3×10^{-4}, and 2.5×10^{-4}, respectively. The device holds selectivity due to specific electron deficiency of target explosive molecules because our sensing is based on the surface recombination velocity modification, which is sensitive to the electron deficiency of adsorbed molecules.

3.5c Sensitivity Enhancement in Lasing Condition

The sensitivity of our sensor in the lasing condition is significantly enhanced compared to that in the spontaneous emission condition. Fig. 3.7a shows the continuous trace of spontaneous emission intensities when DNT delivered vapors at different concentrations. Fig. 3.7b shows the calibration curves obtained for DNT detection in the

spontaneous emission condition. The sensitivity and the detection limit were obtained at 0.23 %/ppb and 14 ppb respectively. The sensitivity of lasing emission was ~5 times higher than that of spontaneous emission, and the detection limit was ~21 times better. We note that the peak intensity of the lasing emission was about 60 times higher than that of the spontaneous emission (Fig. 3.7c**)**. So the sensitivity of lasing emission was ~300 times higher than that of spontaneous emission when ΔI is directly used as the measure of signal [1, 27].

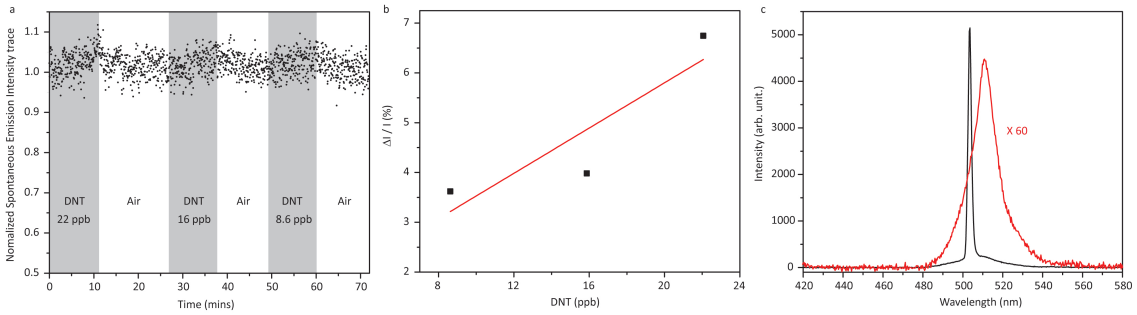

Figure 3.7 Detection of explosive molecules by the same cavity via spontaneous emission. (a) Continuous trace of spontaneous emission intensities at different DNT vapor concentrations diluted by air. **(b)** Calibration curves obtained for DNT detection via spontaneous emission. The sensitivity and the detection limit were obtained at ~0.23 %/ppb and ~14 ppb, respectively. The lasing emission sensitivity showed at about 5 times higher than spontaneous emission sensitivity, and the limit of detection was about 21 times better. **(c)** Spontaneous emission and lasing emission of the sensor device. When ΔI was used as a direct measure of the signal, the sensitivity of lasing emission was revealed at ~300 times higher than that of spontaneous emission.

3.5d Mechanisms Discussion

To understand the underlying mechanism of the sensing process, I performed a measurement of time-resolved spontaneous emission of the cavity (Fig. 3.8). For the intensity modification, I propose two possible physical processes [23]. The first scenario is that the adsorbed DNT molecules on the device modify the localized charge layer at the surface, generating an electrostatic field in the near-surface region within the semiconductor. The second one is that the DNT molecules influence the rate of surface recombination through interactions with surface states of the gain material. The former process increases the emission intensity by mitigating the band bending, but reduces the emission lifetime because of the increased electron-hole wave function overlap. Alternatively, the adsorbed DNT reduced the nonradiative recombination by shifting or removing the intrinsic surface state. This process results in increase of the emission intensity and lifetime because the total emission lifetime (t) is dependent on the radiative lifetime (t_{rad}) and nonradiative lifetime (t_{nonrad}) in the form of $\frac{1}{\tau} = \frac{1}{\tau_{rad}} + \frac{1}{\tau_{nonrad}}$. In the measurement, 100 ppb of DNT vapor was delivered into the chamber to observe the response. The results show that the emission intensity from the device increased after the DNT vapor was introduced, following the same trend as the stimulated emission regime. At the same time, the measured emission lifetime became longer, as shown in Fig. 3.8. These results indicate that the dominant sensing mechanism relies on surface recombination velocity modification.

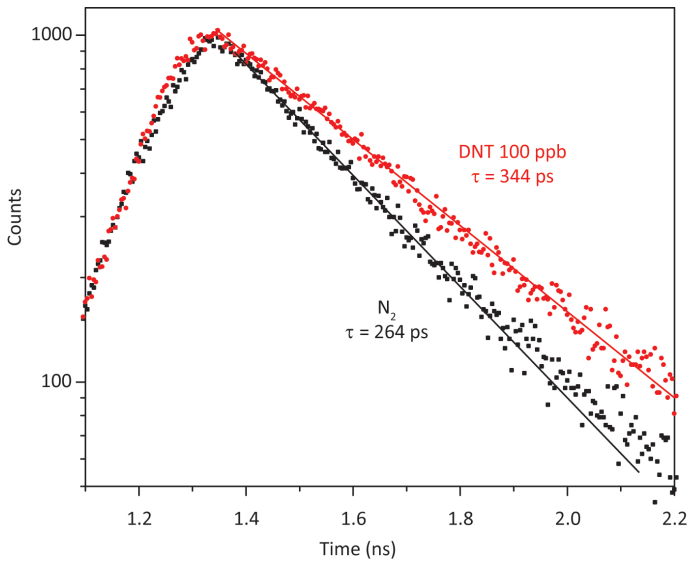

Figure 3.8 Time-resolved emission of the sensor in the spontaneous emission for investigating dynamics of the photon-excited carrier relaxation. Two of the typical time-resolved spontaneous emissions of the device in N_2 and 100 ppb DNT are shown as the black curve and the red curve, respectively. After introducing the DNT vapor, the emission intensity from the device increased, following the same trend as the stimulated emission region. The measured emission lifetime became longer. Both of these intensity and lifetime changes of the spontaneous emission suggest that the intensity increase is because of the surface recombination velocity modification.

3.6 Summary and Future Prospect

In summary, I proposed and experimentally demonstrated the actively excited plasmon sensor for detecting sub-ppb level explosive molecules for the first time, making three findings: (1) while the solid-state semiconductor simultaneously acted as optical gain and as sensing medium in active plasmon sensors, the devices held good selectivity due to the specific electron deficiencies of target explosive molecules; (2) the sensitivity of lasing emission from the calibration curve was ~300 times higher than that of spontaneous emission because the lasing emission has much stronger intensity and higher slope efficiency; (3) the direct monitoring of lasing intensity had superior performance over the monitoring of wavelength shifts due to the index change. These results demonstrate the potential of actively excited surface plasmon for chemical sensing in general and will open new opportunities in a variety of chemical-sensor–related fields, including early-stage disease diagnosis, toxic gas, and explosive detections as well as biomolecular sensing. Moreover, the use of *active* plasmon to study the surface reactions on the semiconductors will become a highly attractive platform to the scientific fields of surface chemistry and physics.

References

1. Rose, A., Zhu, Z., Madigan, C. F., Swager, T. M., Bulovic, V. Sensitivity gains in chemosensing by lasing action in organic polymers. *Nature* **434**, 876-879 (2005).

2. Huang, X.-J., Choi, Y.-K., Chemical sensors based on nanostructured materials. *Sensors and Actuators B* **122**, 659–671 (2007).
3. Peng, G., et al. Diagnosing lung cancer in exhaled breath using gold nanoparticles. *Nature Nanotechnology* **4,** 669-673 (2009).
4. Liu, N., Tang, M. L., Hentschel, M., Giessen, H., Alivisatos, A. P. Nanoantenna-enhanced gas sensing in a single tailored nanofocus. *Nature Materials* **10** 631-636 (2011).
5. He, L., Ozdemir, S. K., Zhu, J., Kim, W., Yang, L., Detecting single viruses and nanoparticles using whispering gallery microlasers. *Nature Nanotechnology* **6,** 428-432 (2011).
6. Erickson, D., Serey, X., Chen, Y.-F. & Mandal, S. Nanomanipulation using near field photonics. *Lab Chip* **11,** 995 (2011).
7. White, I. M. & Fan, X. On the performance quantification of resonant refractive index sensors. *Opt. Express* **16,** 1020–1028 (2008).
8. Barnes, W. L., Dereux, A. & Ebbesen, T. W. Surface plasmon subwavelength optics. *Nature* **424,** 824–830 (2003).
9. Anker, J. N., Hall, W. P., Lyandres, O., Shah, N. C., Zhao, J., Van Duyne. R. P. Biosensing with plasmonic nanosensors. *Nature Materials* **7** 442-453 (2008).
10. Beeram, S. R., and Zamborini, F. P., Selective Attachment of Antibodies to the Edges of Gold Nanostructures for Enhanced Localized Surface Plasmon Resonance Biosensing. *J. Am. Chem. Soc.* **131**, 11689–11691 (2009).
11. Kabashin, A. V., et al. Plasmonic nanorod metamaterials for biosensing. Nature Materials **8**, 867-871 (2009).
12. Cubukcu, E.; Zhang, S.; Park, Y.-S.; Bartal, G.; Zhang, X. Split ring resonator sensors for infrared detection of single molecular monolayers *Applied Physics Letters* 95, 043113 (2009).
13. Li, J. F., et al. Shell-isolated nanoparticle-enhanced Raman spectroscopy. *Nature* **464**, 392-395 (2010).
14. Otte, M. A., et al. Identification of the Optimal Spectral Region for Plasmonic and Nanoplasmonic Sensing. *ACS Nano* **4**, 349–357 (2010).
15. Gao, H., et al. Using the Angle-Dependent Resonances of Molded Plasmonic Crystals To Improve the Sensitivities of Biosensors. *Nano Lett.* 10, 2549–2554 (2010).
16. Mayer, K. M., Hafner, J. H., Localized Surface Plasmon Resonance Sensors. *Chem. Rev.* **111**, 3828–3857 (2011).
17. Chen, S., Svedendahl, M., Van Duyne, R. P., Kall, M., Plasmon-Enhanced Colorimetric ELISA with Single Molecule Sensitivity. *Nano Lett*. 11, 1826–1830 (2011).
18. Yanika, A. A., et al. Seeing protein monolayers with naked eye through plasmonic Fano resonances. *Proc Natl Acad Sci* **108**, 11784-11789 (2011).
19. Brolo, A. G., Plasmonics for future biosensors. Nature Photonics **6**, 709-713 (2012).
20. Escobedo, C., Brolo, A. G., Gordon, R., Sinton, D., Optofluidic Concentration: Plasmonic Nanostructure as Concentrator and Sensor. *Nano Lett*. **12**, 1592-1596 (2012).
21. Vahala, K. J., Optical Microcavities. *Nature* **424**, 839-846 (2003).

22. Vollmer, F., Arnold, S. Whispering-gallery-mode biosensing: label-free detection down to single molecules. *Nature Methods* **5**, 591-596 (2008).
23. Seker, F., Meeker, k., Kuech, T. F., Ellis, A. B. Surface Chemistry of Prototypical Bulk II-VI and III-V Semiconductors and Implications for Chemical Sensing. *Chem. Rev.* **100**, 2505-2536 (2000).
24. Deng, C. et al. Conjugated Polymer−Titania Nanoparticle Hybrid Films: Random Lasing Action and Ultrasensitive Detection of Explosive Vapors. *J. Phys. Chem. B* **114**, 4725–4730 (2010).
25. Thomas, S. W., Joly, G. D. & Swager, T. M. Chemical sensors based on amplifying fluorescent conjugated polymers. *Chem. Rev.* **107**, 1339-1386 (2007).
26. Toal, S. J. & Trogler, W. C. Polymer sensors for nitroaromatic explosives detection - Journal of Materials Chemistry. *Journal of Materials Chemistry* **16**, 2871-2883 (2006).
27. Owens, D. & Malliaras, G. G. Organic Semiconductors in Sensor Applications. Springer, *Page 171* (2008).
28. Alivisatos, A. P., Gu, W. & Larabell, C. Quantum dots as cellular probes. *Annu Rev Biomed Eng* **7**, 55-76 (2005).
29. Ippen, E., Shank, C. & Dienes, A. Rapid Photobleaching of Organic Laser Dyes in Continuously Operated Devices. *IEEE Journal of Quantum Electronics* **7**, 178-179 (1971).
30. Dubois, A., Canva, M., Brun, A., Chaput, F. & Boilot, J. P. Photostability of dye molecules trapped in solid matrices. *Applied Optics* **35**, 3193-3199 (1996).
31. Kaminow, I. P., Stulz, L. W., Chandross, E. A. & Pryde, C. A. Photobleaching of Organic Laser Dyes in Solid Matrices. *Applied Optics* **11**, 1563-1567 (1972).
32. Bergman, D. J. & Stockman, M. I. Surface Plasmon Amplification by Stimulated Emission of Radiation: Quantum Generation of Coherent Surface Plasmons in Nanosystems. *Physical Review Letters* 90, 027402 (2003).
33. Hill, M. T. et al. Lasing in metal-insulator-metal sub-wavelength plasmonic waveguides. *Optics Express* 17, 11107-11112 (2009).
34. Noginov, M. A. et al. Demonstration of a spaser-based nanolaser. *Nature* 460, 1110-1113 (2009).
35. Oulton, R. F. et al. Plasmon lasers at deep subwavelength scale. *Nature*, 461, 629-632 (2009).
36. Ma, R.-M.; Oulton, R. F.; Sorger, V. J.; Bartal, G.; Zhang, X. Room temperature sub-diffraction-limited plasmon laser by total internal reflection. *Nature Materials* **2011**, 10**,** 110-113.
37. Khajavikhan, M. et al. Thresholdless nanoscale coaxial lasers *Nature* **2012**, 482, 204–207.
38. Lu, Y.-J. et al. Plasmonic Nanolaser Using Epitaxially Grown Silver Film. *Science* **337,** 450-453 (2012)
39. Ma, R.-M.; Yin, X. B., Oulton, R. F.; Sorger, V. J.; Zhang, X. Multiplexed and Electrically Modulated Plasmon Laser Circuit. *Nano Letters* **12** 5396-5402 (2012).
40. Lawandy, N. M. Localized surface plasmon singularities in amplifying media. *Applied Physics Letters* **85**, 5040 (2004).

41. Gordon, J. A. & Ziolkowski, R. W. Investigating functionalized active coated nanoparticles for use in nano-sensing applications. *Optics Express* **15**, 12562-12582 (2007).
42. Li, Z.-Y. & Xia, Y. Metal Nanoparticles with Gain toward Single-Molecule Detection by Surface-Enhanced Raman Scattering. *Nano Letters* **10**, 243-249 (2010).
43. Skoog, D. A., Holler, F. J. & Crouch, S. R. Principles of instrumental analysis *6th edition* Publisher: Thomson Learning (2006).
44. Sohn, H., Calhoun, R. M., Sailor, M. J., & Trogler, W. C., Detection of TNT and Picric Acid on Surfaces and in Seawater by Using Photoluminescent Polysiloles. *Angew. Chem. Int. Ed.* **40**, 2104-2105 (2001).
45. Drake, H. L., Küsel, K., & Matthies, C., Acetogenic Prokaryotes. *Prokaryotes* 2:354–420 (2006).
46. Uchimiya, M., Gorb, L., Isayev, O., Qasim, M. M. & Leszczynski, J. One-electron standard reduction potentials of nitroaromatic and cyclic nitramine explosives. *Environmental Pollution* **158,** 3048–3053 (2010).

Chapter 4

Novel Imaging Technologies for Studying and Synthesizing 3D Soft Matters

4.1 Nanowire Interferometry

4.1.1 Introduction to Brownian Motion (BM) and Hydrodynamic Interaction (HI)

Microscopic particles undergo Brownian motion due to the random collision of fluid molecules. It is fundamentally important to understand artificial particles' Brownian motion. Because particles that share characteristic physical dimensions with biological molecules also share their characteristic diffusive behavior, a study of the experimentally observable artificial particle's diffusion allows us to understand the behavior of nanoscale biological molecules. Moreover, this study itself is a fundamental research field of soft condensed matter physics including colloidal physics and many particle systems.

Brownian motion of a free particle is predicted by Einstein's theory as follows [1]:

$$MSD = \left\langle [\Delta x(t)]^2 \right\rangle = 2D\Delta t \qquad (4.1.1)$$

where MSD is the mean square displacement of a free diffusive particle in one dimension during time Δt and D is its diffusivity. The Stokes Einstein equation links the diffusivity with thermal energy as follows:

$$D = k_B T/\gamma \qquad (4.1.2)$$

where k_B is the Boltzmann constant, T is the temperature, and $\gamma = 6\pi\eta R$ is the Stokes friction coefficient for a sphere with radius R in the viscosity of the fluid η. Although these equations predict the observable behavior of the Brownian particles, their dynamics with mass M over all time scales can be described by a Langevin equation [2–4]:

$$M\ddot{x} + \gamma\dot{x} = F_{thermal}(t) \qquad (4.1.3)$$

$$F_{thermal}(t) = \sqrt{2k_B T\gamma}\varsigma(t) \qquad (4.1.4)$$

$F_{thermal}(t)$ is the Brownian stochastic force and $\varsigma(t)$ is the normalized white noise process, characteristically for all t and t':

$$\left\langle \varsigma(t) \right\rangle = 0 \text{ and } \left\langle \varsigma(t)\varsigma(t') \right\rangle = \delta(t - t') \qquad (4.1.5)$$

On the other hand, in most realistic situations in biological and technological applications, the particles' surroundings influence the Brownian motion via electrokinetic force, Wan der Waals force, and other kinds of confining forces. This external force term $F_{external}(t)$ will be added to the right side of equation (4.1.3), affecting the Brownian motion at the time scales, depending on its strength. Understanding the soft matter physics systems is to understand parameters such as γ and $F_{external}(t)$ and how they contribute to the mentioned equations. There are complex factors in the environment that alter the Brownian motion of a free particle. The Wan der Waals force plays important roles especially when the particle is extremely close to the surface; it becomes significant at the distance < 10nm [5]. If there is an electric field in the fluid, the electrokinetic force can also influence its behavior. However, in an ionic liquid, the small ions are attracted to the environments to cancel the electric field from the environments. In colloidal systems where particles can be observed in optical imaging (> hundreds of nanometers), consequently, the dominant force interaction takes place through hydrodynamic interaction.

Hydrodynamic interaction (HI) is a force communication between objects mediated by the fluid flows induced by the motion of the objects themselves [6]. This HI's effects appear even at distances ranging from nanoscales to very large scales up to the size of the particles, thus playing important roles in many realistic situations such as motion of molecules and cells [7-16] as well as the self-assembly of colloidal objects [17-20]. The particles' HI with a planar interface is one of the simplest cases, but even that is complex to understand because HI is essentially an infinite-order multireflection of fluid flows between objects. The case of spherical particles' interaction with the planar wall has been extensively studied as a basis for understanding the realistic systems [21-25]. H. Brenner's pioneer work in the 1960s [24] analytically proposed that the diffusivity of spheres exponentially drops in an anisotropic manner as the particle-wall distance becomes closer than the particle diameter. After the advance of the microscopic precision measurement technique for tracking the particles' position, this prediction was experimentally confirmed [22]. With this established basis of sphere-wall hydrodynamic interactions, it became possible to understand the interaction of spherical particles with more realistic environments.

On the other hand, in many realistic biological and technological systems, microscopic objects such as bacterial cells [7-10], filamentous macromolecules [11-16], and colloidal particles [17-20] are anisotropic and confined by boundaries such as substrate surfaces and cell membranes. Understanding their complex HI of anisotropic particles near a boundary is crucial for comprehending the real dynamics in the motion of molecules and cells [7-10] as well as the self-assembly of anisotropic objects such as nanowires [17-20] in a liquid. For example, immobilization of anisotropic particles always starts with the tethering of one end when the particles experience the strong hydrodynamic effect from the wall. However, the behavior of anisotropic particles in environments is not yet fully studied due to its complexity.

4.1.2 HI of Anisotropic Particles with a Wall

The Brownian motion of anisotropic particles is subject not only to the solvent flows reflected from the environment but also to those induced by the motion of the particles themselves, making the Brownian motion difficult to understand [16, 26-28].

Recent studies have revealed that the HI induced by the particle itself (i.e., even in an isotropic environment) causes the coupling between the translational and rotational diffusions of rod-like particles [26]. Despite such recent progress, the HI with the nearby interfaces further increases the complexity, hampering its theoretical understanding [27-28]. There is no analytical solution developed for this problem and no numerical method to efficiently simulate such a large system. Experimentally, it has been difficult to observe the near-wall Brownian motion of such anisotropic particles with conventional optical methods because of complicated light scatterings. Particularly, direct visualization of the minute change of the inclined angle between the moving particle and the surface has been elusive [15, 28], and previous works typically assumed the particle was parallel to the wall [26].

In this chapter, I experimentally and theoretically studied the hydrodynamic interaction between anisotropic particles and a wall. I proposed and demonstrated an interferometric imaging technique to track the microscopic 3D rotational motion of tethered nanowires, a simplest one-dimensional shape of anisotropic particle. In parallel, I developed an implicit hydrodynamic model to simulate a large system efficiently and accurately.

This quantitative measurement with high angular and temporal resolutions revealed significantly inclined angle- and length-dependent hydrodynamic effects in the Brownian motion for the first time. I observed a 40–80% reduction in the overall rotational diffusivity of nanowires. The implicit simulation efficiently takes the wire-wall hydrodynamic interactions into account, and its results correlated positively with experimental observations with no fitting parameter. The combination of the developed experimental and simulation techniques provides a powerful platform for exploring the optimal self-assembly conditions of nanostructures and for studying the microrheology of soft condensed matters, such as colloidal and biological systems near interfaces.

4.1.3 Nanowire Interferometry (Backscattering Interference Contrast Microscope)

Introduction: Interference Contrast Microscopy

Reflection interference contrast microscopy (RICM) is an interferometric microscopy technique with many applications in cell biology, surface science, wetting, and soft condensed matter research [20, 31]. The intensity distribution of the interferogram is a result of the local difference in the lengths of optical paths between the light waves reflected from different interfaces of the systems. The optical basis for interferences occurring in RICM is depicted in Fig. 4.1.1a. A monochromatic incident light ray I_0 is first reflected at the glass/water interface, yielding ray I_1. The transmitted light is reflected further at the surface of the object (object/water interface) to generate ray I_2. For the observer, rays I_1 and I_2 interfere to generate interferometric intensity profile I. Assuming quasi-normal incidence I is given by equation (4.1.1), where $k = 2\pi n_1/\lambda$ and ϕ is a phase shift usually equal to π, $h(x, y)$ is the distance between the object and the glass/water interface at its lateral position. Because I_1 and I_2 depend only on I_0 and the reflection coefficient at each interface, the last term that is a function of h results in the appearance of contrast in RICM. In a reverse manner, one can mathematically interpret the two-dimensional matrix of intensities in the RICM image as

the corresponding substrate/object distance accurately. For example, large colloidal beads generate the circular symmetric fringe patterns that can be exploited to accurately and robustly track robustly with great accuracy, 1 nm vertically and 10 nm (sub-pixel) laterally [32].

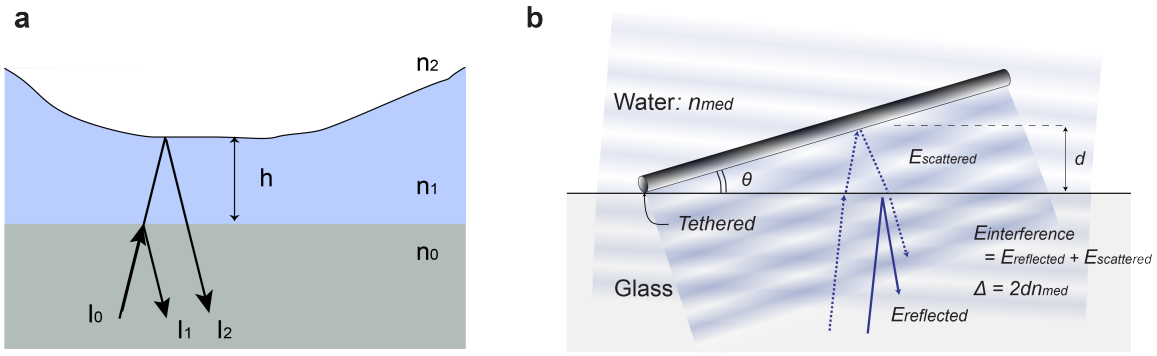

Figure 4.1.1. The principle of reflection interference contrast microscopy (a) and the Mie resonance-enhanced backscattering interference contrast microscopy developed in this work (b).

$$I = I_1 + I_2 + I_1 I_2 \cos[2kh(x,y) + \phi] \qquad (4.1.1)$$

Despite its advance, the RICM research is not directly applicable to nanoscopic objects because the nanoscale material randomly scatters the optical rays with a significant non-π phase shift, causing simple interpretation to become challenging. Thus, in this work, Mie resonance-enhanced *backscattering* interference contrast microscope (BICM) was developed for tracking the microscopic motion of a tethered silicon nanowire (Figure 4.1.1b). In the case of our nanowires, it is a scattering process that did result in weaker signals, multidirectional scattering, and phase change of the scattered photons; RICM was thus hard to apply. However, the high uniformity of the nanowires allowed the phase change to appear uniformly along its length. Its Mie resonance gave a significantly strong backscattering toward the glass substrate [33], resulting in a high-contrast interferogram that allowed precise measurement of the object/substrate.

Mie Resonance-Enhanced *Backscattering* Interference Contrast Microscope (BICM)

For the experiments discussed from here, a suspension of silicon nanowires (150 nm in diameter, with lengths varying from 5 to 25 μm) was stored in a closed chamber on a glass cover slip. Some of the nanowires had one end tethered to the glass surface, due to the Van der Waals force, and the other end free, undergoing Brownian rotation around the tethered point (Figure 4.1.1b). As seen in the SEM picture (Fig. 4.1.2), the commercialized nanowires from Sigma have a high-quality scattering surface that is uniformly smooth and flat along the length of the wire, thus suitable for BICM. The nanowires used in the experiments are rigid enough that bending is negligible. For the nanowires in liquid, the possible effect of bending on Brownian motion can be characterized by the persistence length, $L_p = \kappa/k_BT$ [34], where κ is the bending stiffness. $\kappa = EI$, where E is the elastic modulus and I is the area moment of inertia about the filament axis ($I = \pi d^4/64$ [34]). Using Young's modulus of silicon (E ~130 GPa) [35, 36] and assuming that the silicon nanowires are cylinders with d = 150 nm, we obtain the

persistent length to be L_p = 785 m, which is far longer than the length of the nanowire we used (< 25 microns).

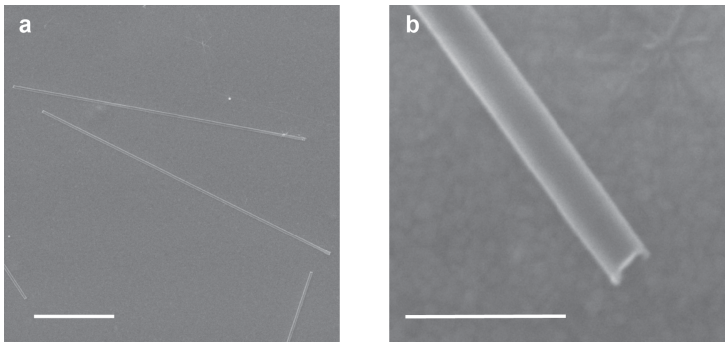

Figure 4.1.2. SEM images of silicon nanowires. (a) An SEM image of highly uniform silicon nanowires with 150 nm diameter (from Sigma, Scale bar = 5 μm). (**b)** A magnified SEM image of an end of the nanowire (scale bar = 500 nm).

In the BICM setup as shown in Fig. 4.1.3, a mercury lamp was used as the illumination light source, from which monochromatic light was selected using band-path filters. The monochromatic light passed through a narrow aperture of 0.5 mm, placed at the Fourier plane, and was focused onto the glass surface plane with an objective lens (Carl Zeiss, 50x LD Epiplan HD DIC, working distance = 6.5 mm, NA = 0.5). The same lens then collected the backscattered light from the nanowire along with the reflected light from the glass-water interface, generating the interference pattern along the wire. The intensity profile of the interference pattern, I, is interpreted to calculate the inclination angle as follows [31]:

$$2I = (I_{max} + I_{min}) - C\,\frac{I_{max}-I_{min}}{2}\,cos\left\{\frac{4\pi n_w}{\lambda}\left[h - sin^2\left(\frac{\alpha}{2}\right)\right] + \phi\right\} \qquad (4.1.2)$$

where I_{max} and I_{min} are the maxima and minima intensity of the interference pattern, C is the correction constant in contrast amplitude, n_w is refractive index of water, h is the distance from the wall, α is half the illumination cone angle defined with illumination numerical aperture as $INA = n_w \sin\alpha$, and ϕ is the phase shifts seen in the pattern. As the nonzero numerical aperture generally introduces effects of damping the interference contrast and of slightly stretching its periods, represented as C and α, the small aperture of 0.5 mm diameter was placed at the Fourier plane and effectively reduced the INA to 0.05, minimizing the measurement errors [31].

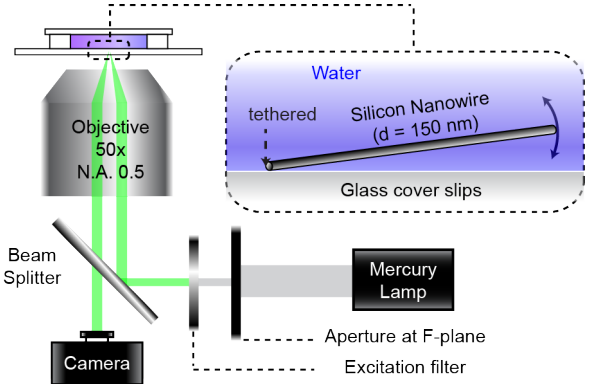

Figure 4.1.3. Optical setup, used to enable the Mie resonance-enhanced backscattering interference contrast microscopy.

The proposed BICM was calibrated using the nanowire with fabricated structures. As shown in Fig. 4.1.4a, a silicon dioxide layer was partially deposited with e-beam evaporation and, after enclosing the SiO2 structure in the chamber, the nanowire solution was introduced at high ion strength. After the waiting period, some nanowires settled down at the bottom and leaned on the edge of the deposited the SiO2 structure. The BICM was then applied for the leaning nanowire that ceased to diffuse. The measurement on nanowires was performed in water because, when dry, a nanowire bends due to capillary forces, as seen in Fig. 4.1.4g. The same mercury lamp and objective lens were used. Fig. 4.1.4b is the transmission bright field image of the wire leaning on the SiO2 structure. The upper area above the dash line is the surface of the original glass cover slip, and the lower area is the surface of the deposited SiO2 structure. Fig. 4.1.4c is the backscattering interference contrast image under illumination of light at wavelength 436 $\pm$ 10 nm, Fig. 4.1.4d is at 546 $\pm$ 5 nm, and Fig. 4.1.4e is at 665 $\pm$ 22 nm. In Fig. 4.1.4f, plots show the intensity profile measured along the wire length in Figs. 4.1.4b–d; the curves were drawn according to the equation (Eq. 4.1.2) with λ = 436, 546, and 665 nm. For the wavelength of 546 nm, the significant shift in phase caused by the resonance of the nanowire was observed. The wire diameter was comparable to the effective wavelength of visible light at the refractive index of silicon, and the nanowires are thus at Mie resonance when applied to visible light. Because this phase shift does not affect the periodicity of the interference pattern, the theoretical curve could still fit well with the measured intensity profile. For the fitting, although ϕ for 436 nm and 665 nm were zero, ϕ for 546 nm was 0.4. The heights of the SiO2 structure were measured by BICM as 673.98 nm at λ = 436 $\pm$ 10 nm, 675.8 nm at λ = 546 $\pm$ 5 nm, and 672.17 nm at λ = 665 $\pm$ 22 nm. The fitting was made from the left side of the interference pattern; its right side near the deposited SiO2 structure was distorted due to the complex light scattering by the edge of the deposited wall. After the BICM measurement, the sample was taken out from the chamber and dried to be imaged by the atomic force microscope (AFM) (Figs. 4.1.4g and h). The strong surface tension generated during the drying of the structures distorted the nanowire toward the bottom, as seen in Fig. 4.1.4g. The measured step height of the deposited structure was 681 nm (Fig. 4.1.4h). With consideration of the layers of dried solutes, the accuracy of our optical measurement was confirmed.

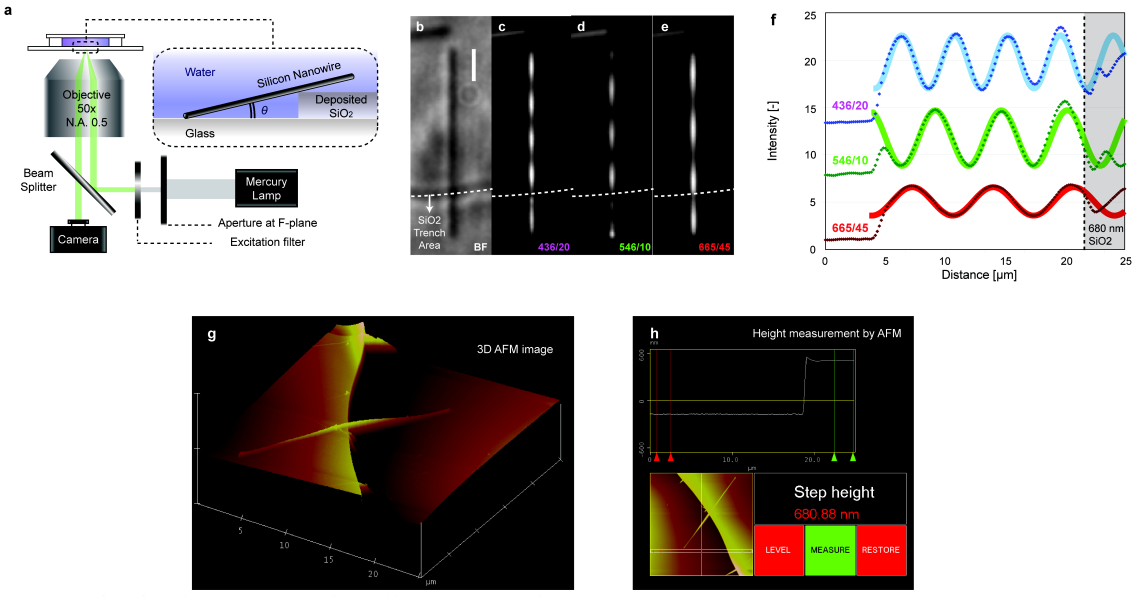

Figure 4.1.4. Calibration of BICM was performed using the partially deposited silicon dioxide structure. (a) schematic**, (b–d)** are transmission of the bright field image and BICM image of the nanowire leaning on the glass trench. schematic**. (b–d)** are illuminated with λ = 436, 546, and 665 nm of light, respectively. (**e)** shows the fitting of experimentally observed interference patterns in (**b-d)** with the equation (4.1.2). (**g)** shows the AFM image of the nanowire on the trench after drying the structures, and (**h)** depicts the trench height. The strong surface tension generated in drying the structures distorted the nanowire toward the bottom, as seen in **g**. The measured step height of the deposited structure was 681 nm (**h**).

When the BICM with the monochromatic light illumination is applied to image the Brownian motion of the tethered nanowire, the high contrast interference pattern enables measuring the inclination angle (θ) at high angular (up to ~10^{-5} radian, corresponding to 1 Å displacement of the free end of a 10 μm nanowire) and temporal (< 0.004 s) resolutions, wherein the MATLAB-based sub-pixel fitting performs pattern interpretation. Such information is impossible to obtain in a dark-field image (Fig. 4.1.5). The same objective lens was used for acquiring both BICM and dark field images. The dark-field image was acquired by using a dark-field cube to illuminate the sample at large incident angles and collected only the back-scattered light, while the interference image was acquired by using a beam splitter (50/50) with a narrow aperture. On the other hand, direct measurement of the azimuth angle (φ) at a high resolution (up to an order of ~10^{-5} radian) was achieved by fitting the image of the nanowire with a single ellipse in the MATLAB software, similar to localization-based microscopic techniques. Thus, a single interference image measured both the inclined and azimuth angles simultaneously, enabling tracking of the 3D Brownian motion of the tethered nanowires accurately in 3D space (Fig. 4.1.6).

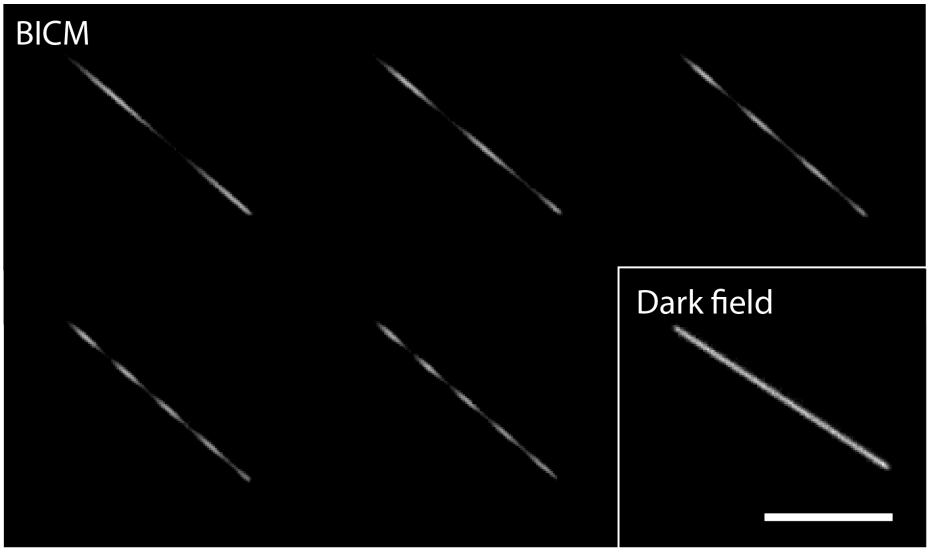

Figure 4.1.5. Typical BICM images of a tethered silicon nanowire. Interpretation of these interference patterns into the inclined angle between the nanowire and a wall and ellipsoidal fitting with the whole nanowire's shape enables tracking of the motion of in 3D. In contrast, such rich information cannot be obtained by dark-field microscopy (right bottom) (scale bar = 10 μm).

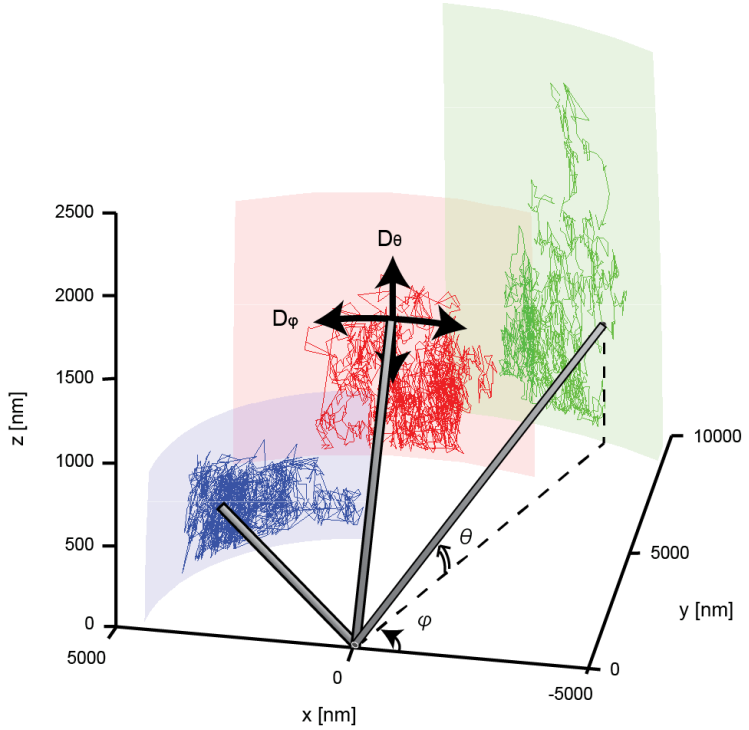

Figure 4.1.6. The accurate tracking of 3D Brownian motion of tethered nanowires. This figure shows three different nanowires with different lengths. The developed methods enable the tracking at high spatial and temporal resolutions.

4.1.4a Experimental Result (Overall Behavior)

The continuous measurement of the 3D Brownian motion of tethered nanowires revealed the length-dependent anisotropic reduction in their rotational diffusion, attributed to the complex hydrodynamic interaction (HI) between the nanowire and a substrate wall. Fig. 4.1.7a displays the typical angular mean-square displacements (AMSDs) of nanowires over long time. I observed that the AMSDs of all nanowires in both inclined and azimuth directions increase linearly at short time scales (< 0.1s). Their motions were diffusive and thus followed the general law of Brownian motion [1]:

$$AMSD_{\theta,\phi} = \left\langle \Delta\theta^2, \Delta\phi^2 \right\rangle = 2D_{\theta,\phi}\Delta t \qquad (4.1.3)$$

At longer time scales, the mean-square displacement reached a plateau, with large fluctuations. Although the exact nature of the tethering is not yet fully understood, the nanowires experienced a weak confinement that limits their diffusion at long time scales. Luckily, this weak confinement does not affect the study of the Brownian motion at short time scales, as explained in the following. The dynamics of the Brownian motion of a particle with a confinement can be described by a Langevin equation [2]:

$$m\ddot{x} = -\gamma\dot{x} + F_{thermal} + F_{confine}(x) \qquad (4.1.4)$$

where the first term at the right side of the equation is the damping force, the second term is the random thermal force due to the collisions with molecules, and the last term is the force due to weak confinements. At short time scales, the effects of the thermal force dominate because the confinement is weak. At long time scales, however, the effects of the thermal force are averaged out because this force is random, while the effects of the weak confinement, most likely because of combined effects, including gravity, tether, and a wall, is deterministic. As seen in the histogram of the angle distribution of one example of tethered nanowire (15 μm) shown in Fig. 4.1.8a, their motion is indeed constrained near the wall, which results in the plateau at the long time scales. By applying the measured distribution in Boltzmann distribution [37]:

$$e^{-Ep(\theta)/k_BT}/(\Sigma e^{-Ep(\theta)/k_BT}) \qquad (4.1.5)$$

the shape of the constraining potential, E_p, is estimated, as shown in Fig. 4.1.7b. The shape of potential clearly demonstrates that a constraining force is acting on the nanowire. Such quantitative estimation indicates that each of the possible explanations contributes to this restriction in a complex manner. When estimating how long it takes for the nanowire to diffuse to move across the constraining potential from $<\Delta\theta^2>=2D_\theta\Delta t$, where $\Delta\theta$ and D_θ are assumed to be 0.02 and 0.0002 (from Fig. 4.1.6), Δt is about 1 second, correlating with the time scale in Fig 4.1.7a, which starts to show the plateau. Again, a weak confinement does not affect the short-time Brownian motion but affects the system at long time scales. The linear increase of the AMSD curves in Fig. 4.1.7 for the short time scales means the particles diffuse freely at short time scales. The well-studied Brownian motion of microspheres trapped by optical tweezers also suffers similar

confinement, which affects the long-time behavior of the system but does not affect the short-time Brownian motion [38].

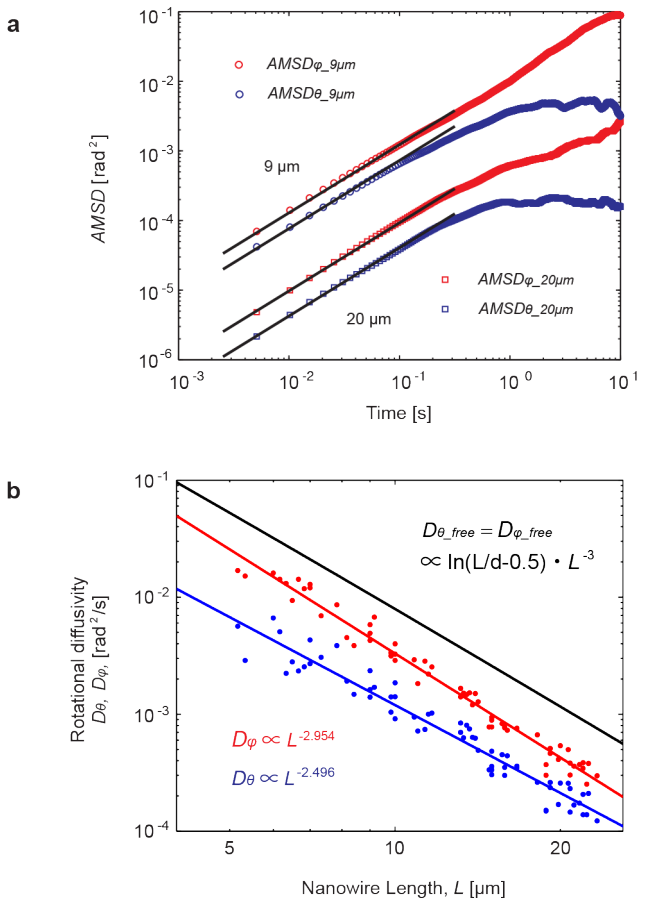

Figure 4.1.7 Measurement of overall angular mean-square displacements (AMSDs) of tethered nanowires and their rotational diffusivities. In **(a)**, a double logarithmic plot of the overall AMSDs of sampled nanowires shows the diffusive behavior ($\propto t$, shown as black lines with slope 1) at short time scales (< 0.1 s). Red and blue circles are the azimuth and inclined AMSDs of a 9-μm nanowire, respectively. Squares are those of a 20-μm nanowire. Their positional data were taken at 250 Hz and 180 Hz, respectively, for more than 30,000 frames. In **(b)**, the rotational diffusivities of the free end of the nanowires in the inclined (D_θ, red circles) and azimuth (D_φ, blue circles) orientations shows a more significant hydrodynamic wall effect in D_θ in an anisotropic manner. A black curve is drawn with an analytical solution for free rotational diffusivity of a cylindrical rod (no wall). D_θ and D_φ follow different power laws as a function of the lengths $\sim L^{-2.5}$ and $\sim L^{-3}$ in good approximation for the rods we observed (<6% and <3% errors, respectively). This power law causes more significant anisotropy in the rotational motion for shorter nanowires. The data were taken from 65 wires in total.

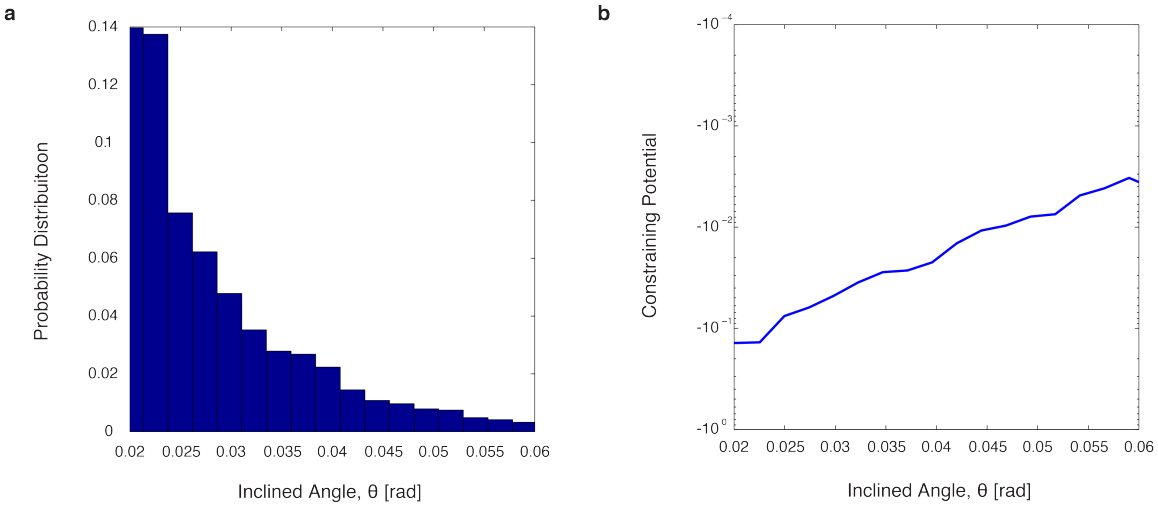

Figure 4.1.8. Weak confinement that creates the plateau in the AMSD at long time scales. (a) A typical distribution of inclined angles. (**b**) Estimated potential obtained from distribution (**a**).

From the slopes, $\langle \Delta\theta^2 \rangle = 2D_{\theta,\varphi}\Delta t$, the angular diffusivities ($D_{\theta,\varphi}$) were obtained for the nanowires with lengths ranging from 5 to 25 μm. In Fig. 4.1.6b, compared to the numerically calculated free rotational diffusivity of a nanowire around one end, the measured rotational diffusivities showed hindered, anisotropic diffusion due to the HI with the wall (numerical method is described in Section 4.1.5). The reduction in D_θ was larger than that in D_φ because a larger portion of reflected flows from the wall is directed back toward the wire, resulting in preferential reduction of the diffusion in the θ direction. The D_θ and D_φ follow different power laws as a function of the length, $\sim L^{-2.5}$ and $\sim L^{-3}$, respectively, in pretty good approximation for the observed rods (< 6% and < 3% errors, respectively), where L is the nanowire length. This power laws resulted in more significant anisotropy in the rotational motion for the shorter wires due to $D_\theta/D_\theta \sim L^{-0.5}$. These results indicate that particles with smaller anisotropy experience more significant HI as they have a larger portion of length near the surface.

4.1.4b Experimental Result (Short Time Scales)

Although Fig. 4.1.7 revealed the overall diffusive behavior of the tethered nanowires, the fast and accurate BICM further enabled measurement of angle-dependent hydrodynamic interactions that dynamically change during the long diffusion. The overall trajectory for each nanowire used in Fig. 4.1.7 was sorted according to the initial inclined angle, θ_{init}, and the AMSD values were recalculated for each sorted data subset. At short time scales, the AMSDs sorted with a different θ_{init} increased linearly with different slopes. The slope of the θ_{init} dropped as the θ_{init} decreased, as shown in Fig. 4.1.9a and Fig. 4.1.9b for θ and φ directions, respectively. The angle-dependent diffusivities were then evaluated as the half slope of each sorted AMSDs: $D_\theta(L,\theta_{init}) = \dfrac{\langle \Delta\theta^2 \rangle}{2\Delta t}$. At sufficiently short time scales, they were approximately independent of Δt (< 0.05 s, see Fig. 4.1.9c and Fig. 4.1.9d), suggesting that their motions followed typical Brownian motion with the locally determined diffusivity. At longer time scales, the nanowires moved away from the initial angle, θ_{init}, to different

positions, experiencing different HIs and other confinement effects from environments. This resulted in the deviation from the original local D_θ. Fig. 4.1.9e and Fig. 4.1.9f show the final results: the reduction in local D_θ was larger for shorter wire lengths and/or for a smaller initial inclined angle θ_{init}. This tendency explains the more significant reduction seen in D_θ for shorter wires in Fig. 4.1.7b. In Fig. 4.1.9e and Fig. 4.1.9f, the experimental results (dots) and the simulated ones (curves), whose details will be explained in the following sections, were plotted together, showing excellent agreement with no fitting parameter. The measurement and analysis proved the dominance of the hydrodynamic forces in the system and demonstrate the powerfulness of the experimental and numerical approaches developed in this work.

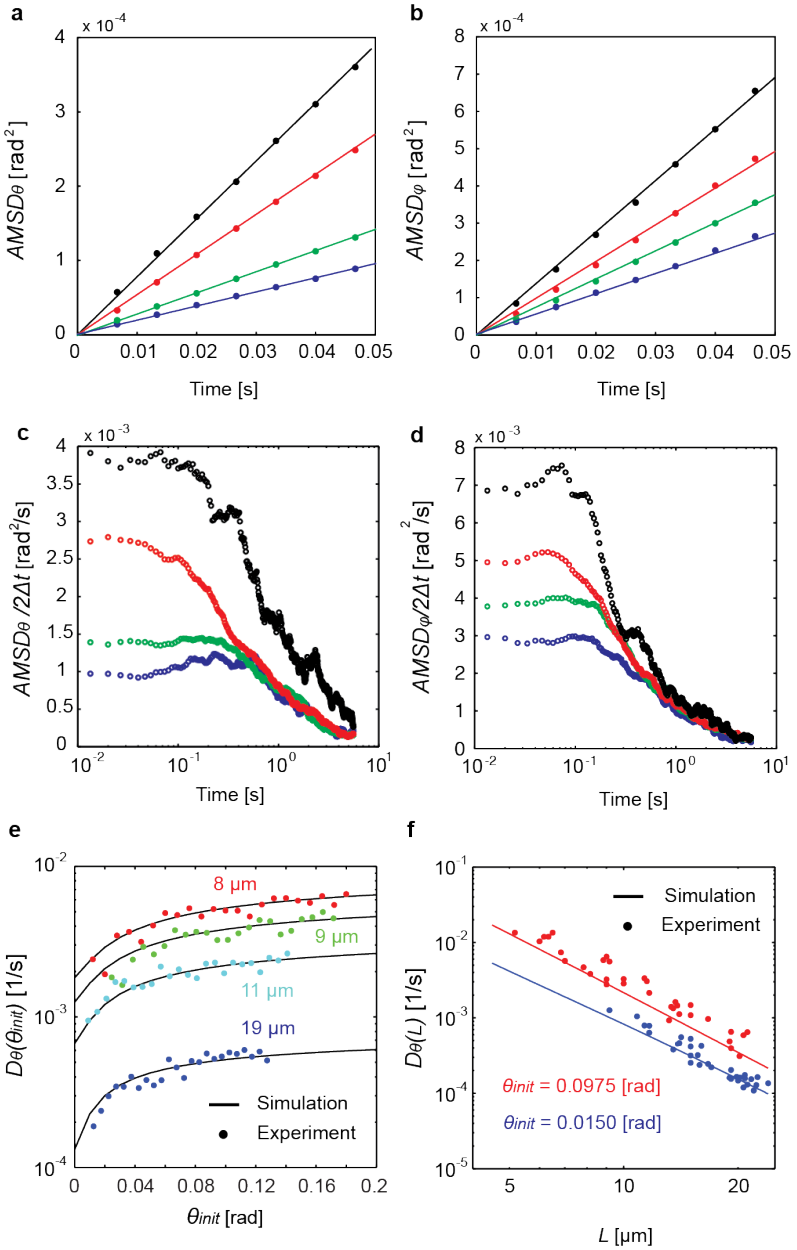

Figure 4.1.9 Measured and calculated diffusion dependence on both inclined angle and wire length. Example plots of sorted *AMSD*s in the inclined (**a**) and the azimuth (**b**) show the diffusive behavior at short

time scale (< 0.05 s), but at different slopes (diffusivity) depending on the initial inclined angle θ_{init}. The sample data was of 9-μm nanowire and sorted according to the θ_{init} by every 0.02 radian. From top to bottom, θ_{init} consisted of 0.19 (black), 0.09 (red), 0.03 (green), and 0.01 (blue) radians. (**c)** and **(d)** are the halves of AMSDs divided by time durations, showing that it is feasible to estimate the local diffusivity D_θ at the short time scales. The color and order of plots are according to those in (**a),** and (**b**), (**e),** and **(f)**, are the inclined angle- and/or length-dependent D_θ of the tethered nanowires obtained from the slopes in (**a)** and (**b)**. The results clearly show significant hydrodynamic wall effects when the wires move closer to the wall. (**c)** compares the measured angle-dependent rotational diffusivities (dots) and the numerically calculated ones (curves) at four different wire lengths. (**d)** compares the measured length-dependent rotational diffusivities for a large number of sample wires (dots) and the numerically calculated ones (curves) at two different θ_{init}. In both (**c)** and (**d)**, experimentally measured diffusivity quantitatively agreed well with the calculated values without any fitting parameters.

4.1.5a Numerical Model Development

To fully understand the effect of hydrodynamic interactions in the system, a 3D hydrodynamic model based on a string-of-beads idealization of the system is developed, and the model is implicitly solved for the hydrodynamic velocity of each bead [16]. Here the basic idea of the model is introduced with Fig 4.1.10a, in which two beads, B_1 and B_2, located at $\vec{X}_1$ and $\vec{X}_2$, respectively, are considered the simplest case. When B_1 moves at a steady speed $\vec{v}_1$ (while B_2 is stationary) in the Stokes' regime, a steady speed $\vec{v}_{1H,2}$ is induced at location $\vec{X}_2$. B_1's motion thereby exerts a drag proportional to the induced velocity $\vec{v}_{1H,2}$ on the bead B_2 and thus causes its drift. If the bead B_2 also moves at a translational velocity $\vec{v}_2$, the hydrodynamic velocities of each bead (i.e., velocity of each bead relative to the velocity of its surrounding fluid) are given by the following implicit formulations [12]:

$$\vec{v}_{1H} = \vec{v}_1 - \vec{v}_{2H,1} \qquad (4.1.6)$$

$$\vec{v}_{2H} = \vec{v}_2 - \vec{v}_{1H,2} \qquad (4.1.7)$$

Generalization of equations (1) and (2) to *N* beads leads to the following:

$$\vec{v}_{i,H} + \sum_{j=1, j\neq i}^{N} \vec{v}_{jH,i} = \vec{v}_i \qquad (4.1.8)$$

The problem of hydrodynamic velocities of a system of *N* beads therefore is reduced to a system of linear algebraic equations that is solvable using standard methods (MATLAB). The input absolute velocities, $\vec{v}_i$, are given to individual beads composing the wire and wall, and constrain their shape with respect to each other. Especially for the tethered rotation, when a wire rotates at the angular velocity $\vec{v}w$ and the n-th bead composing a wire has distance $|\vec{r}_n|$ from the tether, the absolute rotational velocity of $|\vec{r}_n||W|$ is given as input.

In more detail, for calculating the real 3D model, if B_i moves at a steady speed $\vec{v}_i$ in the Stokes' regime, its induced fluid flow at location $\vec{X}_j$ can be determined as radial ($v_{r\_i,j}$) and tangential ($v_{\theta\_i,j}$) velocity with Eq. A and B, respectively:

$$v_{r\_i,j} = \left(\frac{3a}{2\left|\vec{r}_{ij}\right|} - \frac{a^3}{2\left|\vec{r}_{ij}\right|^3} \right) \left|\vec{v}_i\right| \cos\theta_{ij} \qquad (4.1.9)$$

$$v_{\theta\_i,j} = -\left(\frac{3a}{4\left|\vec{r}_{ij}\right|} + \frac{a^3}{4\left|\vec{r}_{ij}\right|^3} \right) \left|\vec{v}_i\right| \sin\theta_{ij} \qquad (4.1.10)$$

where we define $\vec{r}_{12} = \vec{X}_2 - \vec{X}_1 = \{x, y, z\}$ and angle θ_{ij} by $\cos\theta_{ij} = \dfrac{\vec{r}_{ij} \cdot \vec{v}_i}{\left|\vec{r}_{ij}\right| \left|\vec{v}_i\right|}$.

Under this Stokes' regime assumption, the general hydrodynamic relations between beads can be represented as follows:

$$\vec{v}_{i,j} = T_{ij} \vec{v}_i \qquad (4.1.11)$$

$$T_{12} = [C_{3\times1}^{(1)}, C_{3\times1}^{(2)}, C_{3\times1}^{(3)}] \qquad (4.1.12)$$

where

$$C_{3\times1}^{(1)} = \left(\frac{3a}{2\left|\vec{r}_{1,2}\right|^3} - \frac{a^3}{2\left|\vec{r}_{1,2}\right|^5} \right) \begin{Bmatrix} x^2 \\ xy \\ xz \end{Bmatrix} - \left(\frac{3a}{4\left|\vec{r}_{1,2}\right|^3} - \frac{a^3}{4\left|\vec{r}_{1,2}\right|^5} \right) \sqrt{\frac{\left|\vec{r}_{1,2}\right|^2 - x^2}{y^2 + z^2}} \begin{Bmatrix} -(y^2 + z^2) \\ xy \\ xz \end{Bmatrix}$$

$$C_{3\times1}^{(2)} = \left(\frac{3a}{2\left|\vec{r}_{1,2}\right|^3} - \frac{a^3}{2\left|\vec{r}_{1,2}\right|^5} \right) \begin{Bmatrix} xy \\ y^2 \\ yz \end{Bmatrix} - \left(\frac{3a}{4\left|\vec{r}_{1,2}\right|^3} - \frac{a^3}{4\left|\vec{r}_{1,2}\right|^5} \right) \sqrt{\frac{\left|\vec{r}_{1,2}\right|^2 - y^2}{x^2 + z^2}} \begin{Bmatrix} xy \\ -(x^2 + z^2) \\ yz \end{Bmatrix}$$

$$C_{3\times1}^{(3)} = \left(\frac{3a}{2\left|\vec{r}_{1,2}\right|^3} - \frac{a^3}{2\left|\vec{r}_{1,2}\right|^5} \right) \begin{Bmatrix} xz \\ yz \\ z^2 \end{Bmatrix} - \left(\frac{3a}{4\left|\vec{r}_{1,2}\right|^3} - \frac{a^3}{4\left|\vec{r}_{1,2}\right|^5} \right) \sqrt{\frac{\left|\vec{r}_{1,2}\right|^2 - z^2}{x^2 + yz^2}} \begin{Bmatrix} xy \\ yz \\ -(x^2 + y^2) \end{Bmatrix}$$

When applying this representation to the generalized equation (4.1.8), the implicit hydrodynamic model of the system composed of *N* beads, Eq. (4.1.8) can be rewritten as the following linear algebraic equation to solve the hydrodynamic problem.

$$\begin{bmatrix} I_{3\times3} & T_{21} & \cdots & T_{N1} \\ T_{12} & I_{3\times3} & \cdots & T_{N2} \\ \vdots & \vdots & \vdots & \vdots \\ T_{1N} & T_{2N} & \cdots & I_{3\times3} \end{bmatrix}_{3N\times3N} \begin{Bmatrix} \vec{v}_{1h} \\ \vec{v}_{2h} \\ \vdots \\ \vec{v}_{Nh} \end{Bmatrix}_{3N\times1} = \begin{Bmatrix} \vec{v}_1 \\ \vec{v}_2 \\ \vdots \\ \vec{v}_N \end{Bmatrix}_{3N\times1} \qquad (4.1.13)$$

After obtaining the hydrodynamic velocity of each bead, the rotational friction coefficient ξ_{rot}, can be calculated. This ξ_{rot} reflects the complex hydrodynamic interaction with the wall. Because the translational friction coefficient for the spherical bead with diameter d in media having viscosity μ_w is known as $\xi_0 = 3\pi d\mu_w$, the torque equation can be represented as:

$$\xi_{rot}\omega_0 = \sum_{k=beads} \left| \vec{r}_k \times \xi_0 \vec{v}_{kH} \right| \qquad (4.1.14)$$

where $\vec{r}_k$ is the position vector of the bead B_k from the tether point. Finally, the rotational diffusivity is proportional to the inverse of the rotational friction coefficient: $D_{rot} = k_B T / \xi_{rot}$.

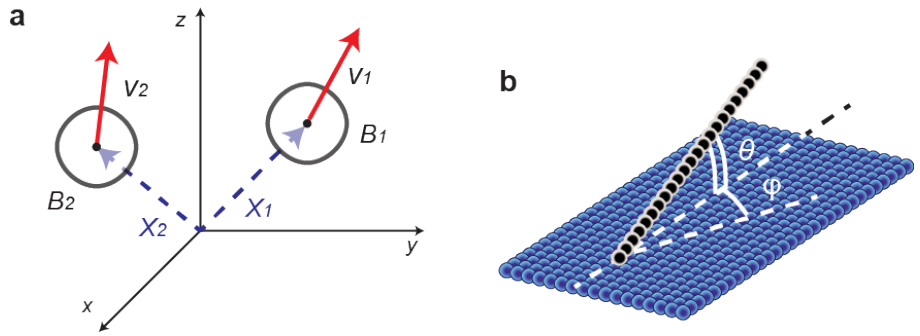

Figure 4.1.10 3D hydrodynamic simulation of the nanowire diffusion near a wall. **(a)** The implicit solution for the hydrodynamic velocity, the velocity of each bead relative to that of its surrounding fluid, considers Stokes' superposition of solvent flows efficiently (moving two beads is an example, causing multi-reflected complex flows between them. Due to its efficiency, the model can simulate very large systems, including the complex HI between the wire and a wall. **(b)** A schematic of the numerical models simulating the experiment, wherein the wire and the wall are expressed as a chain and a 2D array of beads, respectively.

In performing numerical simulations, the extent of the bottom wall was increased until the calculation result was asymptotically converged (Fig. 4.1.11). To see the convergence, the system configuration was chosen for the largest wire length and the highest inclined angle (24 μm = 160 beads as the wire length and 0.2 radian for the inclined angle), which requires the largest wall matrix. If the calculation converges with this wire's configuration, it will converge with all the other configurations (shorter wires/smaller inclined angles). n_x is the number of beads in the wall, extending perpendicular to the wire's longitudinal direction (x-axis). n_{-y} is the number of beads in the wall, extending in parallel to the wire's longitudinal direction (y-axis) from the wire-wall contact. n_{+y} is the number of beads in the wall, extending in parallel to the wire's longitudinal direction (y-axis) from the point 160 beads (wire length) away from the contact. So, the height of the wall is the sum of n_{-y}, 160 beads as wire length, and n_{+y}. In calculating the realistic system, n_{-y} and n_{+y} were set at 20 and 90, respectively, with which the calculation results converged at any n_x. In increasing n_x, the convergences of the calculated angular rotational diffusivities in both inclined and azimuth directions were confirmed in Fig. 4.1.11. The convergence in D_φ was much slower than that in D_θ and

therefore required a larger matrix. In this work, n_x = 30 is used for caluculating the inclined angular diffusivity, D_θ, and n_x = 75 for calculating the azimuth angular diffusivity, D_φ.

One can come up with the question whether the single layer of the packed beads array is enough to simulate the wall that has assumedly infinite thickness. In other words, can fluids pass through the beads array such that the model is not sufficiently accurate? Regarding this question, the approximation of the bottom wall by a 2D sheet of the arrayed beads was good enough because the beads occupied ~80% of the area of the total bottom wall, as depicted in the drawing below, resulting in the strong correlation with our experimental systems whose diffusivities changed by more than 2 orders. I further confirmed that this ~80% occupancy is enough to achieve realistic simulation. When the distance between beads (*d* in the left figure) is changed, I clearly see the convergence of the calculated rotational diffusivity as *d* moves closer to *2r*, the diameter of beads, as shown in the right of Fig. 4.1.12. This result confirms that approximation of the beads' assembly is valid to represent a monolithic plate. Note that due to the very low Reynolds number, even a more sparse bead placement on the bottom induces strong friction and prevents the fluid from penetrating the bottom (in the model). This has already been shown in various setups.

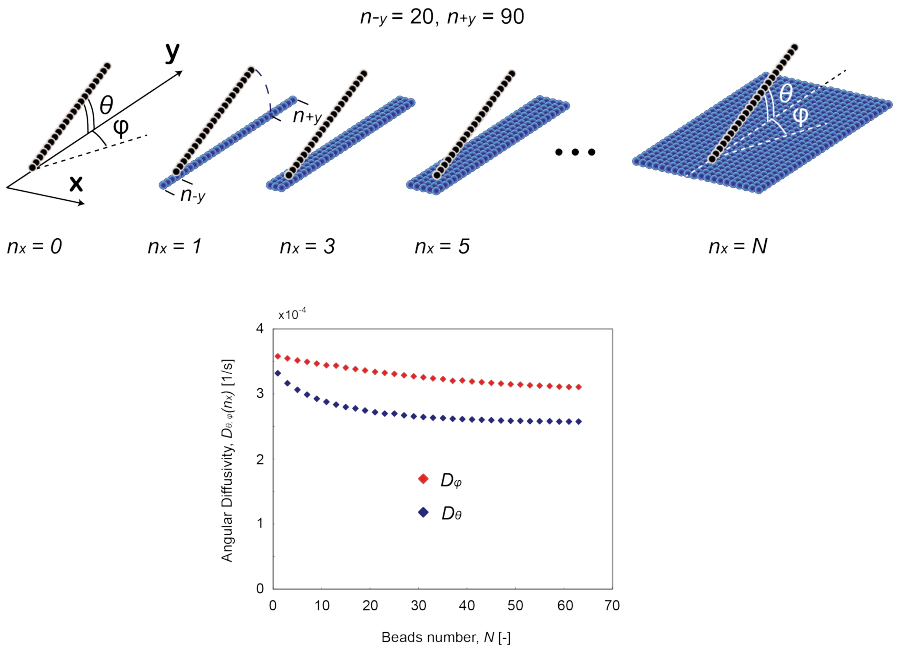

Figure 4.1.11 Convergence of modeling result made by extending the bottom wall dimensions. Larger dimensions were needed to see the convergence in D_φ because the fluid motion induced by the wire's motion in azimuth directions is largely directed to the azimuth directions and the fluid reflection by farther beads affect the calculated rotational diffusivity, making it difficult to calculate in terms of computer resources.

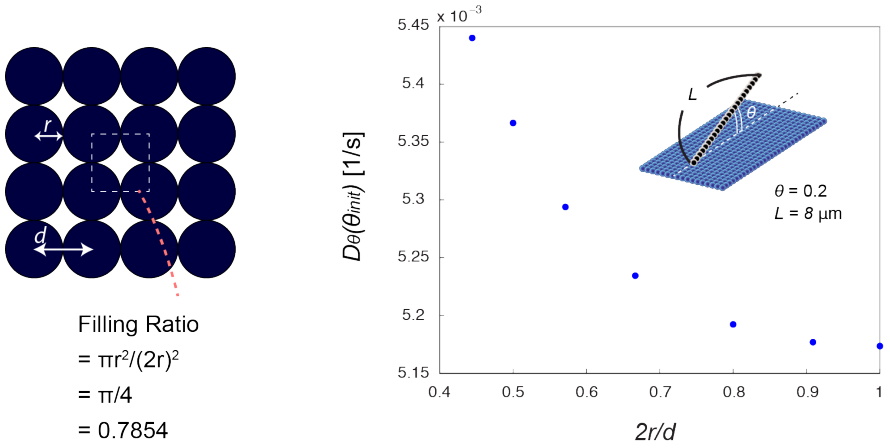

Figure 4.1.12 Validation of the arrayed beads' approximation for representing the monolithic glass wall. Convergence was confirmed when the distance of the beads became smaller, confirming that the approximation of the wall with the dense beads' array was valid.

4.1.5b Implicit Simulation Results

This string-of-beads–idealization and implicit 3D-simulation approach simplifies the numerical calculation considering only the Stokes drag between the individual beads, which is justified because the solution of the relative velocity includes the effect of the multi-reflected Stokes flow. The model is much more efficient than the molecular dynamic simulation, which is incapable of modeling such large systems. In addition, there is no existing analytical solution for the hydrodynamic interaction between the anisotropic object with a simple wall due to its complexity. The model is first tested by simulating the free rotational angular diffusivity of a thin rod around its center as a chain of beads in 2D space. As shown in Fig. 4.1.13, the numerical results agreed well with a well-established analytical approximation [28]:

$$D_{rot} = \frac{k_B T}{\xi_{rot}} = k_B T \Big/ \pi \mu_w \left[L^3 / \{3\ln(L/d) - 0.5\} \right] \qquad (4.1.15)$$

The model is then extended into 3D space to study the hydrodynamic wall effects by representing the wall as a 2D array of beads and the tethered wire as a chain of beads (Fig. 4.1.10b). By assuming the θ at 0.05 radian, the estimated average from the experiment, both D_θ and D_φ, are plotted in Fig. 4.1.14 as blue and red circles, respectively. The black circles are the numerically calculated free rotational diffusivity of the tethered wire around its end, D_{rot} (without a wall). Inset in Fig. 4.1.14 is the anisotropy in diffusivity, D_θ/D_φ. The result showed good agreement with the experimental results, validating the effective modeling of the hydrodynamic interaction with a wall.

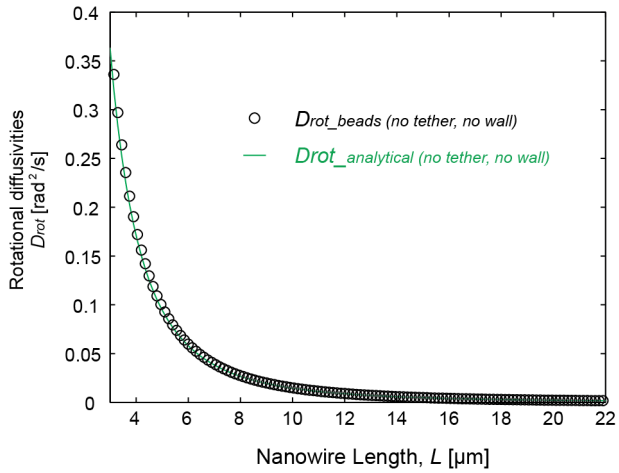

Fig. 4.1.13. Comparison between the analytical approximation and the beads model for the rotational diffusion of the free nanowire *around its center*. Analytically approximated and numerically calculated free rotational diffusivity of the nanowire. The analytical solution for a thin rod is given with equation (4.1.15), plotted as a red curve. The numerical result calculated by the hydrodynamics model is plotted as black circles and shows the good agreement with the analytical curve, proving that our hydrodynamic model correctly considers complex intrinsic HI.

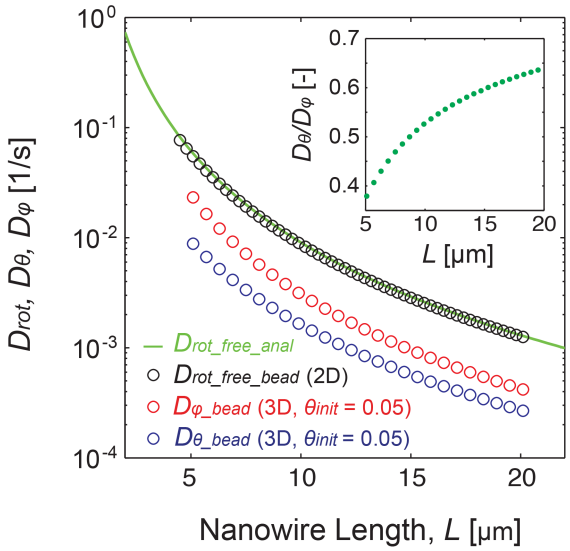

Figure 4.1.13 Comparison between the inclined and azimuth angular rotational diffusion (simulation). The calculated results of the implicit hydrodynamic bead model. The black circles are free rotational diffusivity of the tethered wire around its end, D_{rot}, numerically calculated using our developed bead-model (without a wall). The blue (D_θ) and red (D_φ) circles are also the numerically calculated rotational diffusivities for the tethered wire in the inclined and azimuth directions, respectively (with a wall). The black curve is the analytically approximated rotational diffusivity of the nanowire around one end in bulk, D_θ/D_φ, for comparison (without a wall, see equation in Supporting Fig 6). The inset plots the diffusional anisotropy (D_θ/D_φ). Here, the inclined angle is assumed to be 0.05 radians.

The most important calculation is the one to follow. Because the nanowire experienced different θ during the long time diffusion, I performed a comprehensive calculation of D_θ for a wide range of wire lengths and θ. The free rotational diffusivity of the tethered wire around its end, D_{rot}, was also calculated for normalization. From the calculated

hydrodynamic wall effects visualized in Fig. 4.1.15, we can see the HI become increasingly significant as the wire lengths and/or the θ decrease, which quantitatively correlated strongly with our experimental observations.

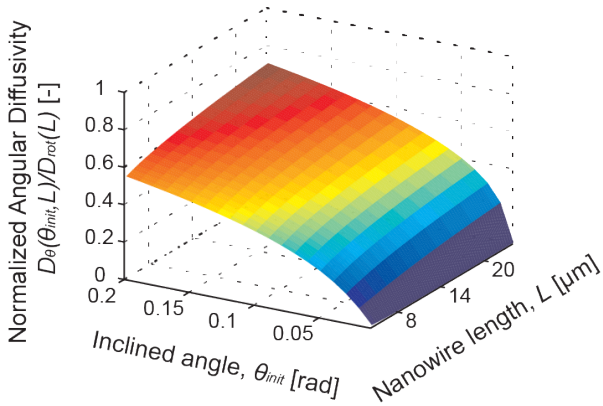

Figure 4.1.15 The inclined angular diffusivity of the tethered wire with different lengths and with different inclined angles, $D_\theta(\theta_{init}, L)$, comprehensively calculated in the developed 3D beads model (normalized by the rotational diffusivity calculated for a free nanowire around one end, $D_{rot}(L)$). The simulation result shows significant hydrodynamic wall effects when the wires are shorter and/or closer to the wall, which quantitatively corresponded strongly with the experimental observations.

In the experiment, I found that the reduction in rotational diffusivity—due to the hydrodynamic interaction with a wall—is more significant for short wires than for long wires. This is because its large volume is very close to the wall. Using the developed numerical model, I calculated the relative fluid velocities (hydrodynamic velocities), which individual beads composing the wire experience, as shown in Fig. 4.1.16. This hydrodynamic velocity is equal to the hydrodynamic drag that individual beads experience when the slender body rotates at a constant speed. It is easily observed that the beads near the tether experience a significant hydrodynamic wall effect and, in total, short wires should experiences larger wall effect.

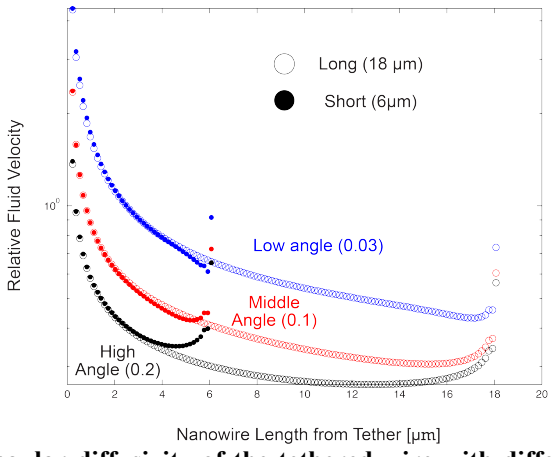

Figure 4.1.16 The inclined angular diffusivity of the tethered wire with different lengths and with different inclined angles, $D_\theta(\theta_{init}, L)$, was comprehensively calculated in the developed 3D beads-model (normalized by the rotational diffusivity).

For a comprehensive analysis of HI, we also calculated D_φ with several sets of the wire lengths and θ. As expected from the results in Fig. 4.1.7b, the effects of HI on D_φ were less significant than that on D_θ (Fig. 4.1.17). Consequently, the anisotropy in the hydrodynamic effect becomes quite significant when θ_{init} approaches zero. It might contribute to the efficient functioning of diffusive motor proteins such as kinesin and *F_1F0*-ATPase beside walls [15, 40, 41]. In general, the observed HI should also affect the near-interface diffusion of anisotropic biological objects, including the cells and filamentous macromolecules [7-16]. Extending our numerical approach to study the 3D motion of semi-flexible objects is straightforward [16] and I thus believe that it can also simulate the near-interface HI in these biophysical systems.

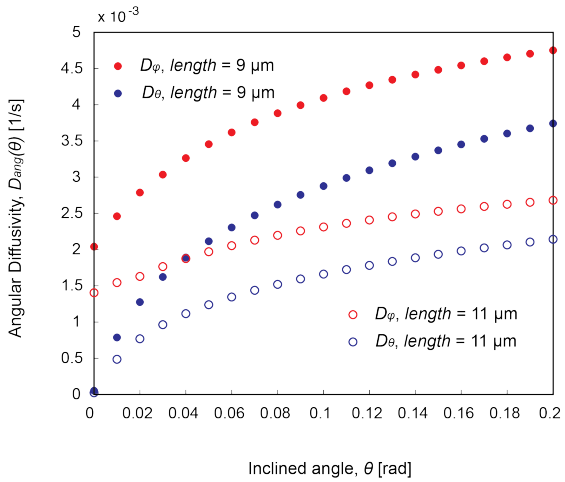

Figure 4.1.17 Comparison between the inclined and azimuth rotational diffusion (simulation). Using the developed hydrodynamics model, I calculated both inclined and azimuth rotational diffusivity of the sample nanowires of 9 μm and 11 μm in length. The hydrodynamic drag by the wall results in a reduction in the diffusivities when the nanowire approaches the wall. As expected from the experiment, the effect was clearly less significant on D_φ, than on D_θ, resulting in the highly anisotropic diffusion of the tethered wires.

4.1.6 Summary and Future Directions

This work developed two new technologies: the Mie resonance-enhanced backscattering interference contrast microscopy and the string-of-beads–based implicit hydrodynamic 3D numerical modeling. These new techniques enable the study of the Brownian motion of tethered nanowires with high spatiotemporal resolutions, offering fundamental insights for understanding the near-wall diffusion of slender particles. These developed technologies revealed anisotropic power-law dependence of the rotational diffusivity on the particle length: the rotational diffusivity follows $L^{-2.5}$ and L^{-3} in the inclined and azimuth directions. Also, these methods enabled both experimental and numerical observation of the angle-dependent rotational diffusion due to the hydrodynamic interaction (HI) with a wall. Finally, I proved the accuracy of our simulation and the significant contribution of the HI via the good agreement of experimental results with the simulation results.

The novel interferometry technique, along with the versatile calculation method, provides a powerful platform for studying interfacial microrheology of various soft condensed matters, including the biological particles near cellular and artificial

membranes [15, 40-42]. For the nanomaterial self-assembly on a substrate, the quantitatively validated string-of-beads model is an efficient tool for optimizing the conditions that potentially reduce the position inaccuracy caused by the thermal fluctuation and hydrodynamic forces [17-20]. In the near future, use of ferromagnetic nanowires will enable active interfacial microrheology and further explore the rich dynamical response of fluids near surfaces [43-45].

References

1. Einstein, A. On the movement of small particles suspended in stationary liquids required by the molecular-kinetic theory of heat. *Ann Physic* (1905).
2. P. Langevin, On the Theory of Brownian Motion", *C. R. Acad. Sci. (Paris)* **146**, 530-533 (**1908**)
3. Lemons, D. S. Paul Langevin's 1908 paper "On the Theory of Brownian Motion, C. R. Acad. Sci. (Paris) 146, 530–533 (1908)]. *Am. J. Phys.* **65,** 1079–1081 (1997).
4. Burger, H. C. & Ornstein, L. S. On the theory of the Brownian motion. *Phys. Rev.,* **36**, 823-841, (1930)
5. Sparreboom, W., van den Berg, A. & Eijkel, J. C. T. Principles and applications of nanofluidic transport. *Nature Nanotechnology* **4,** 713–720 (2009).
6. J.Happel & H. Brenner, Low Reynolds Number Hydrodynamics: With Special Applications to Particulate Media, Springer, (1983).
7. Drescher, K., Dunkel, J., Cisneros, L. H., Ganguly, S. & Goldstein, R. E. Fluid dynamics and noise in bacterial cell-cell and cell-surface scattering. *Proc. Natl. Acad. Sci. U.S.A.* **108,** 10940–10945 (2011).
8. Riedel, I. H., Kruse, K. & Howard, J. A Self-Organized Vortex Array of Hydrodynamically Entrained Sperm Cells. *Science* **309,** 300–303 (2005).
9. Lauga, E., DiLuzio, W. R., Whitesides, G. M. & Stone, H. A. Swimming in Circles: Motion of Bacteria near Solid Boundaries. *Biophysical Journal* **90,** 400–412 (2006).
10. Li, G., Tam, L.-K. & Tang, J. X. Amplified effect of Brownian motion in bacterial near-surface swimming. *Proceedings of the National Academy of Sciences* **105,** 18355–18359 (2008).
11. Brennen, C. & Winet, H. Fluid mechanics of propulsion by cilia and flagella. *Annual Rev. Fluid Mech.* **9,** 339–398 (1977).
12. Aranson, I. S. & Tsimring, L. S. Theory of self-assembly of microtubules and motors. *Phys. Rev. E,* **74,** 031915 (2006).
13. Fakhri, N., MacKintosh, F. C., Lounis, B., Cognet, L. & Pasquali, M. Brownian Motion of Stiff Filaments in a Crowded Environment. *Science* **330,** 1804–1807 (2010).
14. Li, G. & Tang, J. X. Diffusion of actin filaments within a thin layer between two walls. *Phys. Rev. E* (2004).
15. Dodd, T. L., Hammer, D. A., Sangani, A. S. & Koch, D. L. Numerical simulations of the effect of hydrodynamic interactions on diffusivities of integral membrane proteins. *J. Fluid Mech.* **293,** 147 (2006).
16. Chandran, P. L. & Mofrad, M. R. K. Averaged implicit hydrodynamic model of

semiflexible filaments. *Phys. Rev. E* **81,** 031920 (2010).
17. Yu, G., Cao, A. & Lieber, C. M. Large-area blown bubble films of aligned nanowires and carbon nanotubes. *Nature Nanotechnol.* **2**, 372, (2007).
18. Freer, E. M., Grachev, O. & Stumbo, D. P. High-yield self-limiting single-nanowire assembly with dielectrophoresis. *Nature Nanotechnol.* **5,** 525–530 (2010).
19. Huang, Y., Duan, X., Wei, Q. & Lieber, C. M. Directed Assembly of One-Dimensional Nanostructures into Functional Networks. *Science* **291,** 630–633 (2001).
20. Pauzauskie, P. J. *et al.* Optical trapping and integration of semiconductor nanowire assemblies in water. *Nature Materials* **5,** 97–101 (2006).
21. Wang, G. M., Prabhakar, R. & Sevick, E. M. Hydrodynamic mobility of an optically trapped colloidal particle near fluid-fluid interfaces. *Phys. Rev. Lett.* **103,** 248303 (2009).
22. Carbajal-Tinoco, M. D., Lopez-Fernandez, R. & Arauz-Lara, J. L. Asymmetry in colloidal diffusion near a rigid wall. *Phys. Rev. Lett.* **99,** 138303 (2007).
23. Jeney, S., Lukić, B., Kraus, J. A., Franosch, T. & Forró, L. Anisotropic memory effects in confined colloidal diffusion. *Phys. Rev. Lett.* **100,** 240604 (2008).
24. Brenner, H. The slow motion of a sphere through a viscous fluid towards a plane surface. *Chemical Engineering Science* **16,** 242–251 (1961).
25. G. Kasper, Wall correction to the Stokes resistance of arbitrarily shaped particles, *J. Aerosol Sci.* **18**, 457 (1987).
26. Han, Y. *et al.* Brownian Motion of an Ellipsoid. *Science* **314,** 626–630 (2006).
27. Padding, J. T. & Briels, W. J. Translational and rotational friction on a colloidal rod near a wall. *J. Chem. Phys.* **132,** 054511 (2010).
28. Neild, A. *et al.* Translational and rotational coupling in Brownian rods near a solid surface. *Phys. Rev. E* **82,** 041126 (2010).
29. Brenner, H. Rheology of a dilute suspension of axisymmetric Brownian particles. *, Int. J. Multiphase Flow,* **1,** 195–341 (1974).
30. Wiegand, G., Neumaier, K. R. & Sackmann, E. Microinterferometry: Three-Dimensional Reconstruction of Surface Microtopography for Thin-Film and Wetting Studies by Reflection Interference Contrast Microscopy (RICM). *Applied Optics* **37,** 6892–6905 (1998).
31. Limozin, L. & Sengupta, K. Quantitative Reflection Interference Contrast Microscopy (RICM) in Soft Matter and Cell Adhesion. *Chem. Eur. J. of Chem. Phys.* **10,** 2752–2768 (2009).
32. Schilling, J., Sengupta, K., Goennenwein, S., Bausch, A. R. & Sackmann, E. Absolute interfacial distance measurements by dual-wavelength reflection interference contrast microscopy. *Phys. Rev.* **69,** 021901 (2004).
33. H. C. Van De Hulst, in *Light Scattering by Small Particles.* (John Wiler & Sons, Inc., N.Y.: Mineola, N. Y.) (1957).
34. Nikta Fakhria, Dmitri A Tsyboulskic, Laurent Cognetc, R. B. Weismanc, and M. Pasquali, Diameter-dependent bending dynamicsof single-walled carbon nanotubes in liquids, *PNAS*, **106**, 14219 (2009).
35. Sohn, Y.-S. *et al.* Mechanical Properties of Silicon Nanowires. *Nanoscale Res Lett* **5,** 211–216 (2010).

36. Hopcroft, M. A., Nix, W. D. & Kenny, T. W. What is the Young's Modulus of Silicon? *J. Microelectromech. Syst.* **19,** 229–238 (2010).
37. Landau, Lev Davidovich; and Lifshiz, Evgeny Mikhaikivich Statistical Physics. Course of Theoretical Physics **5** (3 ed.). *Oxford: Pergamon Press*, (1980).
38. Li, T., Kheifets, S., Medellin, D. & Raizen, M. G. Measurement of the Instantaneous Velocity of a Brownian Particle. *Science* **328,** 1673–1675 (2010).
39. Carrasco, B. & García de la Torre, J. Hydrodynamic Properties of Rigid Particles: Comparison of Different Modeling and Computational Procedures. *Biophysical Journal* **76,** 3044–3057 (1999).
40. Bieling, P., Telley, I. A., Piehler, J. & Surrey, T. Processive kinesins require loose mechanical coupling for efficient collective motility. *EMBO Rep* **9,** 1121–1127 (2008).
41. Ballmoos, von, C., Wiedenmann, A. & Dimroth, P. Essentials for ATP Synthesis by F_1F_0ATP Synthases. *Annu. Rev. Biochem.* **78,** 649–672 (2009).
42. Wilhelm, C. Out-of-Equilibrium Microrheology inside Living Cells. *Phys. Rev. Lett.* **101,** 028101 (2008).
43. Rovner, J. B., Lapointe, C. P., Reich, D. H. & Leheny, R. L. Anisotropic stokes drag and dynamic lift on cylindrical colloids in a nematic liquid crystal. *Phys. Rev. Lett.* **105,** 228301 (2010).
44. Choi, S. Q., Steltenkamp, S., Zasadzinski, J. A. & Squires, T. M. Active microrheology and simultaneous visualization of sheared phospholipid monolayers, *Nat. Ccommun.* **2**, 312 (2011).
45. Dhar, P., Cao, Y., Fischer, T. M. & Zasadzinski, J. A. Active Interfacial Shear Microrheology of Aging Protein Films. *Phys. Rev. Lett.* **104,** 016001 (2010).

4.2 Axial Plane Optical Microscope

4.2.1 Optical Sectioning Microscopes: Confocal and Light-Sheet Illuminations

The ideal microscope can collect the light photons that come from only the focal plane onto a detector plane. In reality, however, the detector cannot avoid collecting the light from sources outside the focal plane. Therefore, if the sample to observe is too thick, the projected image of the objective's focal plane on the detector suffers from high background noise. To address this issue, there have been significant advances in optical sectioning microscopy to enable taking high-contrast (high signal-to-background ratio) images of the objective lens's focal plane deep within a thick sample. Good performance of the optical sectioning, especially with fluorescence signals and conventionally in z resolution, is of great importance in the field of biological research and biomedical diagnosis because the stack of the high-contrast two-dimensional (2D) images from different focal planes produces the 3D reconstruction of a sample [1].

In fluorescence microscopy, fluorophores outside the focal plane can create background noise in the detector plane if they are illuminated with excitation light. Thus, fluorescence sectioning can be improved with engineered illumination specific to only the focal plane. Among the many techniques currently employed, the most widely used optical sectioning method is a confocal scanning microscope [2-6]. The confocal scanning microscopy utilizes a pinhole at a conjugate focal plane to create the point light source in the sample and utilizes another pinhole to filter out light from sources outside the focal plane to improve optical sectioning (Fig. 4.2.1a). Light sheet fluorescence microscopy, or selective-plane illumination microscopy (SPIM), is a more recently developed optical sectioning microscopy method wherein a slice of an intact fluorescently labeled sample can be imaged with a thin laser light sheet illumination from the side [6-14]. In this method, at least two objective lenses are needed near the sample and are aligned at a 90° angle, one for illumination and another for detection. In other words, only the focal plane of an objective for detection is illuminated, using a laser focused in one direction by another objective for illumination (light-sheet) (Fig. 4.2.1b).

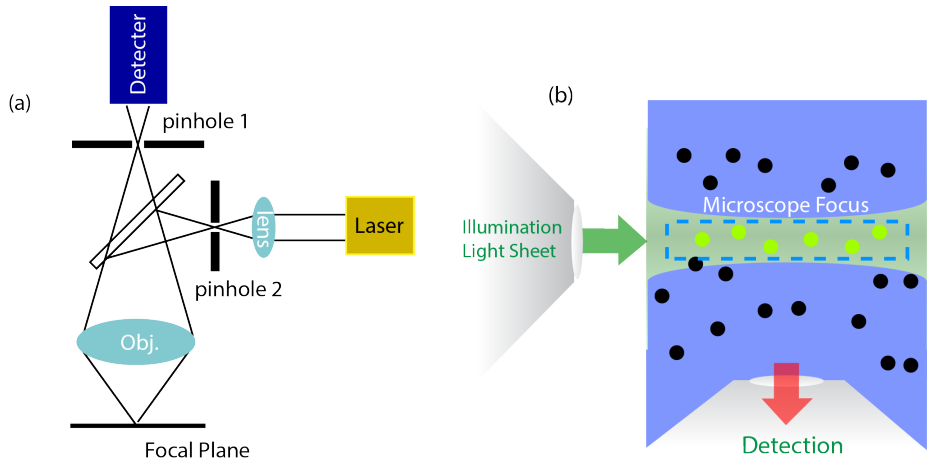

Figure. 4.2.1 Schematic of laser-scanning confocal microscope (a) and selective plane illumination microscope (b).

Compared to the laser scanning confocal microscopy, the SPIM has both advantages and disadvantages. In illumination for the excitation of fluorophores, the confocal microscopy focuses the light from the single objective's direction, which still cannot avoid excitation of fluorophores in the out-of-focus plane and causes background noise and photobleaching there. On the other hand, because SPIM excites only the fluorophores within the light-sheet illumination, it does not cause any background noise or out-of-focus photobleaching. In the collection aspect, although the confocal microscope requires point scanning by mechanically moving the objective and collecting signals by single photon detectors, the SPIM allows wide field image collection on the detector plane in a camera. Consequently, the SPIM allows for faster imaging and reduces total photobleaching of thick samples by orders of magnitude. Due to the afore-mentioned higher single-to-noise ratio, the contrast and resolution of SPIM can exceed even that of confocal microscopy in large samples [6].

On the other hand, a major disadvantage of SPIM, is that it requires two or more objective lenses near the sample at two perpendicular axes, one for illumination and another for signal collection [6-14]. This limits the shape of the samples, the NA of the objectives, and thus the general applications of SPIM. Because two objectives are aligned close to each other, the sample needs to be small enough to be placed in the small space between the objectives. One solution is to reduce the NA of the objectives to have a longer working distance, but doing so is equivalent to scarification of the images' resolution. Also, if the sample is too wide, the light sheet cannot penetrate over the whole section. For example, although SPIM successfully imaged a small fish embryo or brain, it did not image larger animals' tissues, such as centimeter-scale mouse brains, because the light penetration at visible range is limited. Furthermore, a high NA objective is difficult to use in SPIM, especially for light-sheet creation, because such lenses are too large to be aligned to the similarly large NA objective within their small working distance.

4.2.2 Axial Plane Microscope

A wide-field optical microscope typically captures 2D images of samples' cross-sections within the objective's focal (normal) plane (Fig. 4.2.2a) [15]. For some applications such as imaging cortical neurons of a live brain [16] or studying mechanotransduction [17], and mechanical properties of cells [18], however, the main plane of interest is perpendicular to the sample surface and parallel to the objective's optical axis (Fig. 4.2.2b). Currently, such axial plane images can be reconstructed from a series of sliced normal plane images taken by optical methods such as confocal microscopes, which are limited in temporal resolutions [2-6, 20]. In principle, axial plane images can also be obtained by holographic techniques [21-23], but they require coherent light signals and are not applicable to incoherent fluorescent signals, critically limiting their applications in biology.

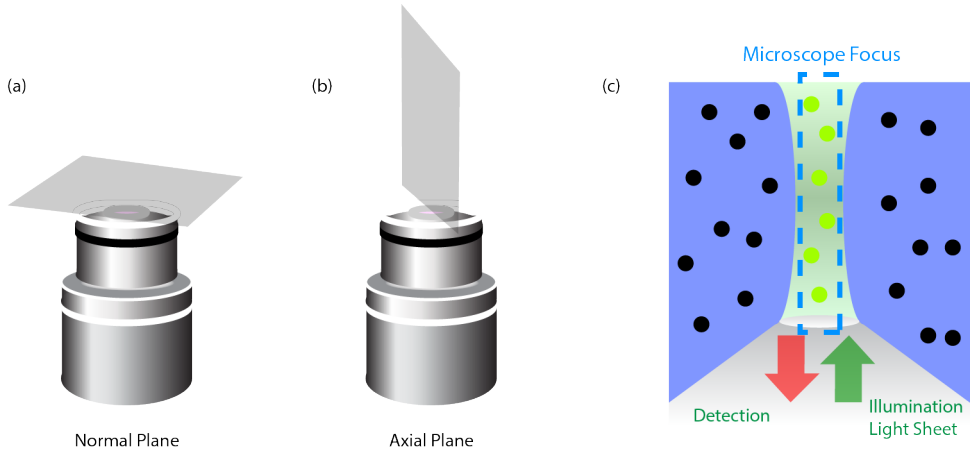

Fig. 4.2.2 Axial Plane Optical Microscope enables the selective plane illumination microscopy with a single lens near the sample. (a) and (b) depict the normal and axial plane defined relative to the optical axis of the imaging objective lens. As shown in (c), the APOM allows the single objective lens to illuminate the light-sheet in the sample and collect the signals to form a axial plane image of the excited fluorophores.

If optically direct imaging of an axial plane in microscopy is possible, it has immediate and highly influential application in SPIM. As shown in Fig. 4.2.2c, the single objective can be used to illuminate the fluorescent sample with a light sheet and then collect the emission from fluorophores within the sheet, directly as an image. Thus, the APOM enables single-lens SPIM and removes the limitations of the conventional SPIM (i.e., the sample shape and the NA of the used objectives).

This work proposes the idea of an axial plane optical microscope (APOM), and the APOM experimentally demonstrates the scan-free imaging of scattering and fluorescent samples. The current APOM setup achieves sub-micrometer resolution imaging over more than 70 μm × 70 μm field of view in the axial plane. The APOM is fully compatible with conventional wide-field microscopes, enabling fast, simultaneous acquisition of orthogonal combination of wide-field images (lateral + axial) of three-dimensional (3D) samples. Furthermore, 3D imaging fluorescent pollens and mouse brain slices using the single-lens SPIM is demonstrated. This single-lens SPIM will become an important breakthrough in a wide range of fields, including 3D tissue imaging, image-based flow cytometry, and *in vivo* single molecule fluorescence studies.

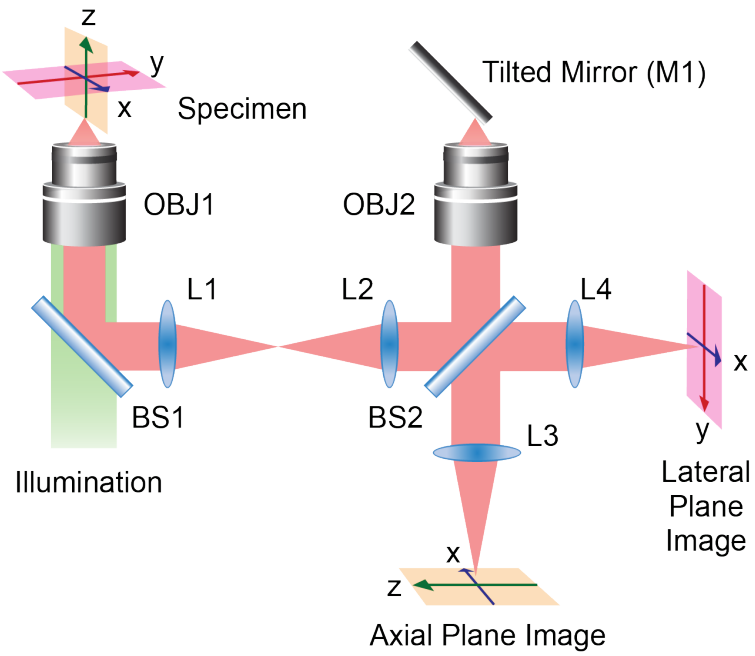

Fig. 4.2.3 Optical setup of the APOM. (a) Schematic of the APOM setup. The APOM contains one objective lens (OBJ1) near the sample for both illumination and signal collection, and a remote objective lens (OBJ2) for forming an aberration-free 3D image around its focal regions. This 3D image is reflected by a mirror (M1) tilted by 45° with respect to the optical axis of OBJ2. Part of the reflected light is recollected by OBJ2 and forms an axial plane image of the sample. The light that transmits through BS2 forms a lateral plane image of the sample. BS1 and BS2 are beam splitters. L1, L2, L3, L4 are achromatic lenses.

As shown in Fig. 4.2.3, one objective lens (OBJ1, 100×, NA=1.4, oil immersion) is used near the sample for both illumination and image collection, and another identical objective lens (OBJ2) is used far away from the sample for forming a 3D optical image above. A 45°-tilted mirror (M1) placed at the focus of the remote OBJ2 transforms the axial cross-section to the lateral cross-section of this remote OBJ2. The axial plane image of the sample is thus formed at the image plane of the remote OBJ2 and collected by a CCD camera (ray tracing simulation of the imaging principle of APOM shown in Fig. 4.2.4 and the effective pupil of APOM is also shown in Fig. 4.2.5). This direct optical imaging requires no scanning or computation, and is thus inherently fast. In principle, the mirror M1 can be placed at any arbitrary angle from 0° to 45°, and be rotated around the optical axis of the remote objective to achieve arbitrary plane imaging. In the current experimental set-up, the pair of identical objective lenses to form the 3D image above OBJ2 without the spherical aberration experienced by optical signals from points outside of the focal plane of the first objective [24-26]. The small working distance of the high NA objective (about 0.13 mm) requires the 45° mirror with clean reflective surface and straight edge. This high quality mirror can be created by coating aluminum on cleaved silicon wafers with an atomically straight edge. Aluminum is superior to other materials such as silver and gold since it is more resistant to oxidation than silver and better optical (reflective) property than gold. In more detail, the two identical objectives used in the optical setup utilizes are Zeiss Plan-Apochromat 100× NA 1.4 oil immersion objective lenses. The tube lenses (L1, L2, L3, L4) are f=150 mm doublet achromatic lenses, BS1 is a 90% reflection beam splitter, and BS2 is a 50% beam splitter. The tilted mirror M1 is a

cleaved silicon wafer coated by about 150 nm of aluminum. The cleaved silicon wafer is used because it has a very straight and shape edge, so providing the ideal mirror placed with an angle at 45 degree as respected to the optical axis of the OBJ2. This tilted mirror converts the image in the axial plane of OBJ2 to an image in the normal plane of OBJ2.

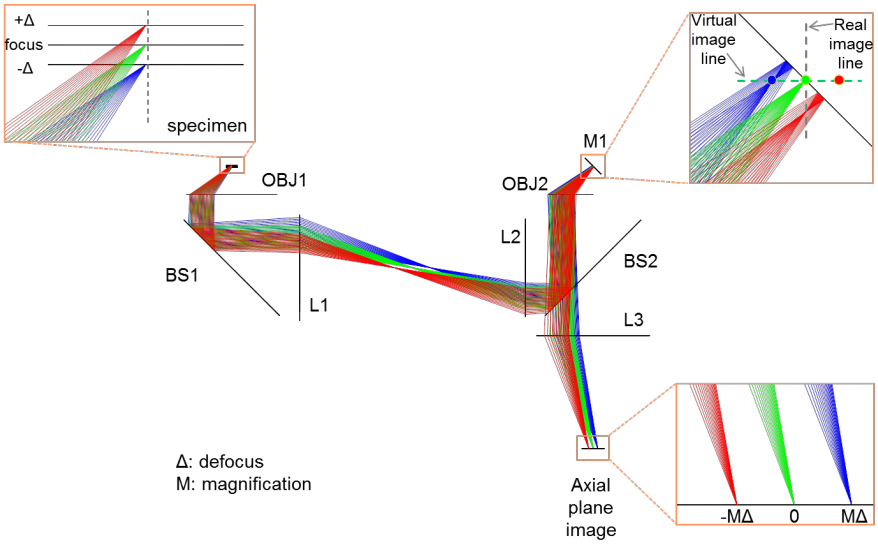

Fig. 4.2.4 The ray tracing simulation by Zemax demonstrates the principle of APOM. Three object points placed on the optical axis of the objective lens (OBJ1) near the sample are imaged to the lateral plane of the detector. OBJ1 and OBJ2 are identical objective lenses. M1 is a mirror tilted by 45° with respect to the optical axis of OBJ2. BS1 and BS2 are beam splitters. L1, L2, L3 are lenses with the same focal length. The separation between the object points (Δ) is magnified by a factor *M*, which is the ratio of the focal length of L3 over the focal length of OBJ1. In the simulation, all optical components are assumed to be aberration free. The back focal point of OBJ1 overlaps with the focal point of L1; the focal point of L1 overlaps with the focal point of L2; and the focal points of L2 and L3 overlap with the back focal point of OBJ2. As shown in the inset, the tilted mirror converts the image in the axial plane of OBJ2 to an image in the lateral plane of OBJ2.

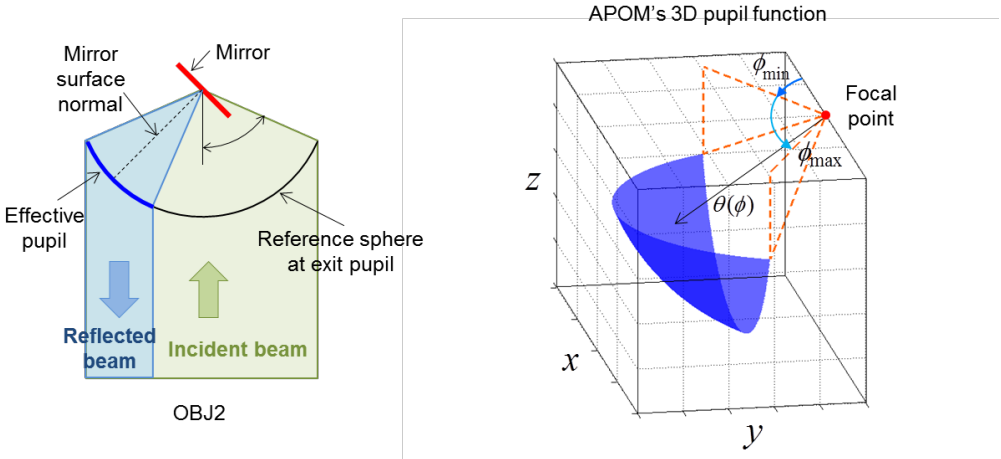

Fig. 4.2.5 Effective pupil of APOM, The left subfigure shows a 2D schematic diagram of the effective pupil in OBJ2 due to signal loss at the 45º mirror. The half-cone angle of the objective lens for signal collection must be greater than 45 degree, corresponding to 0.71 NA in air and 1.07 NA in a n=1.52 oil. The classical scalar diffraction theory is inaccurate in this high NA regime and thus we used the vector

diffraction theory that properly deals with high aperture systems. An effective 3D pupil function in APOM (NA = 1.4, n = 1.52) is first determined by considering the reflected beam path from the tilted mirror back to the exit pupil. The right subfigure shows the 3D effective pupil area of APOM. This is used to numerically estimate the intensity PSF of APOM.

4.2.3 Proof-of-Concept Imaging and Characterization of Resolutions

The APOM enables direct high-resolution axial plane imaging of a sample over a large field of view (Fig. 4.2.6). To understand the resolution limit of APOM, the intensity point spread function (PSF) of APOM is calculated with a vector diffraction theory [24, 25] that treats a high NA optical system accurately (Fig. 4.2.6a). For comparison, the PSF of a conventional microscope along the z-axis is also calculated, although the conventional microscope cannot image the axial plane directly. The calculated full-width at half-maximum (FWHM) of the PSF of APOM in the axial direction is similar to that of a conventional microscope in the axial direction for high NA objectives as shown in Fig. 4.2.7. For the NA of both objectives of 1.4, which is used in the current setup, the full-width at half-maximum (FWHM) of the PSF of APOM is 641 nm along the z-axis and 255 nm along the x-axis (Fig. 4.2.6a) for the wavelength of 546 nm. The experimentally measured FWHM of a gold nanoparticle of 150 nm diameter is about 770 nm along the z-axis, agreeing with the vector diffraction theory (Fig. 4.2.6b and Fig. 4.2.6c). The field of view of APOM is limited by how much the objective OBJ2 can cancel the aberrations caused by objective OBJ1. To study this field of view, a test sample with a nano-hole array with a period of 7 μm perforated in a gold film (Fig. 4.2.6d) is fabricated and imaged. The nano-hole array is placed in the axial plane of the 100× objective OBJ1 using the triangular prism under a wide-field illumination. The illumination light is from a tungsten lamp as shown in Fig. 4.2.3. Fig. 4.2.6e shows the image of 70 μm × 70 μm nano-hole array well-resolved by the APOM with negligible distortions over the entire array, confirming that APOM is well suited to directly image the axial cross-section of large samples. The axial field of view of APOM is much larger than the depth-of-focus of the identical objective used in conventional microscopy, typically less than 1 mm. Further improvement is feasible with phase correction elements such a spatial light modulator.

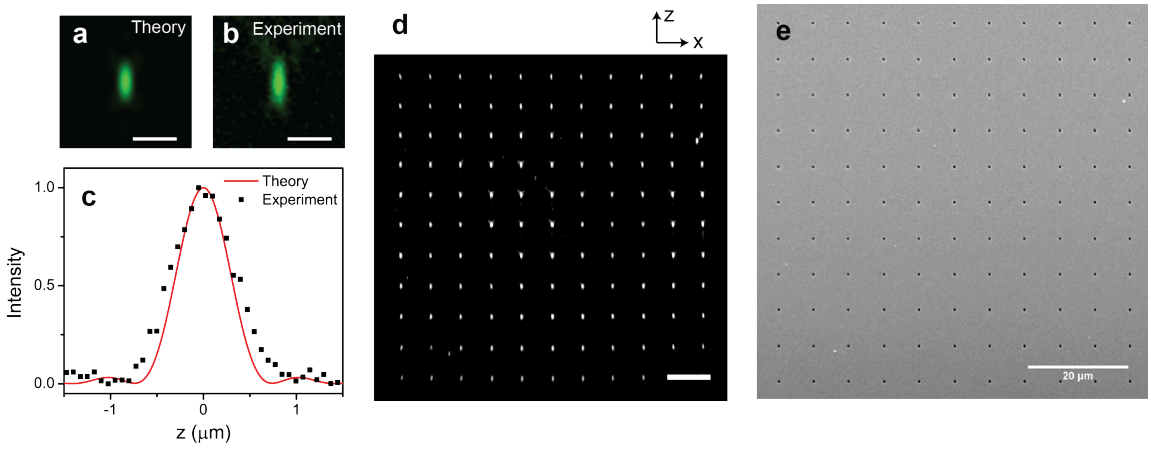

Fig. 4.2.6 Proof-of-concept of APOM demonstration (a) The x-z section of the calculated intensity point spread function (PSF) of the axial plane image when NA=1.4, oil immersion (n=1.52) objectives are used. The optical signal from the specimen is assumed to be unpolarized light with a wavelength of 546 nm. (b) Measured axial plane image of a 150 nm diameter gold nanoparticle placed near the focus of OBJ1. (c)

Profiles of the PSF in the axial direction. The black squares are measured profile of a 150 nm gold nanoparticle in the axial direction, while the red curve is the theoretical profile of the PSF. (d) The axial plane optical image of a 70 μm × 70 μm nano-hole array with a period of 7 μm. The nano-hole array is placed parallel to the optical axis of OB1. Wide-field light from a tungsten lamp is used for the illumination. (e) A SEM image of the nano-hole array used for calibration of the APOM. The period of the array is 7 μm, and the diameter of each hole is 500 nm. The nano-hole array is fabricated by a focused ion beam (FIB) on a 150 nm gold film deposited on a glass coverslip. The small defects (bright spots) near the right top corner and the left bottom corner of the nano-hole array are also visible in the optical image taken by APOM (main text Fig. 1e). In the imaging experiment, the fabricated sample was aligned to be parallel to the optical axis of the objective lens OBJ1, and also be parallel to the edge of the titled mirror M1. The sample was placed in the index-matched oil of the oil-immersion objective lens for imaging. The nano-hole array was fabricated and used for demonstrating the distortion-free large-scale axial plane imaging.
The scale bars in (b) and (c) are 1 μm, and the one in (e) is 10 μm.

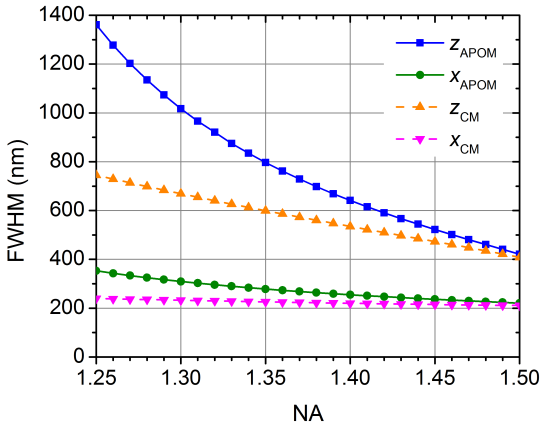

Fig. 4.2.7 Calculated FWHM of point spread functions. Calculated FWHM of the PSF of APOM and a conventional wide-field microscope (CM) along the *x* and *z* axes as a function of the NA of objective lenses for the wavelength of 546 nm. Note that a CM cannot image the axial plane directly. We calculate the FWHM of the PSF of a CM for comparison only. The PSF is not symmetric along the *x* and *z* axes for both APOM and CM's. The resolution of APOM approaches that of CM for high NA objective lenses.To predict theoretical intensity point spread function (PSF) of APOM for an unpolarized point object (λ = 546 nm), multiple double integrals consisting of the vector Debye integral [16, 17] over the derived effective 3D pupil area, is numerically evaluated in MATLAB. For such a numerical simulation, it is assumed that the objective lens satisfies the Abbe's sine condition and the whole system is aberration-free.

4.2.4 Demonstration of 3D Imaging of Biological Samples

For thick fluorescent biological samples, the APOM naturally enables selective-plane illumination microscopy (SPIM) [6-14] with a single objective lens near the sample, enabling axial plane fluorescence imaging with high contrast and throughput (Fig. 2). Here I would restate that, despite its aforementioned advantages over the scanning confocal microscopy, the configuration of closely configured objectives has limited the size of the samples, NA of the objectives and thus its general applications. For example, it has been hard to apply SPIM for imaging large mouse brains and potentially for endoscopic purposes. In contrast, the APOM uses only single high NA objective lens near the sample for both selective plane illumination and image collection. As shown in Fig. 4.2.8a, a thin light sheet is illuminated parallel to the optical axis of the objective lens. In this work, the light sheet is a 532 nm laser beam with thickness ~2 μm. The light sheet is generated by passing a laser through a pair of cylindrical lenses (f= 15mm and f=

200mm). A thin slot was also utilized to further reduce the thickness of the light sheet. As a demonstration, this APOM with the light-sheet illumination is applied to imaging autofluorescent pine pollens (Fig. 4.2.8b). The pollens are intact samples prepared for conventional wide-field microscopes, which embedded in a polymer (purchased from Carolina Biological Supply Inc. (Burlington, USA)). Fig. 4.2.8b is a lateral plane epi-fluorescence image of the pine pollen under wide-field illumination, resulting in low contrast due to the background fluorescence from out-of-focus. The illumination light for Epi fluorescence microscopy is from a mercury lamp for the normal planes images of fluorescent pollens. For fluorescent imaging, a long pass dichroic beam splitter and a band pass filter is placed in front of the camera to block the illumination light while letting the fluorescent signal pass through. The camera used for taking the fluorescent images is a Luca EMCCD camera from Andor. In the case of the APMM the axial plane images (Fig. 4.2.8c-e) shows very high contrast. The shell and hollow structures of the pollen with feature size ~ 1 μm are clearly imaged.

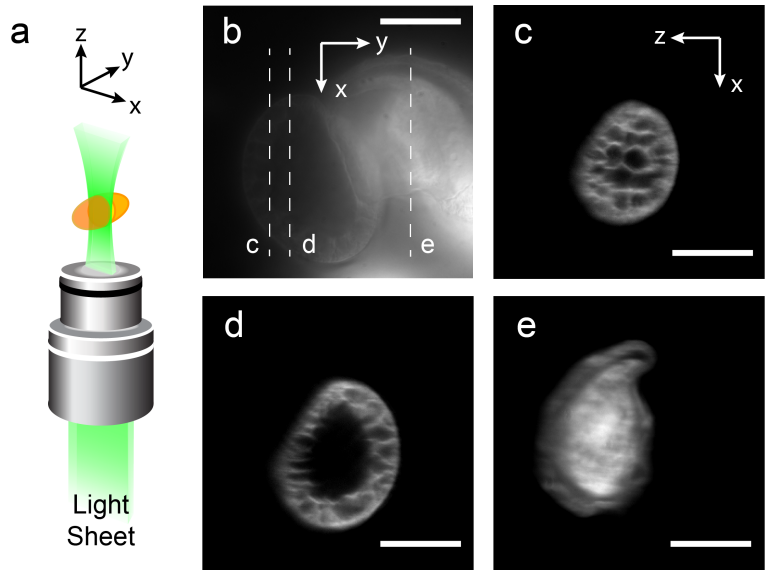

Fig 4.2.8. Lateral and axial plane autofluorescence images of a pollen taken by the APOM. (a) For high-contrast axial plane imaging, the sample is illuminated by a thin laser sheet through the same objective lens (OBJ1) used for image collection. The laser sheet is generated by a pair of cylindrical lenses placed before the objective lens. The width of the laser sheet is about 2 μm. (b) A lateral plane image of a pollen, taken by a wide-field illumination using a mercury lamp. (c), (d), (e) Axial plane images of three different cross-sections of the pollen as labeled in (b). The axial plane images have much higher contrast and better resolved features than the normal plane image because of the optical sectioning by light-sheet illumination. The scale bars are 20 μm.

Because APOM uses only single objective near the sample for SPIM, it requires no special sample preparation and is thus particularly suitable for imaging the structures along depth beneath the surface of large samples, for example, the cerebral cortex of living mammal brains [27]. As a demonstration, the single lens SPIM is used to image fluorescently labeled centimeter-scale mouse brain slices (Fig. 4.2.10a), where the conventional SPIM with multiple objectives installed near the sample [6-14] is very difficult to apply. Fig. 4.2.10b shows its lateral epi-fluorescence image, and Fig. 4.2.10c and Fig. 4.2.10d are high-contrast axial plane fluorescence images of the same brain slice with light-sheet illumination. Here light sheet illumination is applied perpendicular to the

image plane of Fig. 4.2.10a. Again, the axial plane images shows clearly higher contrast and better-resolved features much better than the lateral image because of optical sectioning property. Moreover, only by scanning the sample along the *y*-axis, a series of axial plane images is taken and easily stacked together to create a 3D image efficiently. For stacking, open source software imgej was utilized. Fig. 4.2.10e and Fig. 4.2.10f are the reconstructed 3D fluorescence image of two different mouse brain slices with different fluorescence labeling, which express dense and sparse brain structures, respectively [28, 29]. Different from laser scanning confocal microscopy, the APOM directly obtains 2D axial plane image without scanning, and a 3D image by scanning along only one direction, thus achieving less damage and higher contrast while avoiding the limitation in the sample size, NA of the objectives. In this brain imaging demonstrations, two kinds of fluorescently labeled brain sections shown in Fig. 4.2.10 were gifted by Dr. Kazunari Miyamichi and Dr. Hongfeng Gao, respectively. A sample shown in Fig. 4.2.10b-e is a brain slices with ~30 μm thickness, prepared from a Thy1-GCaMP3 mouse. The sample cells genetically expressed GCaMP3 proteins are immunostained using GFP antibodies conjugated with Cy3. The other sample shown in Fig. 4.2.10f is another brain slices with ~60 μm thickness from a transgenic mouse and labeled with td-Tomato. The APOM images axial cross-sections of the sample directly. To reconstruct a 3D image, the brain section was moved along *y*-axis in step of 0.5 μm by a motorized translation stage. The series of axial plane images are then stacked together to generate the 3D image.

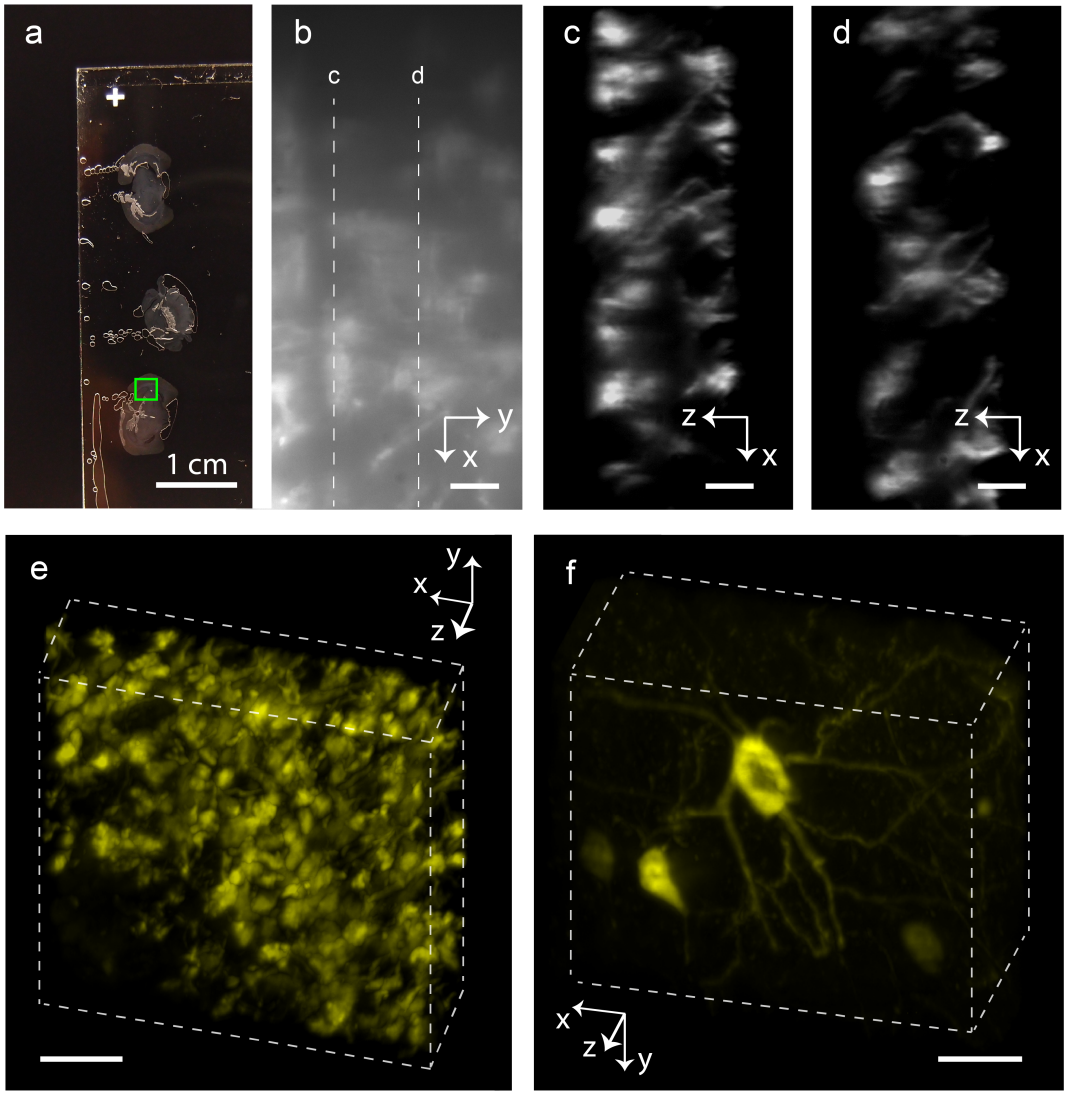

Fig. 4.2.9. Fluorescence imaging of large mouse brain sections by APOM with selective plane illumination. (a) A picture of the glass slide with centimeter-scale mouse brain sections embedded in a polymer whose optical index is matched for the objective lens. No special sample preparation is required for APOM. (b) A normal plane image of the brain slice in the region as labeled by a green square in (a). Axial plane images of two different cross-sections of the brain slice as labeled in (b) are shown in (c) and (d). (e) and (f) are two 3D fluorescent images of mouse brain sections obtained by stacking series of axial plane images together. (e) shows a dense regime while (f) shows a more sparsely stained one. The scale bars are 10 μm in (b-d) and 20 μm in (e-f), respectively.

In addition, I examined the possible distortion in the PSF induced by scattering media such as biological tissues. In the experiment (Fig. 4.1.10a), green fluorescence beads with 200 nm diameter were placed on the previously mentioned brain sections. The index-matched oil was placed on the brain section to minimize the index mismatch between the brain section's optical index and the oil. In this configuration, the light sheet that had passed through the brain section excited the beads, and its emission was collected after it passed through the same section. Despite the remaining mismatch in the

optical index, a relatively good axial resolution of 1.19 μm was achieved in the PSF of the beads as shown in Fig. 4.2.10b, confirming the robustness of APOM.

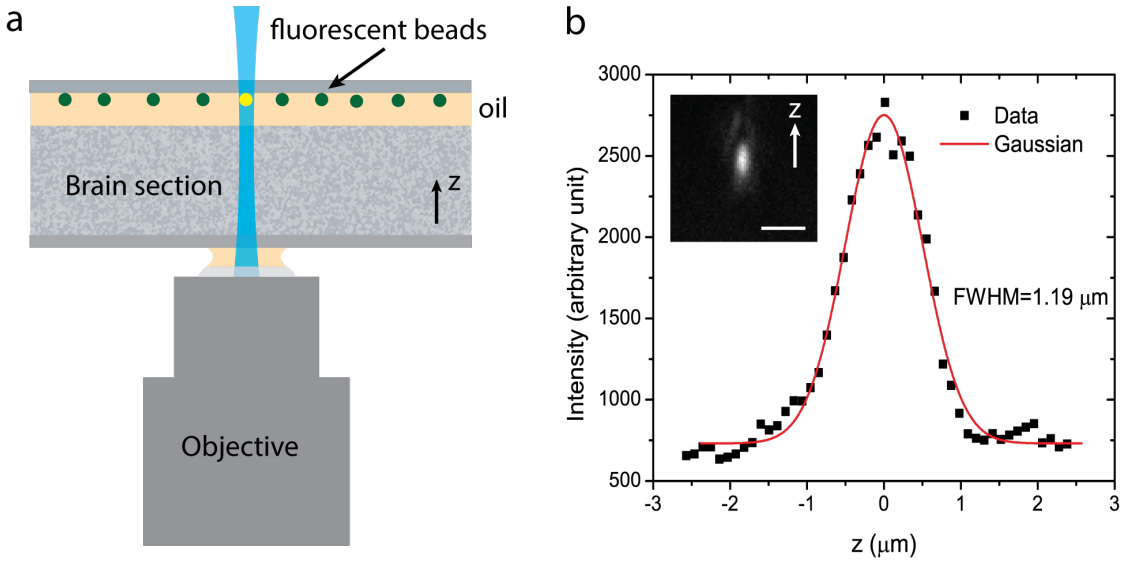

Figure 4.2.10. **Profile of a fluorescent bead after a 75 μm-thick brain slice.** When APOM is used to image thick biological samples, the resolution may degrade due to the mismatch in the refractive index and the light scattering in the biological sample. The profile of a 200-nm (in diameter) green fluorescent bead on top of a 75 μm thick brain section is measured. The fluorescent beads were placed on the surface of a glass cover slip on the brain section, where immersion oil was placed on top of the brain slice to make sure there was no air gap between the brain section and the fluorescent bead **(a).** The measured FWHM of the bead is about 1.19 μm in the axial direction **(b).** This shows that we can obtain high-resolution images of thick biological samples with APOM.

4.2.5. Summary and Future Directions

This section showed the successful development of a novel microscopy, APOM, which is capable of directly imaging the axial plane cross-sections of various 3D samples with no scanning. With a laser sheet illumination through an objective near the sample, the APOM enables fast, high-contrast, and convenient 3D imaging of thick biological samples such as pollens and brain slices, as demonstrated in this work. Again, in this configuration, only one high NA objective near the sample can work for both illumination and detection. The axial plane image can be acquired with negligible distortion over a large field of view (> 70μm × 70 μm), which is much larger than the depth of focus in conventional optical microscopy. The single-lens SPIM enabled with APOM is particularly important because it solves the biggest disadvantage of conventional SPIMs over the established laser scanning confocal microscopy for the 3D imaging: it requires no special sample preparation or limit for the NA of the objective lens used (see Fig. 4.2.12). This breakthrough sheds new light on the general microscopy fields and opens a new avenue for many exciting biological applications such as direct imaging of a living brain from its surface—or potentially inside by endoscopes. In addition, the light sheet from the single high NA objective lens can be thinned down further to reduce the excitation volume and consequently increase signal-to-background ratio, which enables fast and convenient imaging of single fluorescent molecules [30-32].

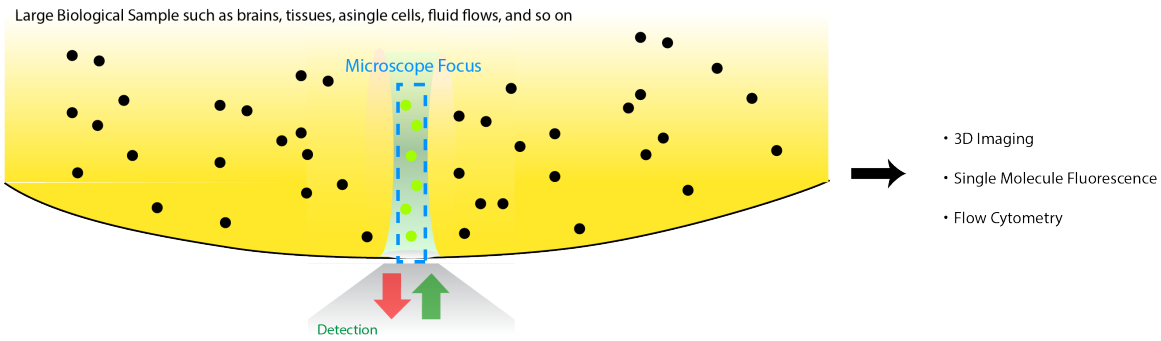

Fig. 4.2.11. Fluorescence imaging of large mouse brain sections by APOM with selective plane illumination.

Finally, it is possible to further improve the APOM in several ways. The simplest way to increase axial resolution is to replace the currently used objective lenses with larger NA lens. Such objective lenses, with 1.49 NA, are commercially available and should improve the axial resolution of APOM to about 450 nm for the wavelength of 546nm (Fig. 4.2.8). The field of view can be enlarged to about 200μm × 200 μm without decreasing the resolution by using commercially available 40× and 1.4 NA objectives and can be further improved by phase correction with spatial light modulation. In addition, the tilted mirror can be rotatable to achieve arbitrary plane imaging [33].

References

1. Conchello, J.-A. & Lichtman, J. W. Optical sectioning microscopy. *Nat Meth* **2,** 920–931 (2005).
2. Pawley, J., Handbook of Biological Confocal Microscopy, *Springer; 3rd edition* (August 10, 2006)
3. Rajadhyaksha, M., Grossman, M., Esterowitz, D., Webb, R. H. & Anderson, R. R. In vivo confocal scanning laser microscopy of human skin: melanin provides strong contrast. *J. Invest. Dermatol.* **104,** 946–952 (1995).
4. Wilson T, Confocal microscopy. *Academic Press: London,* (1990).
5. Shotton, D. M. Confocal scanning optical microscopy and its applications for biological specimens. *Journal of Cell Science* (1989).
6. Huisken, J. & Stainier, D. Y. R. Selective plane illumination microscopy techniques in developmental biology. *Development* **136,** 1963–1975 (2009).
7. Tomer, R., Khairy, K., Amat, F. & Keller, P. J. Quantitative high-speed imaging of entire developing embryos with simultaneous multiview light-sheet microscopy. *Nat Meth* **9,** 755–763 (2012).
8. Cella Zanacchi, F. *et al.* Live-cell 3D super-resolution imaging in thick biological samples. *Nat Meth* **8,** 1047–1049 (2011).
9. Verveer, P. J. *et al.* High-resolution three-dimensional imaging of large specimens with light sheet–based microscopy. *Nat Meth* (2007). doi:10.1038/nmeth1017
10. Ahrens, M. B., Orger, M. B., Robson, D. N., Li, J. M. & Keller, P. J. Whole-brain functional imaging at cellular resolution using light-sheet microscopy. *Nat Meth* **10,** 413–420 (2013).
11. Huisken, J. Optical Sectioning Deep Inside Live Embryos by Selective Plane

Illumination Microscopy. *Science* **305,** 1007–1009 (2004).
12. Dodt, H.-U. *et al.* Ultramicroscopy: three-dimensional visualization of neuronal networks in the whole mouse brain. *Nat Meth* **4,** 331–336 (2007).
13. Truong, T. V., Supatto, W., Koos, D. S., Choi, J. M. & Fraser, S. E. Deep and fast live imaging with two-photon scanned light-sheet microscopy. *Nat Meth* **8,** 757–760 (2011).
14. Mertz, J. Optical sectioning microscopy with planar or structured illumination. *Nat Meth* **8,** 811–819 (2011).
15. Abbe, E., "On the Mode of Vision with Objectives of Wide Aperture", *J. of the Royal Microscopical Society*, **4**, 20-26 (1884).
16. Murayama, M., Pérez-Garci, E., Nevian, T., Bock, T., Senn, W. & Larkum, M. E. Dendritic encoding of sensory stimuli controlled by deep cortical interneurons, *Nature* **457**, 1137-1141 (2009)
17. Wang, N., Butler, J. P., Ingber, D. E., Mechanotransduction across the cell surface and through the cytoskeleton, Science, **260**, 1124 (1993)
18. Ingber, D. E., Cellular mechanotransduction: putting all the pieces together again, The FASEB Journal, **20**, 811 (2006)
19. Chaudhuri, O., Parekh, S. H., Lam, W. A., & Fletcher, D. A. Combined atomic force microscopy and side-view optical imaging for mechanical studies of cells, *Nat. Methods* **6**, 383 - 387 (2009)
20. Botcherby, E. J., Booth, M. J., Juškaitis, R. & Wilson, T. "Real-time slit scanning microscopy in the meridional plane", Opt. Lett. **34**, 1504-1506 (2009).
21. Zhang, T., & Yamaguchi, I. "Three-dimensional microscopy with phase-shifting digital holography", *Opt. Lett.*, **23**, 1221-1223 (1998)
22. Charrière, F. and et al. "Living specimen tomography by digital holographic microscopy: morphometry of testate amoeba", *Opt. Express*, **14**, 7005-7013 (2006)
23. Sung, Y. and et al. "Optical diffraction tomography for high resolution live cell imaging", *Opt. Express*, **17**, 266-277 (2009).
24. Botcherby, E. J., Juškaitis, R., Booth, M. J., and Wilson, T., Aberration-free optical refocusing in high numerical aperture microscopy, Opt. Lett., **32**, 2007-2009 (2007).
25. Botcherbya, E. J., et al. Aberration-free three-dimensional multiphoton imaging of neuronal activity at kHz rates", PNAS, **109**, 2919-2924 (2012)
26. Anselmia, F., Ventalona, C., Bèguea, A., Ogden, D., and Emiliania, V., Three-dimensional imaging and photostimulation by remote-focusing and holographic light patterning, PNAS, **108**, 19504 (2011).
27. Osten, P. & Margrie, T. W., Mapping brain circuitry with a light microscope, *Nature Methods* **10**, 515–523 (2013)
28. Miyamichi, K. *et al*. Cortical representations of olfactory input by trans-synaptic tracing. *Nature* **472**, 191–196 (2011)
29. Chen, Q. *et al*. Imaging Neural Activity Using Thy1-GCaMP Transgenic Mice, *Neuron* **76**, 297–308, (2012).
30. Gebhardt, J. C. M. *et al.* Single-molecule imaging of transcription factor binding to DNA in live mammalian cells. *Nat. Meth.* **10**, 421–426 (2013).
31. Li, G.-W. & Xie, X. S. Central dogma at the single-molecule level in living cells.

Nature **475,** 308–315 (2011).
32. Ritter, J. G., Veith, R., Veenendaal, A., Siebrasse, J. P. & Kubitscheck, U. Light sheet microscopy for single molecule tracking in living tissue. *PLoS ONE* **5,** e11639 (2010).
33. Dunsby, C. Optically sectioned imaging by oblique plane microscopy. *Opt. Express* **16,** 20306–20316 (2008).

4.3 Optofluidic 3D Printing

This final idea of optofluidic 3D printing shares the optical path uniquely developed for the axial plane optical microscope. This work is thus an extension of the work of bio-imaging introduced in Section 4.2 but is separately introduced in this section because it is of great importance in a different field.

4.3.1 Optical Lithography for 3D Material Synthesis

Thanks to the high controllability of light, lithography technologies formed the basis of micro- and nanotechnology evolutions. One of the driving forces for current technological developments is to create 3D structures at higher resolution and higher throughput. The so-called 3D printer is now expected to create a personalized manufacturing industry as a trend in industry because individuals outside companies can design and make products at home due to the cheapness of the printers [1]. More traditionally, optical lithography-based 3D printing has been called stereolithography (SL) [2-11], and its evolved version is the two-photon lithography (2PL) [12-20].

SL is an additive manufacturing process: (1) SL utilizes UV-curable photoresist, and a UV laser fabricates layers of the various parts, one at a time. For each layer, the laser beam exposes a cross-section of the parts' pattern on the surface of the liquid resin, curing and solidifying it into the exposed pattern; (2) the SL's projection system moves up by a distance equal to the thickness of a single layer, typically tens to hundreds of micrometers; (3) Then, a fresh photoresist layer is added. By repeating processes (1)–(3), 3D structures are created. After it is built, the parts are immersed in a chemical bath to be cleaned and further UV-solidified. Meanwhile, 2PL essentially applies the nonlinear photon absorption process to the SL. The reason SL requires the additive process is the issue of background (un-needed photo-polymerization outside the focus plane). Because typical SLs utilize relatively low NA lenses, the background issue is severe. In contrast, the nonlinear two-photon absorption process can happen only when the light is most intensified at the exact focus and thus is quite free from the background issue. As a result, the 2PL can achieve direct laser writing at very high resolution in the photoresist without the additive process.

Despite the solid advance of both SL and 2PL, the intrinsic disadvantage of these batch-based technologies is their limited throughput. The scalability of products is physically defined with the batch size, limiting their application in making more or larger structures. The missing structure includes infinitely long fibers that have great potential application in photonics and biomedicine, or a massive number of microparticles for biomedical diagnosis.

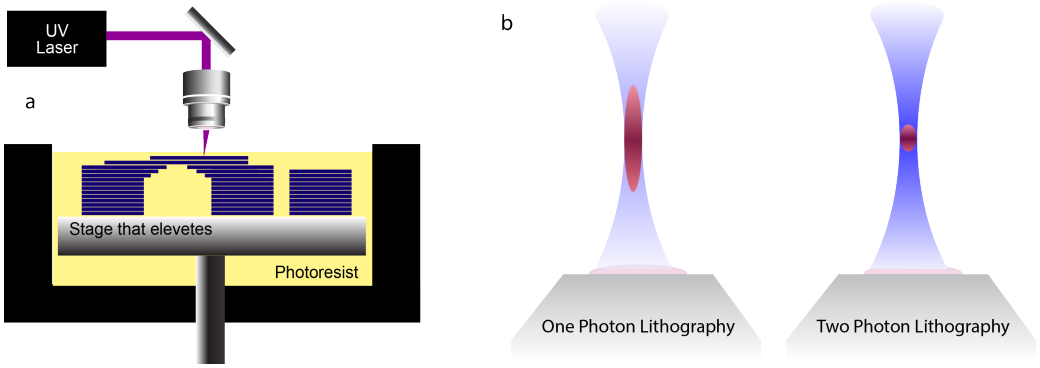

Figure 4.3.1 Stereolithography (a) and comparison of one-photon and two-photon lithography (b). Two-photon absorption dramatically reduces the volume where photochemical reaction occurs, improving the resolution of photolithography and removing the layer-additive process used in stereolithography.

4.3.2 Optofluidic Lithography

Optofluidic lithography (OL) was first demonstrated by P. Doyle's group in 2007 [21] and is a technique for optically synthesizing free-floating microstructures in microfluidic channels [22-25]. Projected 2D light patterns through an objective lens below the fluidic channel polymerizes the photoresist inside the channel, while oxygen provided through the porous PDMS walls prohibits the adhesion of particles to the wall.

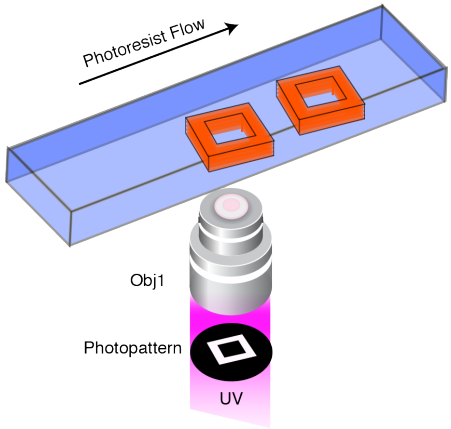

Figure 4.3.2 2D Optofluidic lithography. In this method, the 2D light pattern projected and demagnified with an objective lens with relatively small NA photo-polymerizes the photoresist flowing in the microfluidic channels, creating the microparticles with defined structures according to the 2D light pattern. After polymerization, the microfluidic flows sweep away the synthesized structures and the next light pattern will create the next set of microstructures.

Compared to the techniques introduced in Section 4.3.1, this OL is advantageous because it is free from the batch-based process. However, its application is still limited for several reasons: (1) the shape of structures that can be fabricated by OL is limited in 2D; (2) materials that can be used for channel walls are limited because the channel wall facing the polymerized wall needs to inhibit the polymerization at contact. Some solvents are not compatible with the PDMS; thus, materials different from PDMS but having sufficient porosity to provide oxygen are being researched. For the first issue, although a numerous number of efforts were made to achieve 3D optofluidic printing, none could create arbitrary shaped particles [26-29]. The latter issue can be avoided by the chemical

modification of the channel walls made of different organic materials [30], but still limits its applications requiring more various chemicals.

4.3.2 Optofluidic 3D Printing

Here, my idea is to project the axial light patterns in the microfluidic photoresist flows by reversely utilizing the optical path of APOM (see Section 4.2). By dynamically changing the light pattern and maintaining constant photoresist flows, the projected UV light pattern will become a cross-section of photo-polymerized 3D structures. This work holds significant advantages: (1) it can create arbitrary-shaped 3D structures (potentially) (2) at high throughput and high resolutions and (3) without limit in the kinds of channel walls.

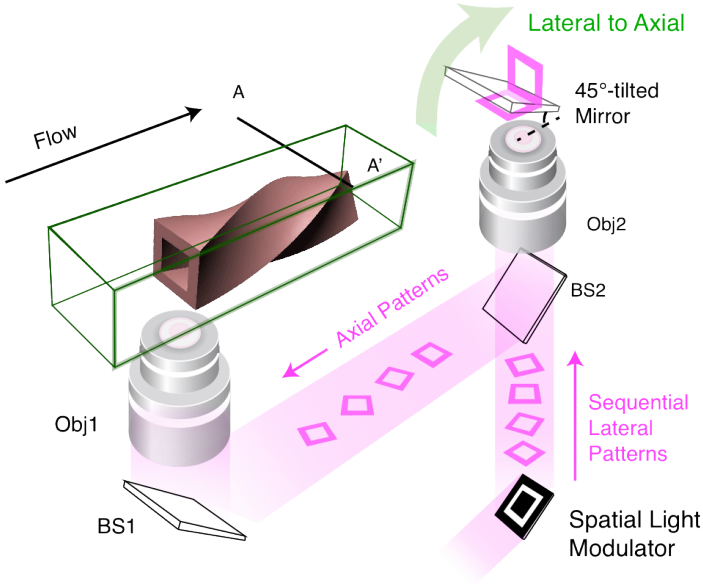

Figure 4.3.2 Optofluidic 3D lithography. By reversely utilizing the optical path in the APOM, the 2D light pattern in the normal plane is converted into the 2D light pattern in the axial plane above the objective lens 2. This axial plane image is projected into the microfluidic flow of photoresist in a microchannel to cause the photo-polymerization. With the continuous flow of the photoresist, consequently, the synthesized 3D structure will have cross-sections corresponding to the axially projected light pattern, enabling creation of 3D arbitrary structures with no limit in size in one dimension.

4.3.2 Optical Setup

Fig. 4.3.4 shows the optical setup for the optofluidic 3D printing, where another 4-f system was utilized to form a light image in a plane corresponding to the imaging plane of the APOM. This allowed the image to travel back in the optical path utilized in the APOM setup. After conversion of this image from a normal to an axial plane and its transfer to objective 1, axial light projection was realized in the flow of photoresist in a microfluidic channel. The light pattern can be dynamically reconfigured by reflecting a UV light from a mercury lamp on the DMD. The reason for using the additional 4-f system is that this optics system was originally designed for the visible wavelength of light and thus could be easily affected by the light dispersion in the UV range. The 4f system allows the user to adjust the position of the image plane relatively easily, enabling adjustment for the dispersion misalignment between the light projection and APOM imaging planes.

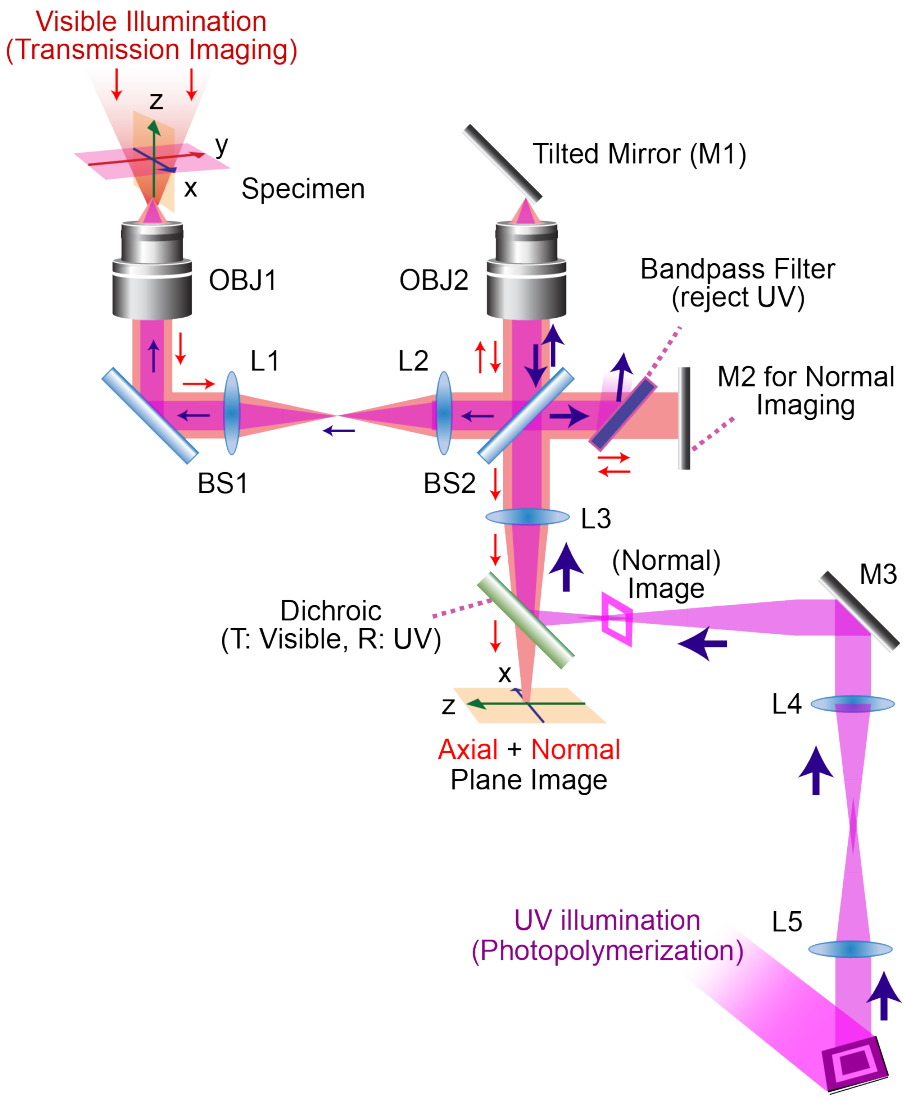

Figure 4.3.4 Optical setup for the Optofluidic 3D Lithography. After passing through L5, L4, and M3, the UV illumination reflected by the DMD light pattern formed a patterned image at a position corresponding to the CCD image plane used in the APOM. Thus, by reversely utilizing the optical path in the APOM, the 2D light pattern in the normal plane was converted into the 2D light pattern in the axial plane above objective lens 2. The converted image was transferred to the objective lens 1 to project the light pattern into the photoresist. Aluminum mirrors were utilized to ensure the highest reflectivity. This projection setup is compatible with transmission normal plane imaging by illumination light from above objective 1. Imaging light has a longer wavelength of red light to prevent interference with the photo-polymerization process.

4.3.2 Result

Alignment of Axial Plane Projection

Optical alignment of axial plane projection requires the simultaneous axial imaging from the same plane of the same sample. A thin film of fluorescence beads coated on a glass cover slip was utilized for this purpose (Fig. 4.3.5). The sample was placed vertically on the side of a glass prism. When properly aligned, I could see the

fluorescence image of the beads in the axial plane, which were excited by the UV light projected in the same plane with relatively good resolution of several microns.

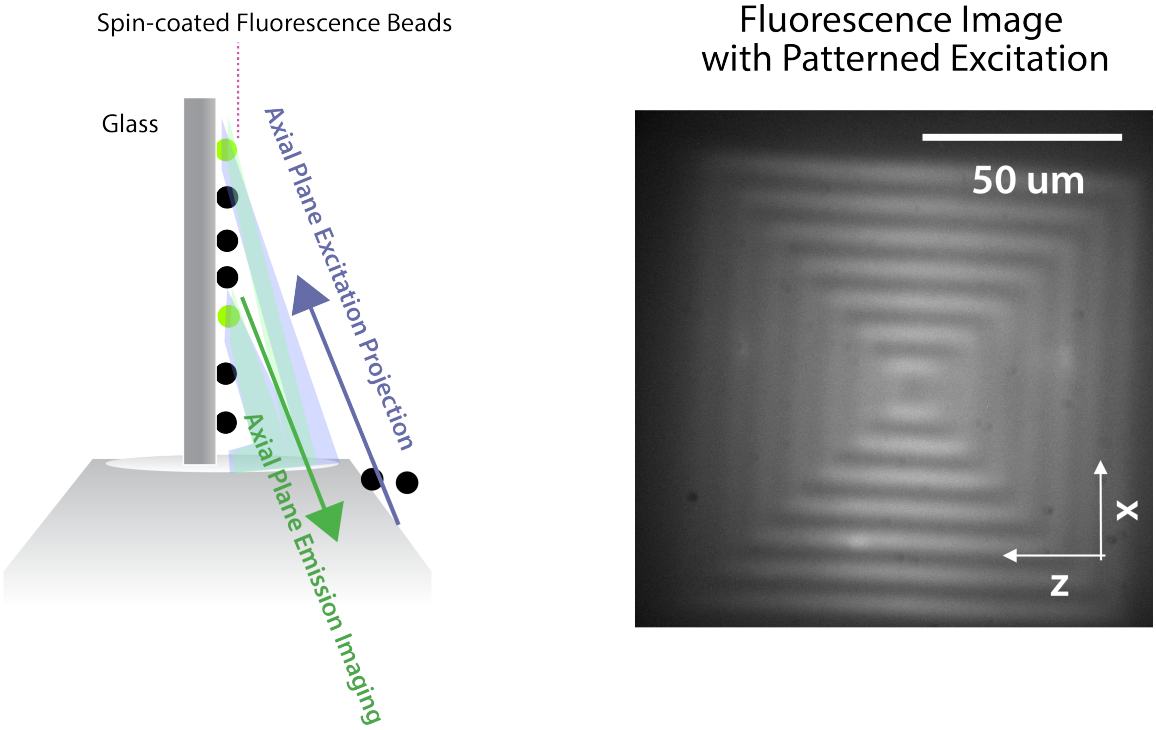

Figure 4.3.5 Alignment of axial plane projection using a layer of fluorescence sample placed in an axial plane of objective 1. Fluorescence beads were spin-coated on a glass cover slip and the slip was placed vertically on the side of a glass prism on top of objective 1. By properly aligning the imaging plane for the visible fluorescence emission and UV light projection in the axial plane, the projected UV light could be observed as the fluorescence emission pattern at relatively good resolutions.

Axial Plane Lithography

With the properly aligned optics, I performed the optical lithography to create a 2D photo-polymerized structure in the axial plane. A mixture of photo-sensitive PEGDA monomer (Poly(ethylene glycol) diacrylate, average molecular weight of 700) as photocurable resin and 10 wt% of a radical photoinitiator (2,2-dimethoxy-2-phenylacetophenone (DMPA, Sigma-Aldrich)). This resin has an optical index of 1.47, which is not far from that of the ideal index of Pyrex glass, ~1.47, such that minimal distortion can be expected. The UV exposure time could be dynamically controlled by changing the time for the light pattern to appear in the DMD. At appropriate exposure time, the axially projected UV light pattern (Fig. 4.3.6a) transferred itself as a photo-polymerized pattern in the resins (Fig. 4.3.6b). The image was taken by illuminating red light from atop of a sample above objective lens 1 (filtered from Tungsten lamp) and collecting signals in the normal plane imaging mode.

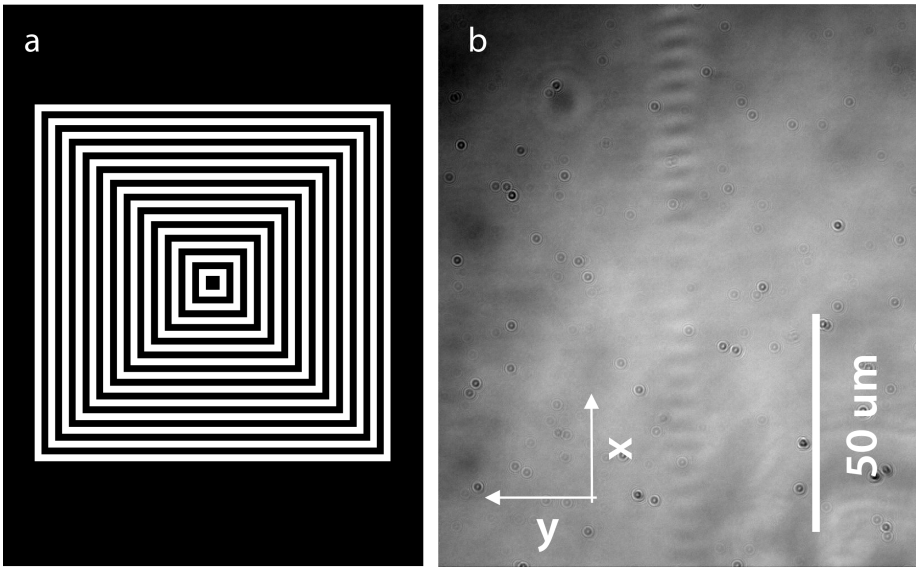

Figure 4.3.6 Photo-polymerization of resin by the axial plane projection of the UV light pattern. As a result of light conversion and transfer of the DMD-imposed pattern **(a),** the photo-polymerized pattern can be observed successfully in the center of the bright field of the normal plane image **(b).**

4.3.3 Summary and Future Outlook

In this section, I showed the exploratory work of optofluidic 3D printing. The result demonstrated the successful transfer of a normal image of light imposed by DMD into the axial plane within the photocurable resins in the microfluidic channel. This first step of the demonstration leads to further optimization of optics in the UV range with a stronger light source, culminating in an ideal optofluidic 3D printer with the resolution limited only by diffraction of light. This new innovation will make a big impact in a wide range of research fields. For example, structured optical fibers (SOF) have been of fundamental importance in both the scientific and industrial community because they can have different but useful optical transmission properties compared to the standard optical fibers [31-33]. SOF includes the photonic crystal fibers that enable the flexible tuning of photonic band gaps [34-39] and demonstrates the lossless transmission of CO_2 laser light through its empty area as a waveguide [39]. Moreover, such photonic crystal fibers are becoming a critical component in nonlinear optic systems such as fiber laser development. However, the fabrication method of the SOF cannot make 3D structures in principle because it relies on a simple pulling of the originally large 2D structure into one dimension, perpendicular to the 2D plane [40]. Conversely, this new 3D printer is able to make such 3D structured optical fibers, opening up an opportunity both in scientific and practical researches. Beyond that, fabrication of 3D structures with a large dimension in one direction with single micron resolutions has been a missing technology. I expect that this invention will stimulate new research fields at the interface between fiber photonics and other fields, including biomedical devices [41], nonlinear optical imaging [42], and optoelectronics fields.

References

1. Anderson, C., "Makers: The New Industrial Revolution", *Crown Business; First edition* (2012).
2. Hull, C. W. Apparatus for production of three-dimensional objects by stereolithography. US Patent, (1986).
3. P. F. Jacobs, Rapid Prototyping & Manufacturing: Fundamentals of StereoLithography, Society of Manufacturing Engineers; 1st edition (1992).
4. Zhang, X., Jiang, X. N. & Sun, C. Micro-stereolithography of polymeric and ceramic microstructures. *Sensors and Actuators A: Physical* **77,** 149–156 (1999).
5. Griffith, M. L. & Halloran, J. W. Freeform Fabrication of Ceramics via Stereolithography. *Journal of the American Ceramic Society* **79,** 2601–2608 (2005).
6. Cooke, M. N., Fisher, J. P., Dean, D., Rimnac, C. & Mikos, A. G. Use of stereolithography to manufacture critical-sized 3D biodegradable scaffolds for bone ingrowth. *J. Biomed. Mater. Res.* **64B,** 65–69 (2003).
7. Sun, C., Fang, N., Wu, D. M. & Zhang, X. Projection micro-stereolithography using digital micro-mirror dynamic mask. *Sensors and Actuators A: Physical* **121,** 113–120 (2005).
8. Bae, Y. C., Soane, D. S. & Crocker, C. Rapid prototype three dimensional stereolithography. (1996).
9. Dhariwala, B., Hunt, E. & Boland, T. Rapid prototyping of tissue-engineering constructs, using photopolymerizable hydrogels and stereolithography. *Tissue Eng.* **10,** 1316–1322 (2004).
10. Carrozza, M. C., Croce, N., Magnani, B. & Dario, P. A piezoelectric-driven stereolithography-fabricated micropump. *J. Micromech. Microeng.* **5,** 177–179 (1999).
11. Giesel, F. L. *et al.* Rapid prototyping raw models on the basis of high resolution computed tomography lung data for respiratory flow dynamics. *Acad Radiol* **16,** 495–498 (2009).
12. Perry, J. W. *et al.* Two-photon polymerization initiators for three-dimensional optical data storage and microfabrication. *Nature* **398,** 51–54 (1999).
13. Zhou, W. An Efficient Two-Photon-Generated Photoacid Applied to Positive-Tone 3D Microfabrication. *Science* **296,** 1106–1109 (2002).
14. Kim, O.-K. *et al.* New Class of Two-Photon-Absorbing Chromophores Based on Dithienothiophene. *Chem. Mater.* **12,** 284–286 (2000).
15. Laza, S. C. *et al.* Two-photon continuous flow lithography. *Adv. Mater.* **24,** 1304–1308 (2012).
16. De Angelis, F., Liberale, C., Coluccio, M. L., Cojoc, G. & Di Fabrizio, E. Emerging fabrication techniques for 3D nano-structuring in plasmonics and single molecule studies. *Nanoscale* **3,** 2689–2696 (2011).
17. Kasko, A. M. & Wong, D. Y. Two-photon lithography in the future of cell-based therapeutics and regenerative medicine: a review of techniques for hydrogel patterning and controlled release. *Future Med Chem* **2,** 1669–1680 (2010).
18. Jhaveri, S. J. *et al.* Direct three-dimensional microfabrication of hydrogels via two-photon lithography in aqueous solution. *Chem. Mater.* **21,** 2003–2006 (2009).

19. Shukla, S., Furlani, E. P., Vidal, X., Swihart, M. T. & Prasad, P. N. Two-photon lithography of sub-wavelength metallic structures in a polymer matrix. *Adv. Mater.* **22,** 3695–3699 (2010).
20. Jeon, S., Malyarchuk, V., Rogers, J. A. & Wiederrecht, G. P. Fabricating three-dimensional nanostructures using two photon lithography in a single exposure step. *Opt. Express* **14,** 2300–2308 (2006).
21. Dendukuri, D., Pregibon, D. C., Collins, J., Hatton, T. A. & Doyle, P. S. Continuous-flow lithography for high-throughput microparticle synthesis. *Nature Materials* **5,** 365–369 (2006).
22. Pregibon, D. C., Toner, M. & Doyle, P. S. Multifunctional Encoded Particles for High-Throughput Biomolecule Analysis. *Science* **315,** 1393–1396 (2007).
23. Chung, S. E. *et al.* Optofluidic maskless lithography system for real-time synthesis of photopolymerized microstructures in microfluidic channels. *Appl. Phys. Lett.* **91,** 041106 (2007).
24. Lee, H., Kim, J., Kim, H., Kim, J. & Kwon, S. Colour-barcoded magnetic microparticles for multiplexed bioassays. *Nature Materials* **9,** 745–749 (2010).
25. Panda, P. *et al.* Stop-flow lithography to generate cell-laden microgel particles. *Lab Chip* **8,** 1056 (2008).
26. Bong, K. W., Bong, K. T., Pregibon, D. C. & Doyle, P. S. Hydrodynamic Focusing Lithography. *Angew. Chem.* **122,** 91–94 (2009).
27. Jang, J.-H., Dendukuri, D., Hatton, T. A., Thomas, E. L. & Doyle, P. S. A route to three-dimensional structures in a microfluidic device: stop-flow interference lithography. *Angew. Chem. Int. Ed. Engl.* **46,** 9027–9031 (2007).
28. Chung, S. E., Park, W., Shin, S., Lee, S. A. & Kwon, S. Guided and fluidic self-assembly of microstructures using railed microfluidic channels. *Nature Materials* **7,** 581–587 (2008).
29. Bong, K. W., Pregibon, D. C. & Doyle, P. S. Lock release lithography for 3D and composite microparticles. *Lab Chip* **9,** 863–866 (2009).
30. Bong, K. W. *et al.* Non-polydimethylsiloxane devices for oxygen-free flow lithography. *Nature Communications* **3,** 805–10 (1AD).
31. van Eijkelenborg, M. *et al.* Microstructured polymer optical fibre. *Opt. Express* **9,** 319 (2001).
32. van Eijkelenborg, M. Imaging with microstructured polymer fibre. *Opt. Express* **12,** 342–346 (2004).
33. Eggleton, B., Kerbage, C., Westbrook, P., Windeler, R. & Hale, A. Microstructured optical fiber devices. *Opt. Express* **9,** 698–713 (2001).
34. Russell, P. Photonic Crystal Fibers. *Science* **299,** 358–362 (2003).
35. Russell, P. S. J. *Photonic-Crystal Fibers*. *J. Lightwave Technol., JLT* **24,** 4729–4749 (IEEE, 2006).
36. Knight, J. C. Photonic crystal fibres. *Nature* **424,** 847–851 (2003).
37. Cho, M. *et al.* Highly birefringent terahertz polarization maintaining plastic photonic crystal fibers. *Opt. Express* **16,** 7–12 (2008).
38. Knight, J. C. *et al.* Anomalous dispersion in photonic crystal fiber. *IEEE Photon. Technol. Lett.* **12,** 807–809 (2000).

39. Temelkuran, B., Hart, S. D., Benoit, G. & Joannopoulos, J. D. Wavelength-scalable hollow optical fibres with large photonic bandgaps for CO2 laser transmission. *Nature* (2002).
40. Bjarklev, A., Broeng, J. & Bjarklev, A. S. Fabrication of Photonic Crystal Fibres, *Springer*, (2003).
41. Choi, M. *et al.* Light-guiding hydrogels for cell-based sensing and optogenetic synthesis in vivo. *Nature Photonics,* online, (2013).
42. Xu, C. & Wise, F. W. Recent advances in fibre lasers for nonlinear microscopy. *Nature Photonics* **7,** 875–882 (2013).